

8-2017

DFIG Based Wind Turbine System For Clemson Micro-grid

Jia Li

Clemson University, jia4@g.clemson.edu

Follow this and additional works at: https://tigerprints.clemson.edu/all_dissertations

Recommended Citation

Li, Jia, "DFIG Based Wind Turbine System For Clemson Micro-grid" (2017). *All Dissertations*. 1989.
https://tigerprints.clemson.edu/all_dissertations/1989

This Dissertation is brought to you for free and open access by the Dissertations at TigerPrints. It has been accepted for inclusion in All Dissertations by an authorized administrator of TigerPrints. For more information, please contact kokeefe@clemson.edu.

DFIG BASED WIND TURBINE SYSTEM FOR CLEMSON MICRO-GRID

A Dissertation
Presented to
the Graduate School of
Clemson University

In Partial Fulfillment
of the Requirements for the Degree
Doctor of Philosophy
Electrical Engineering

by
Jia Li
August 2017

Accepted by:
Professor Richard E. Groff, Committee Chair
Professor Keith A. Corzine
Professor William R. Harrell
Professor Daniel L. Noneaker
Professor Shitao Liu

Abstract

As an important part of the smart grid, the micro-grid interfaces with distributed energy sources, loads and control devices. A doubly fed induction generator (DFIG) based wind turbine (WT) is the main power source of the presented project. The DFIG system is connected to the three phase AC grid via back-to-back power converter and an LCL filter. Decoupled q-d control strategies are investigated for the DFIG system. Matlab/Simulink results will show the performance of the proposed system. Hardware validation results are also presented and discussed.

As a rapidly increasing research interest area the dc micro-grid has been extensively investigated. A topology is proposed to connect the DFIG based WT system to a dc link using a diode bridge and a three phase power converter. The rotor side of the DFIG is connected to the dc link through a converter while the stator is connecting to a three phase diode bridge with the dc side connected to a dc link. The control method is developed to regulate the stator frequency and the d-q axis voltage of the diode bridge to operate the DFIG at a desired stator frequency and generate the required power.

Undesired harmonics in the three phase system will lead to excessive THD, a decrease the power quality and an increase the power loss of the system. An novel methods to compensate the current harmonics by controlling the power converter of the DFIG system is also proposed. With the DFIG connected to the three phase AC grid, the focus has been put into a scenario: a nonlinear load connected to the same node of the DFIG point of common coupling (PCC) to the grid, to draw the harmonics to the system. In the proposed dc link system, the diode bridge will introduce harmonics to the stator current of the DFIG. In both cases, the selected low-order harmonics are detected and calculated by a multiple reference frame estimator. The control methods of how to regulate the harmonics are developed for both the grid-side converter and the rotor-side converter based on multiple reference frame theory.

A hybrid state observer for speed-sensorless motor drives of induction machines is also proposed. The hybrid observer comprises of a Luenberger observer and a sliding mode observer. For a conventional

induction motor with shorted rotor, the stator currents and rotor flux linkages are estimating following a Luenberger observer. While, for a DFIG the similar approach will apply to the stator currents and rotor currents. The rotor speed is estimated using a sliding mode observer. The combination of two observers takes advantage of both approaches. The Luenberger observer is easy to realize and the computational burden is small. The sliding mode observer is known for its robustness with respect to model parameter errors and it will also provide a fast convergence rate. The chattering of the sliding mode observer is addressed by applying a boundary layer.

Acknowledgments

I would like to express my sincere appreciation and thanks to my advisor Dr. Richard E. Groff, and Dr. Keith A. Corzine whose passion and earnest manner in research have transformed me and will benefit me for the rest of my life. Their guidance helped me overcome numerous difficulties and finish my Ph.D study.

I would also like to thank my committee members: Dr. William R. Harrell, Dr. Daniel L. Noneaker, and Dr. Shitao Liu, for their valuable comments and suggestions.

I thank my colleagues in the Clemson Power Electronics and Micro-grid Laboratory: Allan Overstreet, Atif Maqsood, Vahid Dargahi and Anup Thapa for helping me on my research and also daily life. You guys are wonderful companies, and together we went through all good times and hard times.

I especially thank my beloved parents, Haibin Li and Qinglian Ma, for their constant support and unconditional love. I will forever be thankful to all my families who are the sources of all my happiness.

Table of Contents

Abstract	ii
Acknowledgments	iv
List of Tables	vii
List of Figures	viii
Appendix	xi
1 Introduction	1
1.1 Background Introduction	1
1.2 Contributions	5
1.3 Dissertation Organization	6
2 DFIG 3 Phase AC system	7
2.1 Operation of the DFIG Wind Generation	7
3 DFIG DC system	13
3.1 Stator Flux Oriented Control Scheme	13
3.2 Control Of the DC system DFIG	16
4 Multiple Reference Frame Harmonics Regulation	19
4.1 Multiple Reference Frame Harmonics Estimator	20
4.2 Harmonics Regulation in Three Phase AC DFIG System	21
4.3 Harmonics Regulation in DFIG DC System	23
5 Hybrid Observer for Induction Machine	26
5.1 Observer Design for Squirrel Cage Machine	28
5.2 Observer Design for Wound Rotor Machine	30
6 Simulation Results	34
6.1 Simulation Results For AC DFIG Topology	34
6.2 Simulation Results For DC DFIG Topology	35
6.3 Simulation Results For Multiple Reference Frame Based Harmonics Regulation	39
6.4 Simulation Results For Hybrid Observer Sensor-less Drive	45
7 Experimental Results	52
7.1 Experimental Results For AC DFIG System	52
7.2 Experimental Results Multiple Reference Frame Based Harmonics Regulation For AC DFIG System	66
7.3 Experimental Results Of Hybrid Observer Sensor-less Drive	87

8 Conclusion	97
Bibliography	98

List of Tables

6.1	HARMONICS VALUES OF DIFFERENT ORDER	42
6.2	HARMONICS VALUES OF DIFFERENT ORDER OF THE DC DFIG SYSTEM	44
7.1	STATOR CURRENT HARMONICS VALUES OF DIFFERENT ORDER	86
7.2	HARMONICS VALUES OF DIFFERENT ORDER	86

List of Figures

1.1	Clemson micro-grid configuration.	1
1.2	DFIG based WT topology.	2
1.3	Topology of DFIG connect to dc-link.	3
1.4	Nonlinear load connected to the PCC of DFIG WT system.	4
2.1	Induction machine equivalent circuit.	8
2.2	RSC control diagram.	10
2.3	LCL filter topology.	11
2.4	GSC control diagram.	12
3.1	Flux Estimator Blocks	14
3.2	Stator Flux Angle Diagram	15
3.3	Frequency Controller	16
3.4	Control of the RSC	18
4.1	Control of the RSC	21
4.2	GSC Harmonics Regulation	22
4.3	Multiple Reference Frame Harmonic Regulator	24
5.1	The Construction of the Hybrid Observer	28
5.2	T-type Equivalent Circuit for IM	32
6.1	Wind Profile and The Corresponding Power	35
6.2	Stator Command and Actual Power	35
6.3	Machine Active/Reactive Power	36
6.4	The Voltage of The DC-link of The Back-to-Back Converter	36
6.5	Angle Error Obtained From the Controller	37
6.6	Frequency Of the DFIG Stator	37
6.7	Voltage Of the DFIG Stator	38
6.8	The Power Generated From the Machine	38
6.9	Current Draw From the Nonlinear Load	39
6.10	A-Phase Grid Current Before Compensation	40
6.11	FFT Before the Compensation	40
6.12	a-phase grid current after GSC compensation	40
6.13	FFT After GSC Compensation	41
6.14	GSC Current Before Compensation	41
6.15	GSC Current after Compensation	41
6.16	DC DFIG Stator a-phase Current Before Harmonics Compensation	42
6.17	FFT Results Before Harmonics Compensation	43
6.18	DC DFI Stator a-phase Current After Harmonics Compensation	43
6.19	FFT Results After Harmonics Compensation	43
6.20	Speed response to a positive step	45

6.21	Current response to a positive step	46
6.22	Speed response to a negative step	46
6.23	Current response to a negative step	47
6.24	Speed response to a zero speed command	47
6.25	Current response to a zero speed command	48
6.26	Speed response of the hybrid observer for DFIG	49
6.27	Stator current response to a positive speed step	49
6.28	Rotor current response to a positive speed step	50
6.29	Stator current response to a negative speed step	50
6.30	Rotor current response to a negative speed step	51
7.1	Lab Hardware Setup	52
7.2	Converter Cabin	53
7.3	sbRIO-9607 Attached with Interface Board	53
7.4	Stator A Phase Sub-synchronous Mode	54
7.5	Rotor A Phase Sub-synchronous Mode	54
7.6	GSC A Phase Sub-synchronous Mod	55
7.7	Active Power From the Stator Sub-synchronous Mode	55
7.8	Active Power From the Stator Sub-synchronous Mode	56
7.9	Reactive Power From the Stator Sub-synchronous Mode	57
7.10	Reactive Power From the Rotor Sub-synchronous Mode	57
7.11	Stator A Phase Synchronous Mode	58
7.12	Rotor A Phase Synchronous Mode	58
7.13	GSC A Phase Synchronous Mode	59
7.14	Active Power From the Stator Synchronous Mode	59
7.15	Active Power From the Rotor Synchronous Mode	60
7.16	Reactive Power From the Stator Synchronous Mode	60
7.17	Reactive Power From the Rotor Synchronous Mode	61
7.18	Stator A Phase Super-synchronous Mode	62
7.19	Rotor A Phase Super-synchronous Mode	62
7.20	GSC A Phase Super-synchronous Mode	63
7.21	Active Power From the Stator Super-synchronous Mode	63
7.22	Active Power From the Rotor Super-synchronous Mode	64
7.23	Reactive Power From the Stator Super-synchronous Mode	64
7.24	Reactive Power From the Rotor Super-synchronous Mode	65
7.25	Nonlinear Load in Lab	66
7.26	Nonlinear Load Current	67
7.27	Stator Current With Nonlinear Load Connect to PCC Sub-Synchronous Mode	67
7.28	FFT of The Stator Current Sub-Synchronous Mode	68
7.29	Rotor Current With Nonlinear Load Connect to PCC Sub-Synchronous Mode	68
7.30	GSC Current With Nonlinear Load Connect to PCC Sub-Synchronous Mode	69
7.31	Grid Current With Nonlinear Load Connect to PCC Sub-Synchronous Mode	69
7.32	FFT of The Grid Current Sub-Synchronous Mode	70
7.33	Stator Current After the Compensation Sub-Synchronous Mode	70
7.34	Stator Current FFT After the Compensation Sub-Synchronous Mode	71
7.35	Rotor Current After the Compensation Sub-Synchronous Mode	71
7.36	Grid Current After the Compensation Sub-Synchronous Mode	72
7.37	Grid Current FFT After the Compensation Sub-Synchronous Mode	72
7.38	GSC Current After the Compensation Sub-Synchronous Mode	73
7.39	Stator Current With Nonlinear Load Connect to PCC Synchronous Mode	73
7.40	FFT of The Stator Current Synchronous Mode	74

7.41	Rotor Current With Nonlinear Load Connect to PCC Synchronous Mode	74
7.42	GSC Current With Nonlinear Load Connect to PCC Synchronous Mode	75
7.43	Grid Current With Nonlinear Load Connect to PCC Synchronous Mode	75
7.44	FFT of The Grid Current Synchronous Mode	76
7.45	Stator Current After the Compensation Synchronous Mode	76
7.46	Stator Current FFT After the Compensation Synchronous Mode	77
7.47	Stator Current After the Compensation Synchronous Mode	77
7.48	Grid Current After the Compensation Synchronous Mode	78
7.49	Grid Current FFT After the Compensation Synchronous Mode	78
7.50	GSC Current After the Compensation Synchronous Mode	79
7.51	Stator Current With Nonlinear Load Connect to PCC Super-Synchronous Mode	80
7.52	FFT of The Stator Current Super-Synchronous Mode	80
7.53	Rotor Current With Nonlinear Load Connect to PCC Super-synchronous Mode	81
7.54	GSC Current With Nonlinear Load Connect to PCC Super-synchronous Mode	81
7.55	Grid Current With Nonlinear Load Connect to PCC Super-synchronous Mode	82
7.56	FFT of The Grid Current Super-synchronous Mode	82
7.57	Stator Current After the Compensation Super-synchronous Mode	83
7.58	Stator Current FFT After the Compensation Super-synchronous Mode	83
7.59	Rotor Current After the Compensation Super-synchronous Mode	84
7.60	Grid Current After the Compensation Super-synchronous Mode	84
7.61	Grid Current FFT After the Compensation Super-Synchronous Mode	85
7.62	GSC Current After the Compensation Sub-Synchronous Mode	85
7.63	Measured speed response with a positive step	87
7.64	Measured current response with a positive step	88
7.65	Measured speed response with a negative step	88
7.66	Measured current response with a negative step	89
7.67	Measured speed response with a zero speed command	89
7.68	Measured current response with a zero speed command	90
7.69	Hybrid observer speed performance sub-synchronous mode	91
7.70	Stator current estimated and measured sub-synchronous mode	91
7.71	Rotor current estimated and measured sub-synchronous mode	92
7.72	Hybrid observer speed performance synchronous mode	92
7.73	Stator current estimated and measured synchronous mode	93
7.74	Rotor current estimated and measured synchronous mode	93
7.75	Hybrid observer speed performance super-synchronous mode	94
7.76	Stator current estimated and measured synchronous mode	94
7.77	Rotor current estimated and measured synchronous mode	95

APPENDIX

v_s :	DFIG stator voltage
i_s :	DFIG stator current
v_r :	DFIG rotor voltage
i_r :	DFIG rotor current
v_r :	DFIG rotor voltage
i_r :	DFIG rotor current
λ_s :	DFIG stator flux linkage
λ_r :	DFIG rotor flux linkage
r_s :	DFIG stator resistance
r_r :	DFIG rotor resistance
L_{ls} :	DFIG stator leakage inductance
L_{lr} :	DFIG rotor leakage inductance
L_M :	DFIG magnetizing inductance
L_{ss} :	DFIG stator total inductance
L_{ss} :	DFIG rotor total inductance
ω_e :	system synchronous electrical speed
ω_r :	machine rotor electrical speed
P_s :	DFIG stator active power
Q_s :	DFIG stator reactive power
V_s :	RMS value of the grid line to neutral voltage

Chapter 1

Introduction

1.1 Background Introduction

Nowadays with more and more concern being drawn in the problems of the traditional power systems such as environmental pollution, fossil fuel price, depletion of fuel resource, efforts have gone to developing the smart grid [1–3]. Typically, a battery energy storage system, photovoltaic (PV), wind turbine, back-up diesel generators are used as energy sources of a smart grid [4,5]. A modern, locally, small-scale of the centralized smart grid is the concept of micro-grid [6–9].

Figure 1.1 shows the configuration of the planned Clemson micro-grid. Most of the energy sources are connected to the micro-grid via grid connected inverters followed by passive filters. Control of power the electronic inverters are needed to keep the output of the inverters at an acceptable voltage and frequency. This dissertation studies the DFIG based WT in the micro-grid.

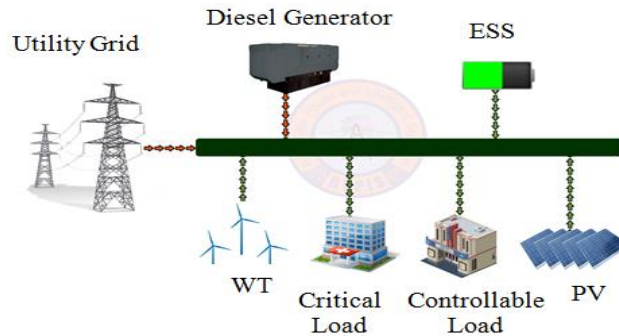


Figure 1.1: Clemson micro-grid configuration.

Wind power is one of the renewable energies that become more and more popular. Wind generators can operate at either fixed speed or variable speed. The DFIG was chosen to be the wind generator for this micro-grid. As a variable speed wind generator, the DFIG has a number of advantages compared to fixed-speed generators including that the machine can operate in sub-synchronous mode, synchronous mode as well as super- synchronous mode, decoupled control of active and reactive power, better energy capture, mechanical stress reduction and low cost with the development of the power electronics converters [10–13].

The basic topology of the DFIG based wind turbine is shown in Figure 1.2. The wind turbine is driving the DFIG through a gearbox. The stator windings of the machine are directly connected to the grid. The rotor side converter (RSC) and the grid side converter (GSC) connected back to back through a dc link. The rotor is connected to the LCL filter through the back-to-back converter, the LCL filter is then connected to the grid to filter out the harmonics. LCL filters have been employed in the system because of their smaller

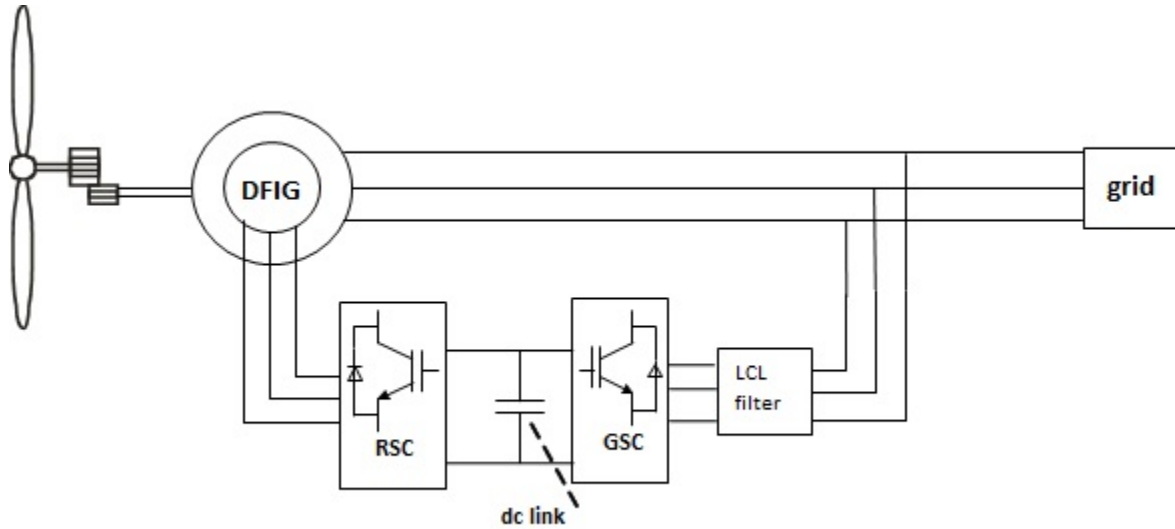


Figure 1.2: DFIG based WT topology.

size and weight, faster dynamic response and better current ripple attenuation [14, 15].

The dc micro grid is extensively investigated by engineers and researches nowadays. The rapid increasing research interest of the dc micro grid is mainly caused by the advantages compared to the ac micro grid as: high quality of power supply, no reactive power flow, less copper loss [16–19]. A topology as shown in Figure 1.3 is proposed to connect the DFIG to a dc link through a three phase diode bridge and RSC. The DFIG based wind turbine has been used widely when connecting to the ac grid. The stator directly connects

to the grid to synchronize the stator frequency of the DFIG to the grid frequency in steady-state operation. Connecting the DFIG to a dc system, the problem encountered firstly is to regulate the frequency of the stator of the DFIG and correctly align the stator voltage of the DFIG to the proper rotating reference frame. A flux-oriented control based on the stator current and stator voltage of the DFIG is employed to synchronize the stator frequency to the reference value and achieve the flux angle to align the stator voltage of the DFIG. With the stator voltage properly aligned, the decoupled d-q control method can easily implemented to control the stator power.

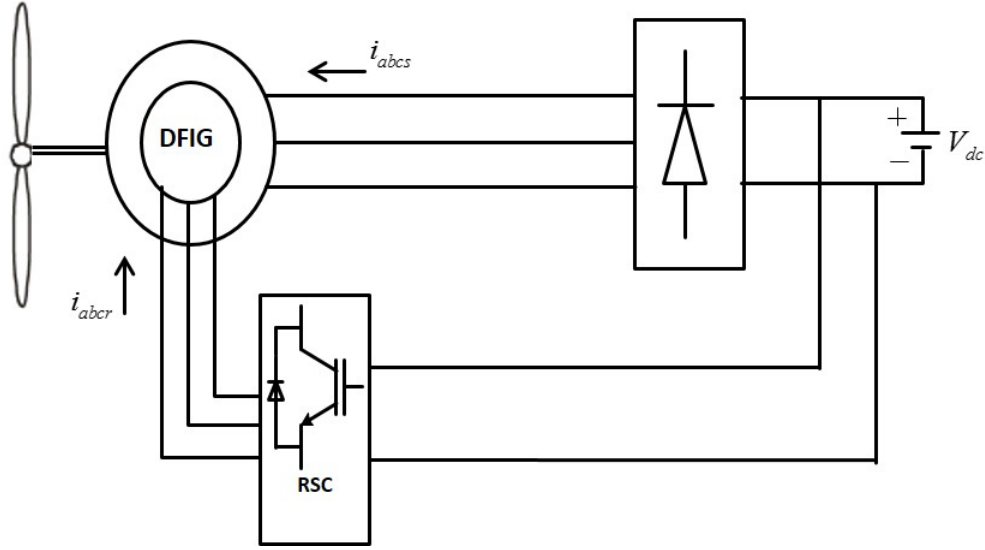


Figure 1.3: Topology of DFIG connect to dc-link.

The problem of harmonics in a power system has been investigated for quite some time. Unwanted harmonics in the system can decrease the power quality, causes overheating, lowers the power factor, increases losses, and possibly effects sensitive electronic equipment [20]. IEEE 519 [21] and IECEN 61000-3 [22] standards specify required regulations governing harmonic compliance. With the development of power electronic devices, proliferation of the diode and thyristor rectifier type front-end nonlinear load has resulted in serious utility interface issues. To elaborate on this problem in three phase ac system, a nonlinear load is connected to the same node of the DFIG point of common coupling (PCC) to the grid, to draw the harmonics to the system as shown in Figure 1.4. In the proposed dc system, the DFIG stator is connected to the grid via a diode bridge. As an uncontrolled power electronic component, the diode bridge will introduce harmonics to the stator current of the DFIG.

Compensating the harmonics using a shunt active filter connecting at the same point with the har-

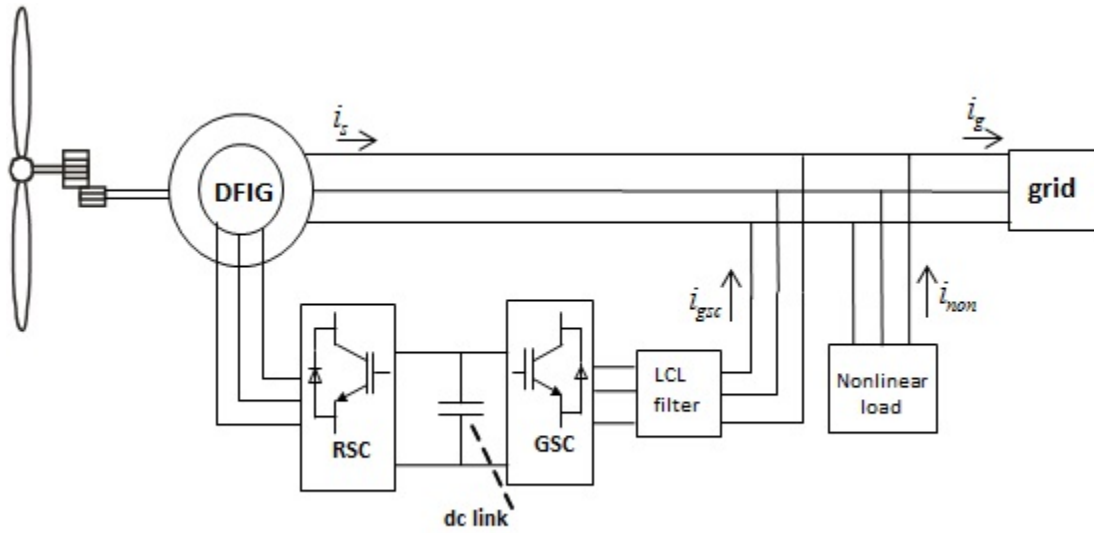


Figure 1.4: Nonlinear load connected to the PCC of DFIG WT system.

monic source is a standard method. One drawback of this is expense due to required power electronic components. In the DFIG system, a power converter is built-in component to regulate the machine. It is easy to make use of the built-in converters to compensate the harmonics without extra cost. In [20] the current of the nonlinear load is measured, and the RSC is used to cancel the harmonics. Whereas, in [23] the authors use a similar approach. Unlike the work presented in [20], the GSC is used as a shunt active filter.

In this dissertation a novel method to detect and regulate the selected order harmonics under a multiple reference frame is introduced. The harmonics with selected order is estimated using a multiple reference frame estimator, and then compensated using a multiple reference frame harmonic regulator. In Figure 1.4, the RSC is used to cancel the current harmonics in the machine stator, and GSC is used to compensate the harmonic draw from the nonlinear load. In the proposed dc system, the diode bridge is connected directly to the machine stator, and so the RSC is a natural choice to enhance the stator power quality. Vector control for induction machines is commonly used because it is easy to implement and has a good dynamic performance [24–26]. In most cases, the machine current and the rotor speed are measured using physical current and speed sensors [27, 28]. In past decades, research efforts have been devoted to developing speed-sensorless drive algorithms which can eliminate the speed sensor. Eliminating the speed sensor can avoid problems such as speed sensor mounting difficulty, sensor's revolution and fragility issues, and reduce the overall system cost.

Various estimation algorithms have been presented in the area of speed-sensorless drives for induction machines. Applying Luenberger observer schemes to build up speed adaptive observers are presented and widely used to estimate the squirrel cage machine states as [29–32]. A rotor position phase lock loop [33–35] is presented to solve the sensor-less drive for a wound rotor machine. In these solutions the speed is a state to identify. The speed estimation accuracy is affected by the model parameter error and noise. When the noise covariances of the measurements and the system process is known, extended Kalman filter (EKF) can be used as optimal filtering to accomplish the state estimation. Work in [36–38] assumes that the derivative of rotor speed is zero, turning the rotor speed (one of the states in EKF) to be an adaptive parameter, wherein EKF is applied to the system to drive the machine. Based on the EKF algorithm, in order to get the observer gain, an $n \times n$ dimension matrix inverse has to be calculated each iteration [39–42] (where n is the number of the state variables). A high dimension matrix inverse not only requires extensive resources to calculate in a micro-controller, it also dramatically increases the difficulty for engineers to program. Using sliding mode observer (SMO) to estimate the IM states has drawn increasing interest in the research area of speed-sensorless drives [43–46]. The SMO is robust against parameter variations and disturbances. The comparative high observer gain of SMO ensures a fast converge rate. However, the SMO takes all the non-linear elements in the system dynamics as disturbances which necessarily results in conservative design.

A novel hybrid state observer combining a Luenberger observer and an SMO is proposed in this paper. A fourth-order Luenberger observer is built to estimate the four electrical variables for the induction machine, while the rotor speed estimation is performed via the SMO. By separating the rotor speed from the electrical states of the machine, the electrical states are in a linear relationship. Luenberger observer for a linear system can be easily established. The estimation of the rotor speed is feeding to the Luenberger observer as a parameter. SMO is proven to have a decent level of robustness against disturbances, parameter errors and system noise [47–50]. The rotor speed can be accurately estimated with a desired converge rate using the SMO.

1.2 Contributions

The unique contributions of this dissertation can be expressed as:

- The DFIG wind turbine system topologies for ac and dc systems are presented. Decoupling control strategies for each are developed.

- A multiple reference frame based harmonics estimator and regulator is proposed using the back-to-back converter of the DFIG system for both the ac and dc DFIG system.
- A hybrid observer is presented for induction machine speed estimation that has a low computation burden and good dynamic performance.

1.3 Dissertation Organization

This dissertation is organized as follows. Chapter 2 proposed a normal way to connect the DFIG based wind turbine to a 3 phase ac system. The d-q decoupled control is developed for the system. Chapter 3 proposes a topology to connect the DFIG based wind turbine to a dc grid. All the challenges and control algorithm are detailed. In Chapter 4 a multiple reference based harmonics estimator and regulator is proposed. The novel method proposed here handles each harmonic as a dc quantities and controlled in parallel with the main control. Chapter 5 details the design of a novel hybrid observer to perform the speed sensor-less drive for an induction machine. Chapter 6 presents the simulation results for the presented problems. Chapter 7 shows some hardware validation results . Chapter 8 concludes the dissertation.

Chapter 2

DFIG 3 Phase AC system

As shown in Figure 1.2, the wind generator in the system, the wind turbine driving the DFIG through a gearbox. The stator windings of the machine are directly connected to the grid. The RSC and the GSC connected back to back through a dc link. The rotor is connected to the LCL filter through the back-to-back converter, the LCL filter is then connected to the grid to filter out the harmonics.

2.1 Operation of the DFIG Wind Generation

DFIG-based wind turbine now is the most popular wind turbine system in the industry. DFIG can generate electrical power to the grid at variable speed. The operation is controlled by the back-to-back converter connected between the rotor side of the machine and the three phase ac grid.

Decoupled d-q control for both RSC and GSC are developed based on the reference frame theory,

the three phase abc quantities to d-q two phase quantities transformation can be represent as

$$\begin{aligned}
 f_{qd0s} &= K_s f_{abcs} \\
 K_s &= \frac{2}{3} \begin{bmatrix} \cos(\theta) & \cos(\theta - \frac{2\pi}{3}) & \cos(\theta + \frac{2\pi}{3}) \\ \sin(\theta) & \sin(\theta - \frac{2\pi}{3}) & \sin(\theta + \frac{2\pi}{3}) \\ \frac{1}{2} & \frac{1}{2} & \frac{1}{2} \end{bmatrix} \\
 (K_s)^{-1} &= \begin{bmatrix} \cos(\theta) & \sin(\theta) & 1 \\ \cos(\theta - \frac{2\pi}{3}) & \sin(\theta - \frac{2\pi}{3}) & 1 \\ \cos(\theta + \frac{2\pi}{3}) & \sin(\theta + \frac{2\pi}{3}) & 1 \end{bmatrix} \\
 \theta &= \int_0^t \omega(\zeta) d\zeta + \theta(0)
 \end{aligned} \tag{2.1}$$

where f can be voltage, current or flux linkage. ω is reference frame speed (rad/sec). θ is reference frame position (rad) [51–54].

2.1.1 RSC Control Strategy

The equivalent circuits of the induction machine under the d-q axis can be simplified as [55]:

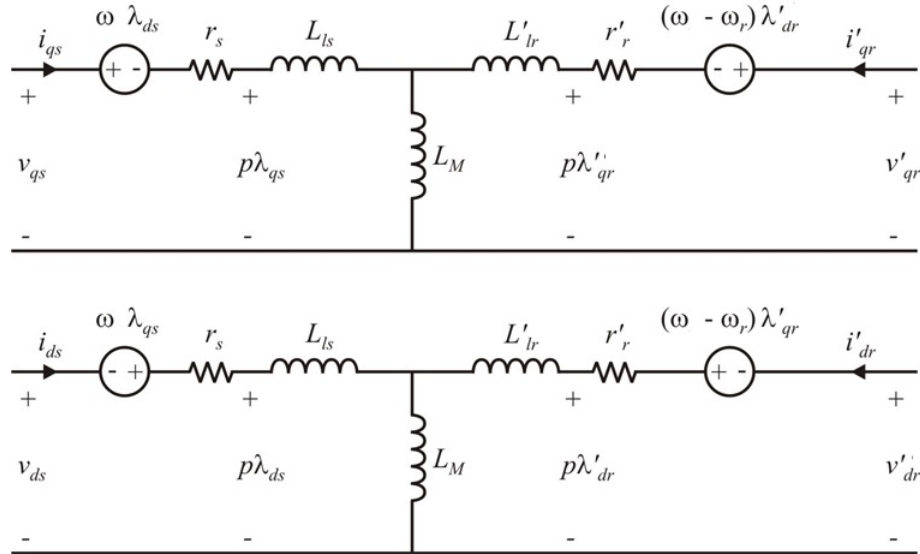


Figure 2.1: Induction machine equivalent circuit.

Figure 2.1 is formed under arbitrary speed ω . From the equivalent circuit the stator side d-q voltage

can be expressed as:

$$v_{qs} = r_s i_{qs} + \omega \lambda_{ds} + \rho \lambda_{qs} \quad (2.2)$$

$$v_{ds} = r_s i_{ds} - \omega \lambda_{qs} + \rho \lambda_{ds} \quad (2.3)$$

where:

$$\lambda_{qs} = L_{ss} I_{qs} + L'_{lr} I'_{qr} \quad (2.4)$$

$$\lambda_{ds} = L_{ss} I_{ds} + L'_{lr} I'_{dr} \quad (2.5)$$

ρ dedicates the derivative of the certain value. The stator of DFIG is directly connect to the grid, a phase lock loop (PLL) can align the grid voltage to q axis making $v_{qs}^e = \sqrt{2}V_s$, $v_{ds}^e = 0$. Superscribe e means the variables are under synchronous reference frame. Superscribe $'$ means the rotor side variables are referred to the stator side. Under system steady state, the derivative goes to 0. Applying the measured the electrical speed of the grid ω_e , and the corresponding angle θ_e to equation (2.2) (2.3),

$$\begin{bmatrix} I_{qs}^e \\ I_{ds}^e \end{bmatrix} = \begin{bmatrix} r_s & \omega_e L_{ss} \\ -\omega_e L_{ss} & r_s \end{bmatrix}^{-1} \begin{bmatrix} V_{qs}^e - \omega_e L_M I'_{dr} \\ V_{ds}^e + \omega_e L_M I'_{qr} \end{bmatrix} \quad (2.6)$$

consider the fact that $\omega_e L_{ss} \gg r_s$ leading:

$$I_{qs}^e \approx -\frac{L_M}{L_{ss}} I'_{qr} \quad (2.7)$$

$$I_{ds}^e \approx \frac{\sqrt{2}V_s}{\omega_e L_{ss}} - \frac{L_M}{L_{ss}} I'_{dr} \quad (2.8)$$

Under the synchronous frame, the stator active and reactive power can be computed using d-q axis component as:

$$P_s = -\frac{3}{2} (V_{qs}^e I_{qs}^e + V_{ds}^e I_{ds}^e) = -\frac{3}{2} \sqrt{2} V_s I_{qs}^e \quad (2.9)$$

$$Q_s = -\frac{3}{2} (V_{qs}^e I_{ds}^e - V_{ds}^e I_{qs}^e) = -\frac{3}{2} \sqrt{2} V_s I_{ds}^e \quad (2.10)$$

In terms of the rotor currents

$$P_s \approx \frac{3}{2} \frac{\sqrt{2}V_s L_M}{L_{ss}} I_{qr}'^e \quad (2.11)$$

$$Q_s \approx \frac{3}{2} \frac{\sqrt{2}V_s L_M}{L_{ss}} I_{dr}'^e - \frac{3V_s^2}{\omega_e L_{ss}} \quad (2.12)$$

From (2.11) (2.12), the DFIG stator power can be controlled using rotor current, following the control diagram: Figure 2.2. The superscript * indicates the reference value of the PI controller, N_r/N_s is the rotor to stator turns ratio. The outer control loop controls the stator active and reactive power independently, output of the PI controller is the q-d axis reference signals $i_{qr}'^{e*}$ and $i_{dr}'^{e*}$ respectively. The inner control loop regulates the q-axis and d-axis rotor currents. The output of the two current controllers is compensated by the corresponding cross-coupling terms to get the voltage signals $v_{qr}'^{e*}$ and $v_{dr}'^{e*}$. These voltage control signals are then used by the PWM module to produce gate signals to drive the RSC [56–59].

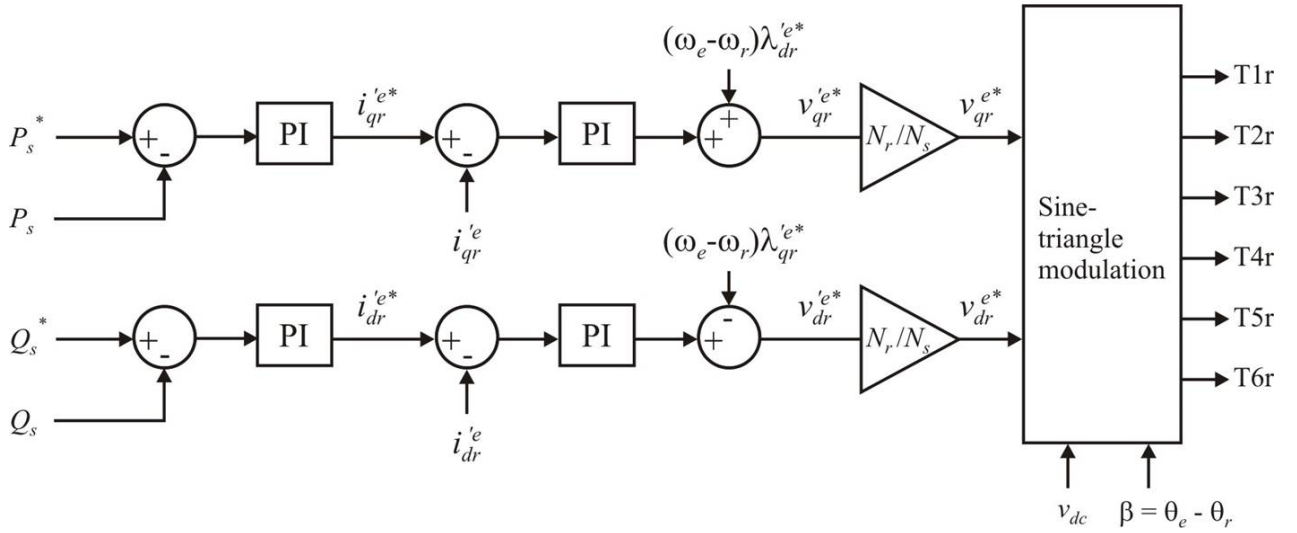


Figure 2.2: RSC control diagram.

2.1.2 GSC Control Strategy

From Figure 1.2, the GSC is connected to the grid through a LCL filter. LCL filters have been employed in the system because of their smaller size and weight, faster dynamic response and better current ripple attenuation [15,60]. The LCL is connected as in Figure 2.3, having a cutoff frequency of $\sqrt{\frac{L_1+L_2}{3L_1L_2C}}$ [61, 62]. Using the GSC to regulate the dc link voltage of the back-to-back converter is straight forward following

Figure 2.4. The control scheme consist two cascaded control loops. The outer control loop regulates the dc link voltage v_{dc} and generates the q-axis current reference signal i_q^{e*} . The d-axis current component i_d^e is set to be regulated to zero because no reactive power is desired through the GSC. The inner current loop regulates the q-axis and d-axis components of current. The output of the two current controllers are compensated by the corresponding cross-coupling terms to get the voltage signals to generate the switching signals for the converter [63–65].

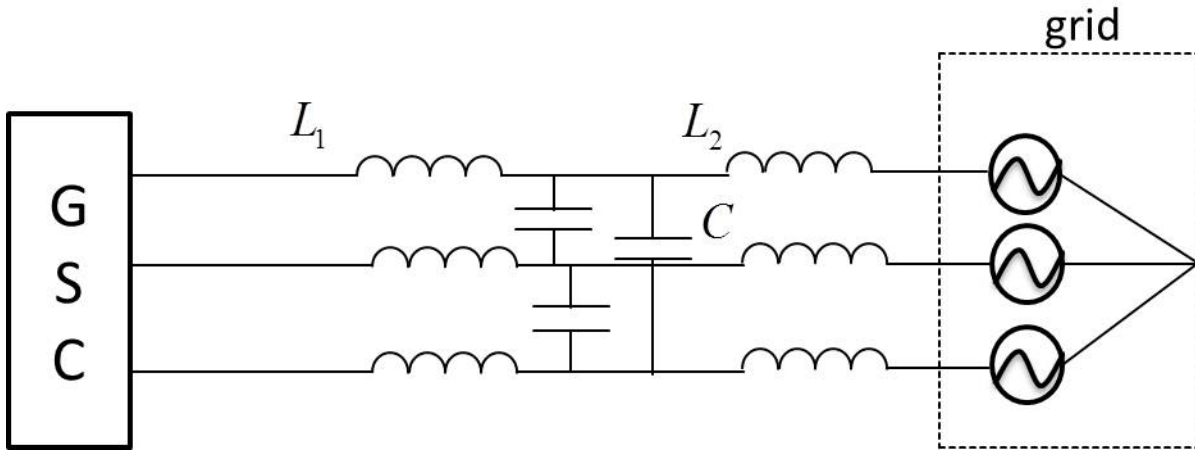


Figure 2.3: LCL filter topology.

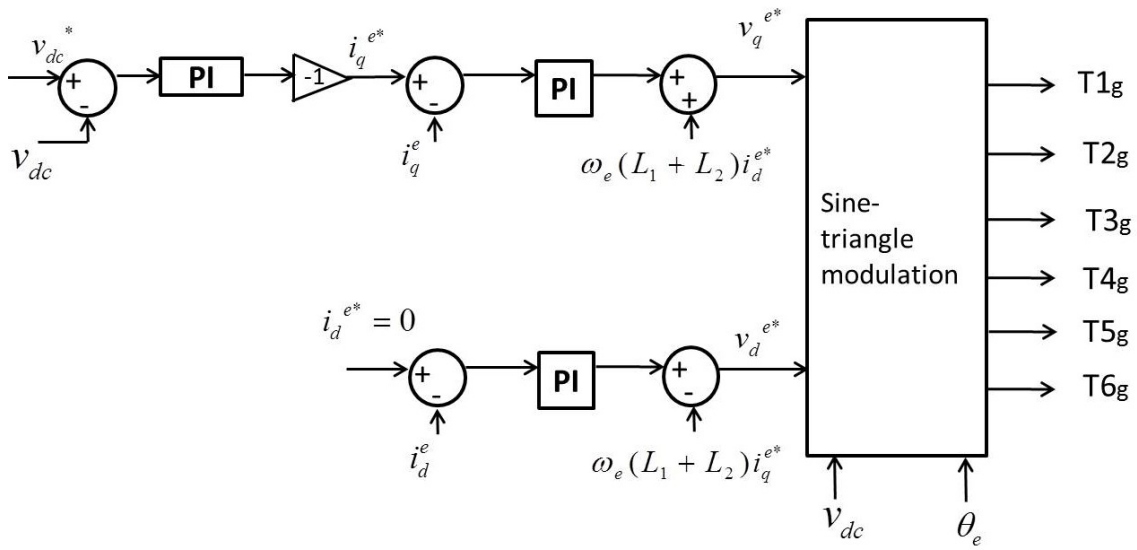


Figure 2.4: GSC control diagram.

Chapter 3

DFIG DC system

The conventional topology, dc link voltage is connected between the back to back converter. The RSC is connected to the rotor controlling the active and reactive power of the stator of the DFIG. The GSC is regulating the dc link voltage with the ac side to the converter connecting to the grid. In this system, the low speed wind turbine drives the DFIG through a gearbox, making the rotor speed around the grid frequency fitting the slip in the range of 25% [66, 67]. The stator directly connects to the grid synchronize the stator frequency of the DFIG to the grid frequency in steady-state operation. In this paper the DFIG is connected to a dc link through a three phase diode bridge and RSC. The proposed dc system topology is shown in Figure 1.3. The dc link in the system is assumed to be a constant dc voltage which is not deliberated here.

3.1 Stator Flux Oriented Control Scheme

The problem encountered firstly is to regulate the frequency of the stator of the DFIG and correctly align the stator component. A stator flux-oriented control based on the stator current and stator voltage of the DFIG is employed to synchronize the stator frequency to the reference value and achieve the flux angle to align the stator flux of the DFIG.

3.1.1 Flux Estimator

The first paper detailing flux oriented control is presented by F. Blaschke in early 1970s to control the induction motor [24]. As a vector control method flux oriented control has to be operated in d-q reference frame. According to Parks transform equation (2.1), just like equations(2.2),(2.3) The stator side voltage can

be described as:

$$v_{qs} = r_s i_{qs} + \omega \lambda_{ds} + \rho \lambda_{qs} \quad (3.1)$$

$$v_{ds} = r_s i_{ds} + \omega \lambda_{qs} + \rho \lambda_{ds} \quad (3.2)$$

Here, the stator flux reference frame is chosen to accomplish the FOC. The flux will be aligned on d-axis.

Under the stationary frame with $\omega=0$, equation (2) (3) can be represented as :

$$v_{qs}^s = r_s i_{qs}^s + \rho \lambda_{qs}^s \quad (3.3)$$

$$v_{ds}^s = r_s i_{ds}^s + \rho \lambda_{ds}^s \quad (3.4)$$

Superscript s means the values are in stationary frame. ρ means derivative of the certain value. $v_{qs}^s, v_{ds}^s, i_{qs}^s, i_{ds}^s$ is the stator voltage and current q d axis value of DFIG and $\lambda_{qs}^s, \lambda_{ds}^s$ is the flux q d axis value, r_s is the rotor resistor of the machine. Figure3.1 shows the flux estimator blocks implemented to calculate the flux and the angle of the flux base on the equation (3.3),(3.4).

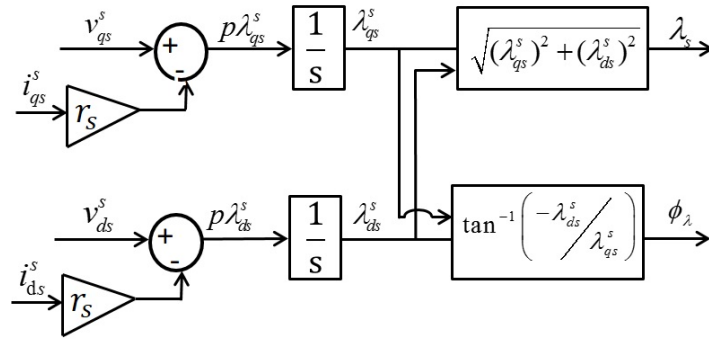


Figure 3.1: Flux Estimator Blocks

ϕ_λ is the angle captured from the flux estimator block. To properly align the flux on d-axis, $\theta_e = \phi_\lambda + \frac{\pi}{2}$ is picked to form the rotating frame. The corresponding angular speed of this angle is ω_e . As shown in Figure3.2, q d axis flux then becomes $\lambda_{qs}^e = 0, \lambda_{ds}^e = \lambda_s$, superscript e means the component is aligned using θ_e with speed ω_e and the q d axis voltage under the stator flux synchronous rotating frame becomes

$$v_{qs}^e = r_s i_{qs}^e + \omega_e \lambda_{ds}^e \quad (3.5)$$

$$v_{ds}^e = r_s i_{ds}^e + \rho \lambda_{ds}^e \quad (3.6)$$

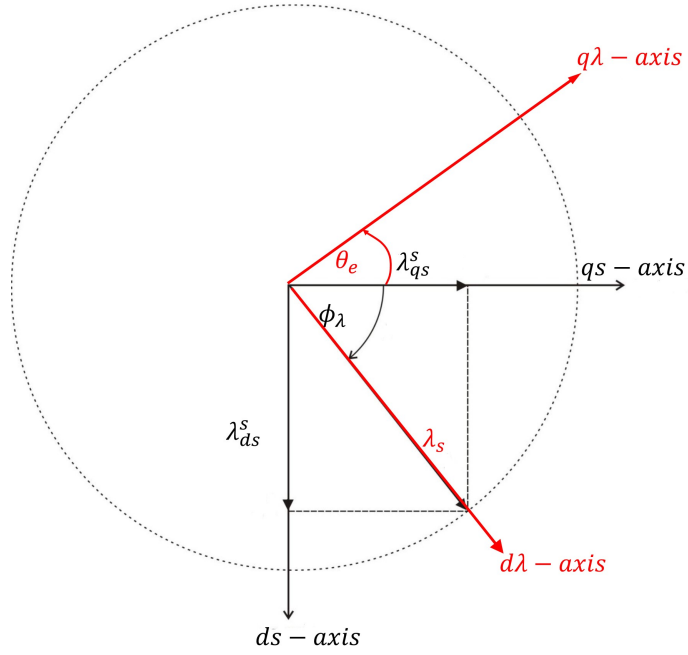


Figure 3.2: Stator Flux Angle Diagram

3.1.2 Frequency Control and Regulation

Conventionally, the stator of DFIG directly connects to the grid the frequency of the stator is imposed by the grid. Whereas, the proposed dc DFIG system, the machine is connected to a dc link through a diode bridge. The frequency of the stator should be controlled closed to the rated value of the machine. In an ac DFIG system the frequency can be obtained by a simple PI controller forcing the q/d axis voltage/current to be zero, then the error goes to another PI controller to compare with the reference constant frequency. This way both the frequency and the phase can be regulated. However, the same procedure is not suitable in the proposed system. The simple two PI loops will just guarantee either the frequency or the phase. The rigid frequency will also cause stator current discontinuous in due to the dc link [68–70].

The method to control the frequency is by implementing a frequency controller as shown in Figure 3.3. The reference angle θ^* , using to align the flux is generating by integrating the reference constant frequency ω^* . Compared θ_e with θ^* , the error σ goes through a gain and pure integrator then add back to the angle θ^* to correct the reference angle [68].

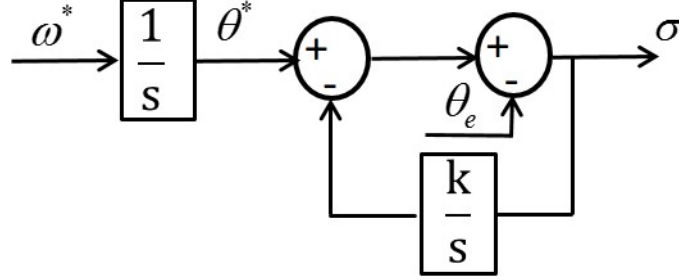


Figure 3.3: Frequency Controller

3.2 Control Of the DC system DFIG

In the topology of the proposed system, RSC is implemented to control the stator power by q axis current and d axis current is used to regulate the frequency and keep the flux. The electrical torque T_e of the DFIG can be presented using the stator current and flux variables as [71]

$$T_e = \frac{3P}{4}(\lambda_{ds}i_{qs} - \lambda_{qs}i_{ds}) \quad (3.7)$$

P is the number of poles of the machine. Since the stator flux is properly aligned on the d axis, leading the electrical torque equation to be

$$T_e = \frac{3P}{4}\lambda_{ds}i_{qs} \quad (3.8)$$

According to the stator q axis flux equation

$$\lambda_{qs}^e = L_{ss}i_{qs}^e + L_M i_{qr}'^e \quad (3.9)$$

Under stator flux synchronous rotating frame, $\lambda_{qs}^e = 0$, $i_{qs}^e = \frac{-L_M}{L_{ss}}i_{qr}'^e$, leading the electrical torque is proportional to rotor side q axis current. In a dc system, there is no reactive power transfer between DFIG and the dc source, the power of the machine can be regulated by the rotor side q axis current $i_{qr}'^e$.

In a steady operation state, the derivative part of stator voltage equation will be 0. Equation (3.3),(3.4)

will be further simplified to

$$V_{qs}^e = r_s I_{qs}^e + \omega_e (L_{ss} I_{ds}^e + L_M I_{dr}^{e'}) \quad (3.10)$$

$$V_{ds}^e = r_s I_{ds}^e \quad (3.11)$$

The capital letter means the variables are in steady operation state. In DFIG, $r_s \ll \omega_e L_M < \omega_e L_{ss}$, the r_s term can be neglected. Leads $V_{ds}^e \approx 0$, this will be proved and shown in the simulation results. With the approximation that d axis voltage is 0, the stator voltage which is imposed by the dc source is aligned on q axis. With a diode bridge connect to a dc source, the line to neutral fundamental RMS values should be $\frac{\sqrt{2}}{\pi} V_{dc}$ which V_{dc} is the value of the dc source voltage. At the stator side:

$$V_{qs}^e = \frac{2}{\pi} V_{dc} \quad (3.12)$$

$$I_{ds}^e = \frac{V_{qs}^e}{\omega_e L_{ss}} - \frac{L_M}{L_{ss}} I_{dr}^{e'} \quad (3.13)$$

The dc source is assumed to be a constant value, it can be conclude that the frequency e can be controlled by rotor side q axis current.

Figure 3.4 shows the q-d decoupled control of RSC. The error of the request output power and the DFIG provided power will go through a PI controller to generate the q axis reference rotor current i_{qr}^{e*} . The angle error σ is feed to a PI controller to generate the d axis reference rotor current i_{dr}^{e*} . The output of the two current controllers on q d axis are compensated by the corresponding cross-coupling terms to generate the voltage signals v_{qr}^{e*} and v_{dr}^{e*} . These voltage control signals are then used by the PWM module to produce gate signals to drive the RSC. Herein, superscript * means command value. Subscript 1 for the command voltage means the fundamental frequency and also to keep the consistency with the following harmonics compensation sections. The flux linkages $\lambda_{qr}^{e'}$ and $\lambda_{dr}^{e'}$ are the rator q-d axis flux linkage. N_r/N_s is the rotot to stator turns ratio.

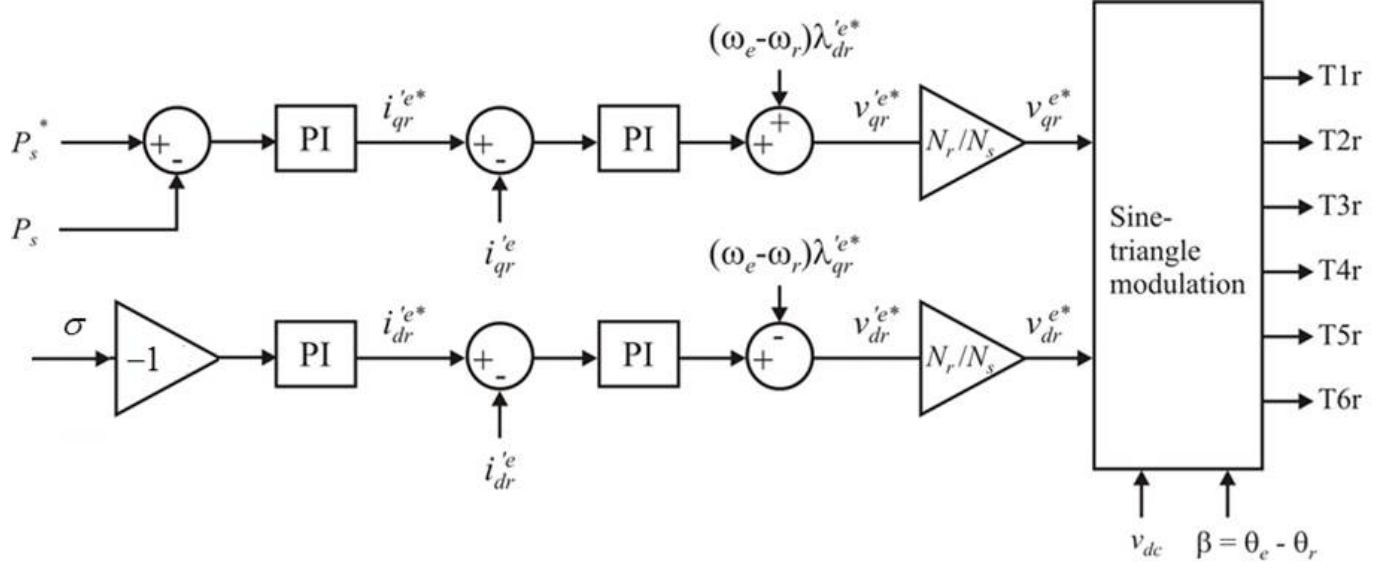


Figure 3.4: Control of the RSC

Chapter 4

Multiple Reference Frame Harmonics

Regulation

The idea presented is compensating grid current harmonics using the back-to-back converter of the DFIG wind generator. The power rating of the back-to-back converter of the DFIG is normally 25% of apparent power of the system. Under certain speeds, the power capability left to compensating harmonics is limited. Under these circumstances, using both sides of the back-to-back converter can extend the potential capacity of the harmonic regulation. Previous work [20, 23] also make use of the back to back converter to accomplish the harmonics compensation. They use the back to back converter and the dc link as a shunt active filter [72, 73]. The way a shunt active filter works is : the three phase current is measured, and transferred to q-d variables under synchronous frame using equation (2.1). The component at fundamental frequency are transferred to dc quantities , whereas all harmonics are transformed to ac quantities with a frequency shift of 60hz (assume the fundamental frequency is 60hz). Extraction of the dc quantity is achieved by low pass filter (LPF), which is insensitive to phase errors [74–76]. The remaining ac quantities is the harmonics component. Using a pi controller to generate the voltage signals to control the converter. The reference signal will be the negative of harmonics component. Which is a ac signal that contents all the high order frequency. Multiple reference frame regulators are detailed for both RSC and GSC. The control of the harmonic regulator is parallel with the main control of the DFIG system. The harmonic regulation methods presented deal with the dc component in different reference frames. Comparing to the conventional active filter, the multiple reference frame harmonics regulator feed the PI controllers a slowly changing dc component as the reference

signal. This way, the high order dynamics of the system will not be excited, ensure the controller has a better performance. Therefore making the control strategy of the proposed method straightforward to implement. Further, the proposed control has good dynamic stability under variable wind speed.

4.1 Multiple Reference Frame Harmonics Estimator

The idea of the multiple reference frame estimator is proposed in [77]. The multiple reference frame estimator operates as a parallel combination of certain synchronous current estimators at different harmonics orders. Due to the existence of the diode bridge connecting between the DFIG stator and the dc link, the stator current is full of the harmonics in order of $n=6m \pm 1$ $m=1, 2, \dots$ respect to the fundament frequency. A multiple reference frame harmonics estimator is proposed in this paper to detect these harmonics and separated the harmonics noise from the fundamental component.

The current transformation under the multiple reference frame can be denoted as:

$$i_{qd0}^n = K^n i_{abc}$$

$$K^n = \frac{2}{3} \begin{bmatrix} \cos(n\theta_e) & \cos(n(\theta_e - \frac{2\pi}{3})) & \cos(n(\theta_e + \frac{2\pi}{3})) \\ \sin(n\theta_e) & \sin(n(\theta_e - \frac{2\pi}{3})) & \sin(n(\theta_e + \frac{2\pi}{3})) \\ \frac{1}{2} & \frac{1}{2} & \frac{1}{2} \end{bmatrix} \quad (4.1)$$

$$(K_s)^{-1} = \begin{bmatrix} \cos(n\theta_e) & \sin(n\theta_e) & 1 \\ \cos(n(\theta_e - \frac{2\pi}{3})) & \sin(n(\theta_e - \frac{2\pi}{3})) & 1 \\ \cos(n(\theta_e + \frac{2\pi}{3})) & \sin(n(\theta_e + \frac{2\pi}{3})) & 1 \end{bmatrix}$$

θ_e is the angle getting from the flux estimator. The input of the multiple reference frame estimator in this paper is the DFIG stator current which containing all the harmonics. The input goes through each transformation block, low pass filter (LPF) will filter out all the ac component, only the corresponding order harmonics will be detected as d-q axis dc current component. Transferring the variables after each LPF back to abc frame using the multiple reference frame theory, add them together. At the input point of each specific harmonic order, subtract this add-up values, and add the corresponding back-transferred abc signals. The output obtaining from the proposed estimator is the different order isolated harmonics dc component in d-q axis under the multiple reference frame [78–81]. The blocks of the multiple reference frame estimator is shown in Figure 4.1.

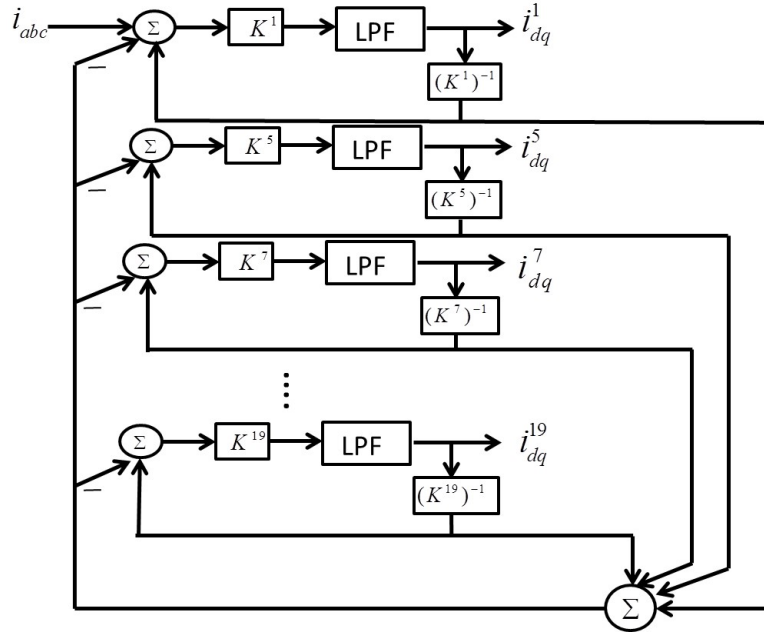


Figure 4.1: Control of the RSC

4.2 Harmonics Regulation in Three Phase AC DFIG System

According to the figure 1.4, based on the KCL

$$i_g = i_s + i_{gsc} + i_{non} \quad (4.2)$$

Where i_g is the current flow in to the grid, i_s is the DFIG stator current, i_{gsc} is the current from the GSC, and i_{non} is the current draw from the nonlinear load.

The goal is to compensate the harmonics in the grid current i_g , so it is straight that we can achieve this by control the three component on the left side of equation (4.2). The current from the nonlinear load is the source of the harmonics and it is off control in the system. So the harmonics should be compensate from neither the stator current of the DFIG i_s , or i_{gsc} the output current of the LCL filter which connected to the GSC of the back-to-back converter of the DFIG wind generator. However, if the harmonics is compensated by the RSC, compensating harmonics current will be injected to the generator to cause unnecessary power in the DFIG, extra heat will also be generator by the machine, big harmonics might also cause unbalanced current in the generator, jeopardize the machine. The DFIG should be used only for the purpose for which it has been installed, i.e., supplying active power only. Following this, the RSC should be used to regulate the stator

power of the DFIG also help to enhance the power quality of the machine itself. Meaning to compensate the harmonics in the stator current i_s . GSC is the more natural option to compensate the harmonics draw from the nonlinear load [23].

4.2.1 Harmonics Regulation By GSC

The basic idea of this control method is by adding the same order of harmonics with negative amplitude to i_g , the harmonics in will be compensated. The topology of the GSC harmonics regulator is shown as Figure 4.2. The d-q axis grid current getting from the multiple reference harmonics estimator of the certain order $6m \pm 1$, $m = 1, 2 \dots$ are the dc quantities. To compensate the grid current harmonics from GSC, the power converter needs to generate the same amplitude dc quantities at each harmonics order with a negative sign. The command signal i_d^{n*} , i_q^{n*} are the detected harmonics signals value times -1 at each harmonic order. This signal compare with the GSC out-put current at each harmonic order i_d^n , i_q^n . The error goes to a well-tuned PI controller and adding a cross coupling term to get the voltage signals under each reference frame respectively [81]. Under the synchronous frame the command voltage to compensate each harmonics will be add up together with fundamental frequency q-d axis voltage using Equation (4.3). to control GSC and regulating the harmonics is .

$$v_q^{e*} = \sum_{m=1}^{n=6m \pm 1} v_{qn}^{e*} + v_q^{e*} \quad (4.3)$$

$$v_d^{e*} = \sum_{m=1}^{n=6m \pm 1} v_{dn}^{e*} + v_d^{e*} \quad (4.4)$$

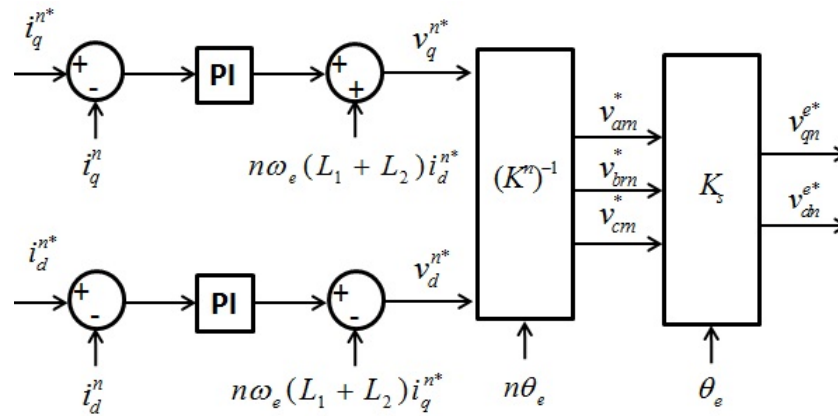


Figure 4.2: GSC Harmonics Regulation

4.2.2 Harmonics Regulation By RSC

When the machine is operated in steady state, the relation between the current in the stator respect to the rotor current under the same multiple reference frame is [82]

$$I_{qs}^n = -\frac{L_M}{L_{ss}} I_{qr}'^n \quad (4.5)$$

$$I_{ds}^n = -\frac{L_M}{L_{ss}} I_{dr}'^n \quad (4.6)$$

As the harmonics of the order $n=6m-1$ $m=1,2,\dots$ will rotate at the backward direction respect to the electrical speed of the stator, resulting the harmonics on the rotor will be detected at frequency $n\omega_e + \omega_r$. The harmonics detected at the frequency $n\omega_e - \omega_r$ on rotor corresponding to those harmonics order of $n=6m+1$ $m=1,2,\dots$ on the stator. The harmonics regulators show as Figure 4.3. The well-tuned PI controller will firstly force the stator harmonics at different order to be 0. Then the error will go to the inner loop PI controller to get voltage control signals in the n order multiple reference frame. This voltage signal have to be transferred back to stationary reference frame then again transfer to synchronous stator flux frame to get the command voltage to cancel out the harmonics. The voltage signals using to control the RSC will be generated following the same approach as GSC control. Each harmonics compensation voltage will be add up together with fundamental frequency q-d axis voltage using Equation (4.5). The voltage v_{qrn}^{e*} and v_{drn}^{e*} will be used to by the PWM module to produce gate signals to drive the RSC to generate the desired power and compensated all the targeted harmonics [81] [83].

$$v_{qr}^{e*} = \sum_{m=1}^{n=6m\pm 1} v_{qrn}^{e*} + v_{qr}^{e*} \quad (4.7)$$

$$v_{dr}^{e*} = \sum_{m=1}^{n=6m\pm 1} v_{drn}^{e*} + v_{dr}^{e*} \quad (4.8)$$

4.3 Harmonics Regulation in DFIG DC System

In the proposed DFIG dc system, Due to the existence of the diode bridge connecting between the DFIG stator and the dc link, the stator current is full of the harmonics in order of $n = 6m \pm 1$ $m=1, 2, \dots$ respect to the fundamental frequency. The harmonics component in the stator current is compensated using the RSC similarly to the section 4.2.2. A multiple reference frame harmonics estimator is applied to detect these harmonics and separated the harmonics noise from the fundamental component. The dc harmonics component

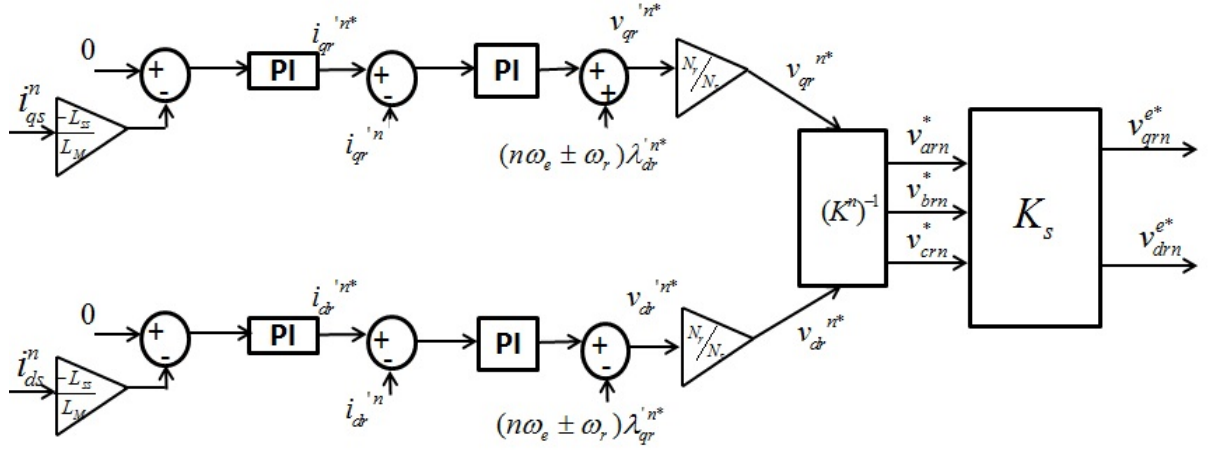


Figure 4.3: Multiple Reference Frame Harmonic Regulator

under each reference frame is regulated using the multiple reference frame RSC harmonics compensator.

Chapter 5

Hybrid Observer for Induction Machine

The three phase induction machine (IM) is prevalently used in industry because of advantages: simple and rugged in construction, low cost, and high operation reliability. Vector control as a commonly applied method to drive the IM has a good dynamic performance. In most cases, the knowledge of rotor speed is essential part to the vector control. In this section, a hybrid observer is proposed to estimated the rotor speed of the IM. The induction machine model under arbitrary reference frame can be described in continuous time model as: [51]

$$\begin{aligned}v_{qs} &= r_s i_{qs} + \rho \lambda_{qs} + \omega \lambda_{ds} \\v_{ds} &= r_s i_{ds} + \rho \lambda_{ds} - \omega \lambda_{qs} \\v'_{qr} &= r'_r i'_{qr} + \rho \lambda'_{qr} + (\omega - \omega_r) \lambda'_{dr} \\v'_{dr} &= r'_r i'_{dr} + \rho \lambda'_{dr} - (\omega - \omega_r) \lambda'_{qr} \\\rho \omega_r &= \frac{P}{2} \frac{(T_e - T_L)}{J}\end{aligned} \tag{5.1}$$

Where P is the number of poles of the machine. Note that equation (5.1) is universal expression for induction machine under arbitrary frame. The objective of this section is to build a observer has the general construction could be applied to estimated the rotor speed, regardless the machine is squirrel cage type or wound rotor.

Apply Euler discretization [84] to the rotor speed dynamics gives in equation (5.1)

$$\begin{aligned}\omega_{r_{k+1}} &= \omega_{r_k} + \rho \omega_{r_k} T_s \\ &= \omega_{r_k} + \frac{P}{2} \frac{(T_e - T_L)}{J} T_s\end{aligned}\quad (5.2)$$

Where T_s is the time step for the discretization. In equation (5.2), T_e is the electrical torque of the machine. The electrical torque of a induction machine can be computed with the knowledge of other machine states .i.e machine currents and flux linkage. If the machine states are measured using a physical sensor and estimated using a state observer. The difference between the estimated speeds based on the measured states and the estimated states can be introduced and defined as a coefficient s .

Based on how the machine states are measured, the electrical torque can be estimated differently. For a squirrel cage machine, only by measuring the stator voltage and current, the full knowledge of machine can be comprehended, and the machine can be properly controlled.

For the squirrel cage machine, the electrical torque T_e can be computed as:

$$T_e = \frac{3}{2} \frac{P}{2} \frac{L_M}{L_{rr}} (\lambda'_{dr} i_{qs} - \lambda'_{qr} i_{ds}) \quad (5.3)$$

The wound rotor machine provide the access of the rotor. Both stator and rotor current and voltage can be measured. To accomplish the vector control for the wound rotor machine, current and voltage values at both side of the machine is imperative. The electrical torque T_e of the wound rotor machine can be expressed as:

$$T_e = \frac{3}{2} \frac{P}{2} L_M (i'_{dr} i_{qs} - i'_{qr} i_{ds}) \quad (5.4)$$

From equation (5.3) (5.16), it can be seen that four machine states are needed to obtained the knowledge of the electrical torque of the machine. From (5.1), if the rotor electrical speed ω_r is treated as a time-variant parameter, the dynamics of i_{ds} , i_{qs} , λ_{dr} and λ_{qr} (for squirrel cage), and the dynamics of i_{ds} , i_{qs} , i'_{dr} , and i'_{qr} , (for wound rotor machine) are linear, and a Luenberger observer is capable of solving this problem. To further simplify the problem, the observer is built in the stationary frame, with $\omega = 0$. The idea of the proposed hybrid observer is using the 4*4 Luenberger observer to estimated the four picked electrical states of the machine. The estimated states is utilized to build a sliding mode observer to predict the rotor speed ω_r . The rotor speed is then feed to the Luenberger observer as a time-variant parameter. The

construction of the hybrid observer is shown in Figure 5.1.

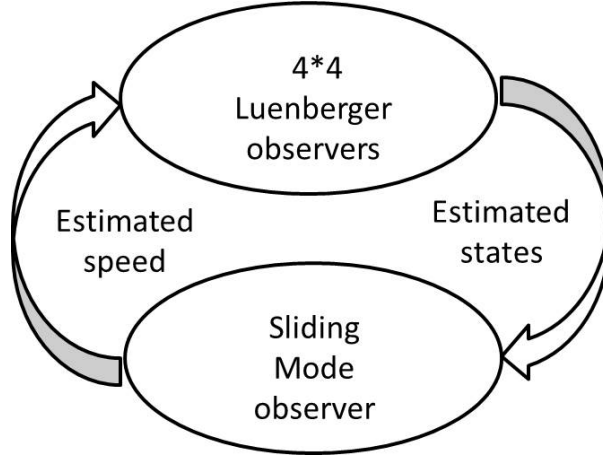


Figure 5.1: The Construction of the Hybrid Observer

5.1 Observer Design for Squirrel Cage Machine

The basic equation for the Luenberger state observer [85–88] can be written as:

$$\rho \hat{x} = A\hat{x} + Bu + G(\hat{x} - x) \quad (5.5)$$

The superscript $\hat{}$ indicates the value is estimated from the observer. The matrix A is the state space matrix, B is the input matrix, G is the gain matrix, to ensure the observer is negative-semidefinite. One desirable character of induction machine is that the motor is self stable, so G can be 0 to predigest the design [89, 90]. With the electrical state picked as i_{ds} , i_{qs} , λ_{dr} and λ_{qr} , and a shorted rotor making the input are

v_{ds}, v_{qs} the state space matrix , and the input matrix B can be denoted as:

$$A = \begin{bmatrix} -\gamma & 0 & \alpha\beta & \beta\omega_r \\ 0 & -\gamma & -\beta\omega_r & \alpha\beta \\ \alpha L_M & 0 & -\alpha & -\omega_r \\ 0 & \alpha L_M & \omega_r & -\alpha \end{bmatrix} \quad (5.6)$$

$$B = \begin{bmatrix} \frac{1}{\sigma} & 0 \\ 0 & \frac{1}{\sigma} \\ 0 & 0 \\ 0 & 0 \end{bmatrix} \quad (5.7)$$

Where

$$\begin{aligned} \alpha &= \frac{r_r'}{L_{rr}} & \beta &= \frac{L_M}{\sigma L_{rr}} \\ \gamma &= \frac{r_s}{\sigma} + \alpha\beta L_M & \sigma &= L_{ss} \frac{1 - L_M^2}{L_{ss} L_{rr}} \end{aligned}$$

From equation (5.3) the the electrical torque based on the estimated valued form the Luenberger observer is

$$\hat{T}_e = \frac{3}{2} \frac{P}{2} \frac{L_M}{L_{rr}} (\hat{\lambda}_{dr} \hat{i}_{qs} - \hat{\lambda}_{qr} \hat{i}_{ds}) \quad (5.8)$$

The coefficient s introduce previously can be defined as:

$$\begin{aligned} s &= \frac{P}{2J} \left(\frac{3}{2} \frac{P}{2} \frac{L_M}{L_{rr}} ((\hat{\lambda}_{dr} \hat{i}_{qs} - \hat{\lambda}_{qr} \hat{i}_{ds}) - (\hat{\lambda}_{dr} \hat{i}_{qs} - \hat{\lambda}_{qr} \hat{i}_{ds})) \right) T_s \\ &= \frac{P}{2J} \left(\frac{3}{2} \frac{P}{2} \frac{L_M}{L_{rr}} (\hat{\lambda}_{dr} \hat{e}_{qs} - \hat{\lambda}_{qr} \hat{e}_{ds}) \right) T_s \end{aligned} \quad (5.9)$$

The SMO for the rotor electrical speed then can be designed using the variable s by

$$\hat{\omega}_{r_{k+1}} = \hat{\omega}_{r_k} + (K_1 \hat{T}_e + K_2 \text{sgn}(s)) T_s \quad (5.10)$$

The function sgn is defined as

$$\begin{cases} \text{sgn}(x) = 1 & \text{if } x > 0 \\ \text{sgn}(x) = 0 & \text{if } x = 0 \\ \text{sgn}(x) = -1 & \text{if } x < 0 \end{cases}$$

In (5.10) both K_1 and K_2 are positive constants. To reduce the chattering of the SMO, the sgn function in (5.10) is replaced by a boundary layer $\text{sat}(x)$ which is given by.

$$\begin{cases} \text{sat}(x) = 1 & \text{if } x > \delta \\ \text{sat}(x) = -1 & \text{if } x < -\delta \\ \text{sat}(x) = x/\delta & \text{else} \end{cases}$$

The SMO has the following dynamics

$$\hat{\omega}_{r_{k+1}} = \hat{\omega}_{r_k} + (K_1 \hat{T}'_e + K_2 \text{sat}(s', \delta)) T_s \quad (5.11)$$

where

$$\hat{T}'_e = \hat{\lambda}_{dr} i_{qs} - \hat{\lambda}_{qr} i_{ds} \quad (5.12)$$

$$s' = \hat{\lambda}_{dr} e_{qs} - \hat{\lambda}_{qr} e_{ds} \quad (5.13)$$

5.2 Observer Design for Wound Rotor Machine

Similar design approach can be applied to the observer of wound rotor machine with slightly changes. With the states chosen for wound rotor machine are i_{ds} , i_{qs} , i'_{dr} , and i'_{qr} , input variables are

v_{ds} , v_{qs} , v'_{dr} , and v'_{qr} , the space matrix A and input matrix B changes to:

$$A = \begin{bmatrix} \frac{-L_{rr}r_s}{\sigma} & \frac{\omega_r L_M^2}{\sigma} & \frac{L_{rr}r'_r}{\sigma} & \frac{\omega_r L_M L_{rr}}{\sigma} \\ \frac{\omega_r L_M^2}{\sigma} & \frac{-L_{rr}r_s}{\sigma} & -\frac{\omega_r L_M L_{rr}}{\sigma} & \frac{L_{rr}r'_r}{\sigma} \\ \frac{L_M r_s}{\sigma} & -\frac{\omega_r L_M L_{ss}}{\sigma} & \frac{-L_{ss}r'_r}{\sigma} & \frac{-\omega_r L_{ss} L_{rr}}{\sigma} \\ \frac{\omega_r L_M L_{ss}}{\sigma} & \frac{L_M r_s}{\sigma} & \frac{\omega_r L_M L_{ss}}{\sigma} & \frac{L_{ss}r'_r}{\sigma} \end{bmatrix} \quad (5.14)$$

$$B = \begin{bmatrix} \frac{L_{rr}}{\sigma} & 0 & \frac{-L_M}{\sigma} & 0 \\ 0 & \frac{L_{rr}}{\sigma} & 0 & \frac{-L_M}{\sigma} \\ \frac{-L_M}{\sigma} & 0 & \frac{L_{ss}}{\sigma} & 0 \\ 0 & \frac{-L_M}{\sigma} & 0 & \frac{L_{ss}}{\sigma} \end{bmatrix} \quad (5.15)$$

The estimated electrical torque will be calculated as:

$$T_e = \frac{3}{2} \frac{P}{2} L_M (\hat{i}_{dr} \hat{i}_{qs} - \hat{i}_{qr} \hat{i}_{ds}) \quad (5.16)$$

Rotor Position Phase Lock Loop is presented by research in [33–35]. Researchers estimate the rotor speed and position in a very easy and straight forward way. From Figure 5.2 based on Kirchhoff's current law at the node of the mutual inductance L_M

$$\begin{bmatrix} i_{qs} \\ i_{ds} \end{bmatrix} + \begin{bmatrix} i_{qm} \\ i_{dm} \end{bmatrix} + \begin{bmatrix} i'_{qr} \\ i'_{dr} \end{bmatrix} = \begin{bmatrix} 0 \\ 0 \end{bmatrix} \quad (5.17)$$

Where i_{qm}, i_{dm} is the magnetization currents. Rearrange the equation (5.17)

$$\begin{bmatrix} i_{qs} \\ i_{ds} \end{bmatrix} + \begin{bmatrix} i_{qm} \\ i_{dm} \end{bmatrix} = - \begin{bmatrix} i'_{qr} \\ i'_{dr} \end{bmatrix} \quad (5.18)$$

Argument i'_s is introduced as $i'_s = i_s + i_m$. The stator voltage after passing through the block $\frac{1}{L_M s}$, yield the magnetization current i_m

$$\begin{bmatrix} i'_{qs} \\ i'_{ds} \end{bmatrix} = - \begin{bmatrix} i'_{qr} \\ i'_{dr} \end{bmatrix} \quad (5.19)$$

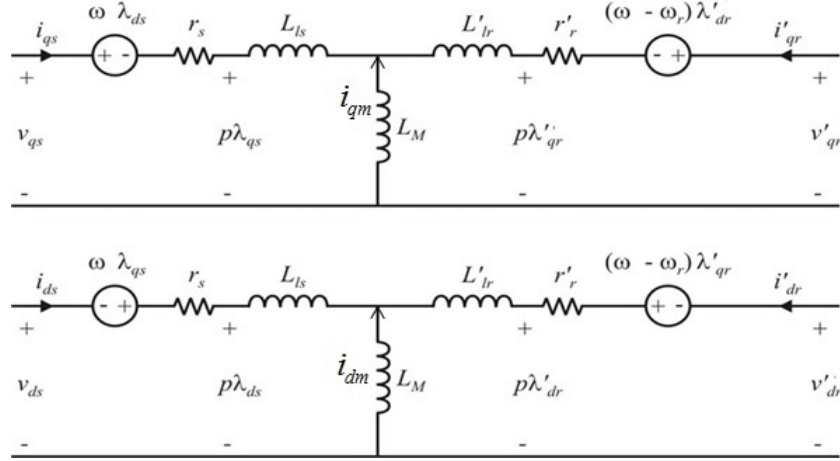


Figure 5.2: T-type Equivalent Circuit for IM

When the estimated speed is equal to the rotor speed and the angle is aligned correctly from the equation (5.19)

$$\hat{i}'_{qs}\hat{i}'_{dr} - \hat{i}'_{qs}\hat{i}'_{dr} = 0 \quad (5.20)$$

The SMO can follow the same dynamics as in equation (5.11), with T'_e and s' change to

$$\hat{T}'_e = \hat{i}'_{dr}\hat{i}'_{qs} - \hat{i}'_{qr}\hat{i}'_{ds} \quad (5.21)$$

$$s' = \hat{i}'_{qs}\hat{i}'_{dr} - \hat{i}'_{qs}\hat{i}'_{dr} \quad (5.22)$$

Theoretically, as stated in section 5.1, with the A matrix in equation (5.5) being semi-negative, the G matrix can be chosen as 0. However, unlike the squirrel cage machine in the lab, which the parameters of the machine are provided by Texas Instruments with accurate values. The DFIG parameter are calculated from the test results conducted in the lab which are not guaranteed to be precise. To ensure a fast converge rate and have a robust performance against system errors, G matrix is not picked as 0 for DFIG. When the system goes to steady state, the rotor speed is accurately predicted and the angle is aligned correctly, equation (5.20) equals to 0, otherwise, the result of equation (5.20) is referred as rotor position error e_r . The dynamic observer gain G could be easily pick as

$$G = g * [abs(e_r), abs(e_r), abs(e_r), abs(e_r)]' \quad (5.23)$$

abs is the absolute value, g is a constant value, and the gain matrix G is changing with the rotor error. When the error is big, the gain matrix is big. When the error is zero, means the system enters the steady state, the gain matrix is 0.

From (5.2), the acceleration of the rotor speed depends on the inertia of the machine and the attached load torque. In many cases, the knowledge of the inertia value is absent. Even if the inertia can be precisely measured offline, load change could still be possible during the drive process. Slightly different from (5.10), in (5.11) the sgn function is replaced by a boundary layer function sat , and \hat{T}_e' and s' are introduced instead of using \hat{T}_e and s . In (5.10), \hat{T}_e and s both depend on machine parameters, while \hat{T}_e' and s' only require the state values estimated from the Luenberger observer. Notice that the gain K_1 and K_2 in the designed SMO (5.11) absorbs the machine parameters used in (5.10) making the designed SMO such that it does not require knowledge of the machine inertia or any other machine parameter. This ensures the hybrid observer has less dependency of machine model accuracy. Since the speed estimation not require accurate machine parameters, it ensures the observer good robustness, and better performance when encountering a load disturbance.

Chapter 6

Simulation Results

6.1 Simulation Results For AC DFIG Topology

All the proposed topology and the control algorithm are simulated employing Matlab/Simulink to prove the performance. The machine parameter is calculated based on some laboratory test as:

$$\begin{aligned} r_s &= 0.0492\Omega & r_r' &= 0.0492\Omega \\ L_{ss} &= 5.9mH & L_{rr}' &= L_{ss} \\ L_M &= 5.3mH \end{aligned}$$

The grid is a three-phase balanced set at 120V 60Hz . The changing wind speed driving the wound-rotor induction machine. The mechanical power from the wind turbine will be tracked by a maximum power point tracking(MPPT) [91–93]. The optimum curve of the turbine will follows [94–97]:

$$P_{opt} = K_{opt} \omega_r^2 \quad (6.1)$$

k_{opt} is the optimum power coefficient, which is picked as 230. Figure 6.1 shows the wind speed profile used to driving the machine, and the corresponding K_{opt} . Note that the maximum power is set to be 23Kw.

The decoupled q-d control strategy is developed for RSC and GSC control. The RSC control is to trace the stator active and reactive power. The power factor is set to be unity. The GSC control fixes the dc link voltage. Figure 6.2 shows the machine RSC is properly controlled to trace the command power.

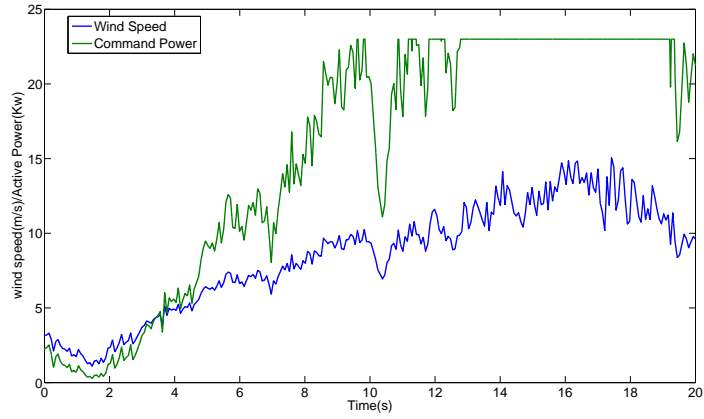


Figure 6.1: Wind Profile and The Corresponding Power

With a command unity power factor, the reactive of the machine should equals to 0. At every beginning, the machine should use some active power from the grid to build up the magnetic field, as shown in Figure 6.3

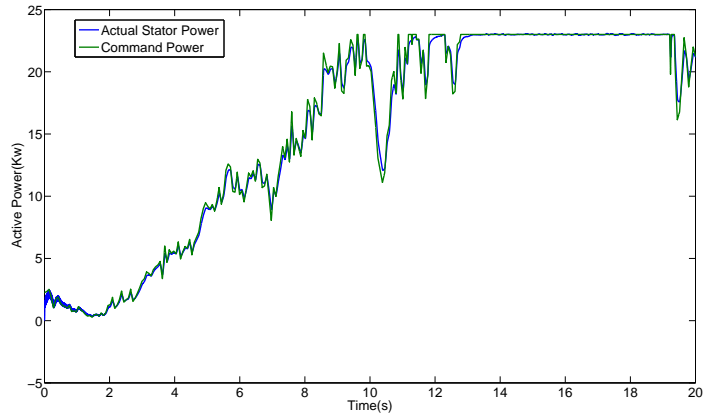


Figure 6.2: Stator Command and Actual Power

The command dc-link voltage is set to be 360V. GSC is used to regulated the voltage, the simulation results is shown below in Figure 6.3

6.2 Simulation Results For DC DFIG Topology

With the DFIG connected to a fixed dc link. As the topology shown in Figure 3. If the frequency controller works as expected, the angle error σ should goes to zero. The frequency can be assumed equal to the reference value. The reference frequency is set to be 60hz. The figure 6.5 and Figure 6.6 elaborate the

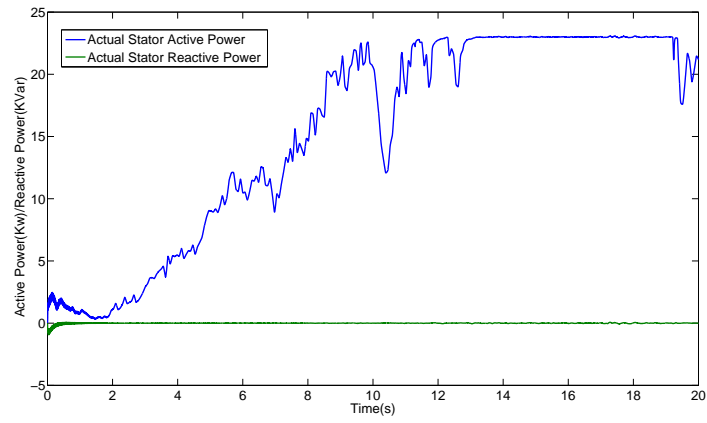


Figure 6.3: Machine Active/Reactive Power

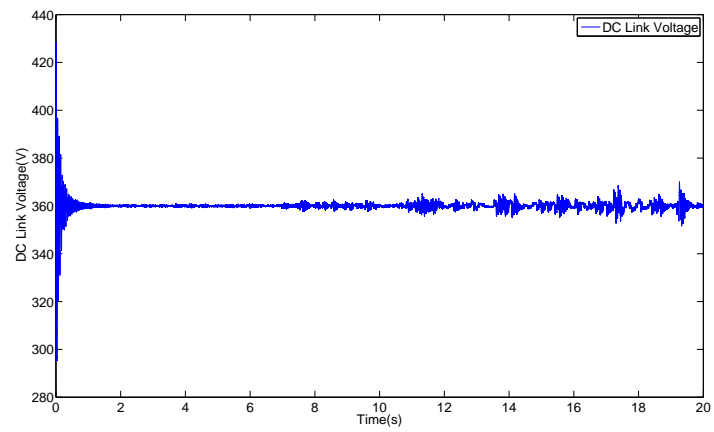


Figure 6.4: The Voltage of The DC-link of The Back-to-Back Converter

performance of the frequency controller. When system enters the steady state, from Equation (3.10),(3.11),

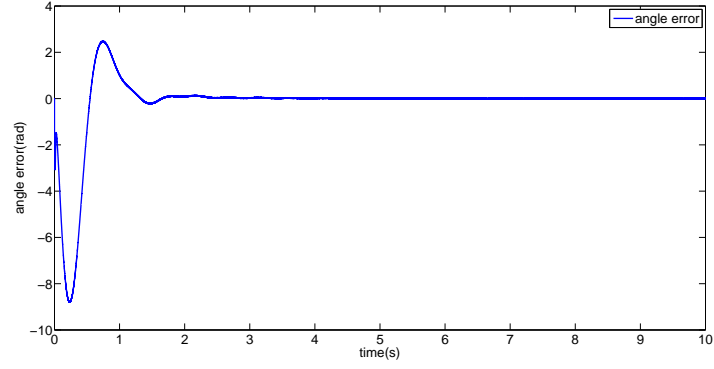


Figure 6.5: Angle Error Obtained From the Controller

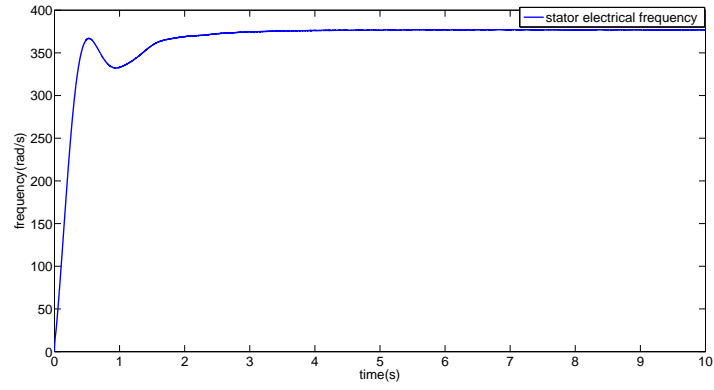


Figure 6.6: Frequency Of the DFIG Stator

if ignore the stator resistor, the d axis voltage is close to zero. Stator voltage is mainly aligning on the q axis. The dc link is a constant voltage 360 by hypothesis. $V_{qs}^e = \frac{2}{\pi} 360 = 229.1831$ [98]. The stator q d axis voltage is deliberate in Figure.6.7. The wind profile used to drive the machine is the same as the one in the Figure 6.1. The power from the machine with the fixed dc-link is shown as in Figure 6.8

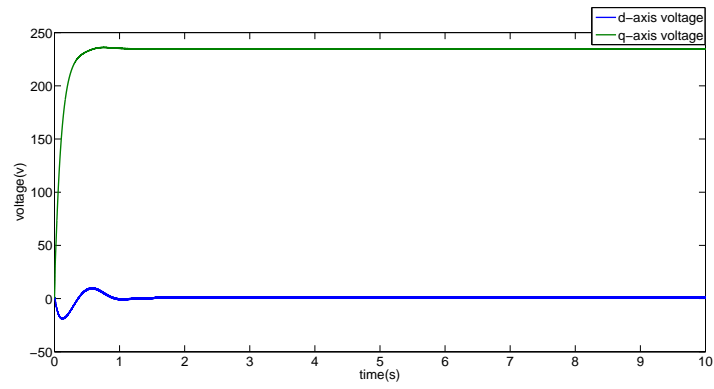


Figure 6.7: Voltage Of the DFIG Stator

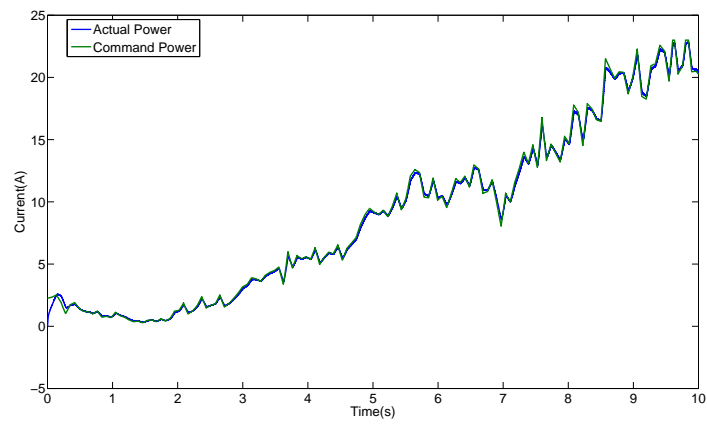


Figure 6.8: The Power Generated From the Machine

6.3 Simulation Results For Multiple Reference Frame Based Harmonics Regulation

With a nonlinear load connected to the PCC of the three phase ac DFIG system as shown in figure 1.4, the current of the grid will be deteriorated. The nonlinear load is simulated by a three phase idea ac-dc thyristor bridge triggered at fixed firing angle. The ac side of the thyristor bridge connected to the PCC, a 34 ohms resistor is connected to the dc side. The nonlinear load draws order of $n = 6m \pm 1m = 1, 2, \dots$ harmonics to the grid making the grid current highly distorted. The current draw from the nonlinear load is shown in Figure 6.9

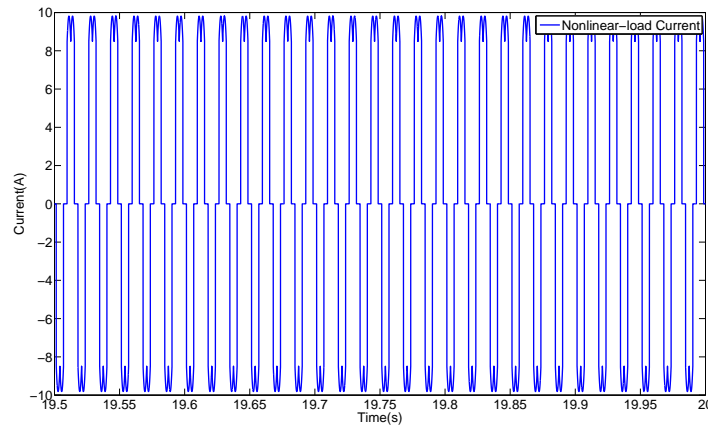


Figure 6.9: Current Draw From the Nonlinear Load

Figure 6.10 is the a-phase grid current with harmonics, the amplitude is varying with the changing of the power flowing into the grid.

The fast Fourier transform (FFT) analyzes is carried to the current, the results shows in the Figure 6.11

In the three phase ac DFIG system, GSC is picked to compensate the harmonics draw from the nonlinear load. After the compensation the current flows in to the grid changes to Figure 6.12 Applying FFT to the current, the results is shown in Figure 6.13 Using the GSC to compensate the harmonics draw from the nonlinear load, the current from the GSC will generate the same harmonics at the same frequency with negative amplitude. Figure 6.14 and 6.15 shows the current of GSC changes after compensating the harmonics Table.6.1 explicitly presents the selected order harmonics changing before and after the harmonics regulation.

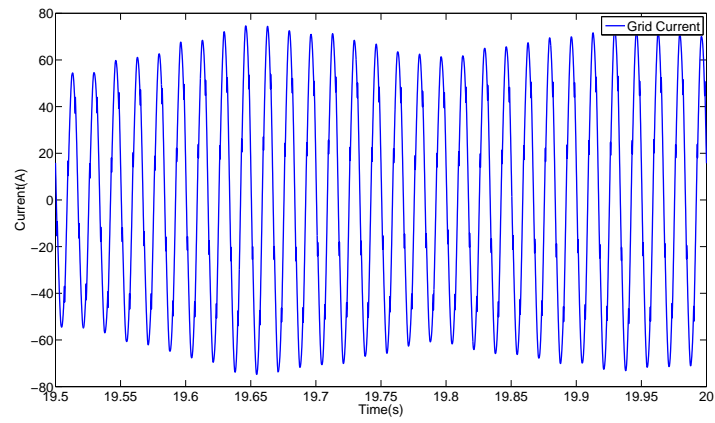


Figure 6.10: A-Phase Grid Current Before Compensation

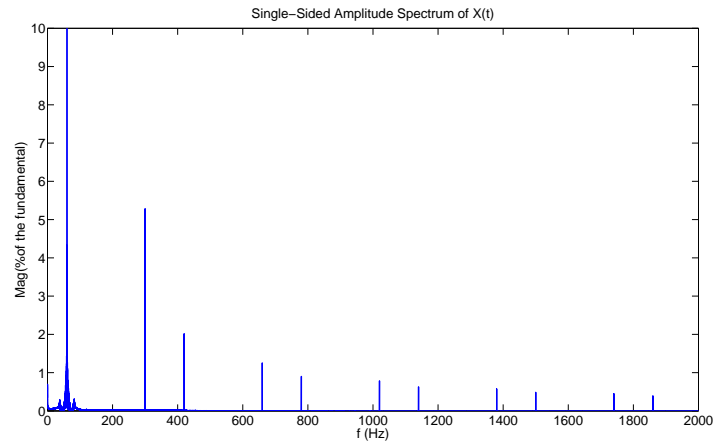


Figure 6.11: FFT Before the Compensation

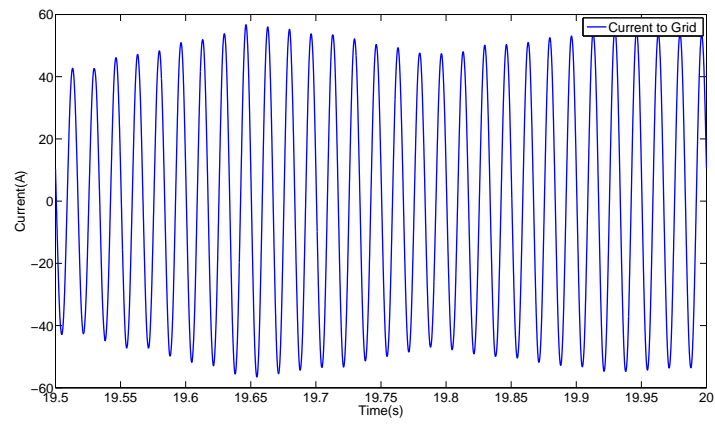


Figure 6.12: a-phase grid current after GSC compensation

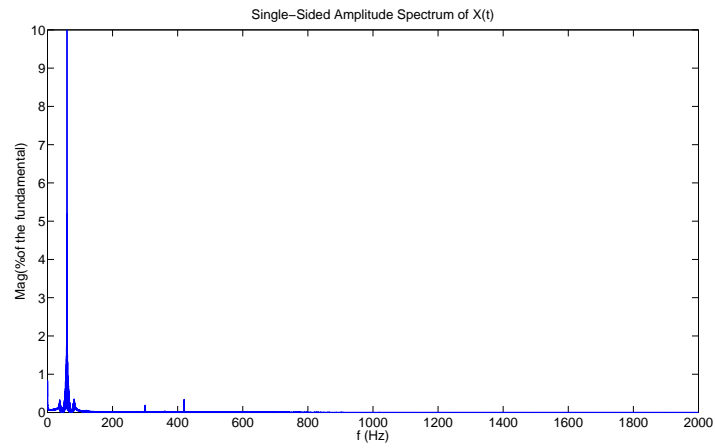


Figure 6.13: FFT After GSC Compensation

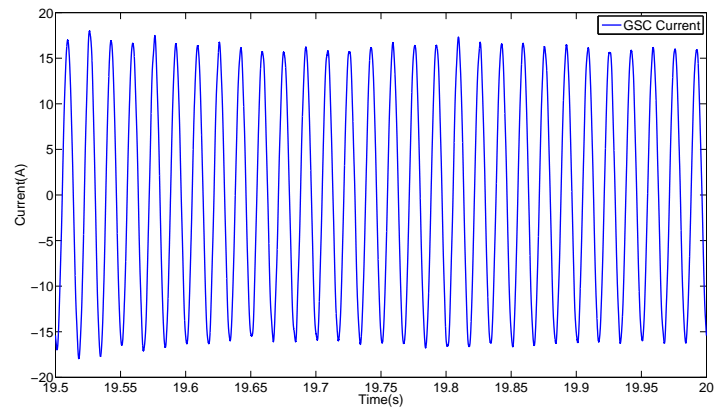


Figure 6.14: GSC Current Before Compensation

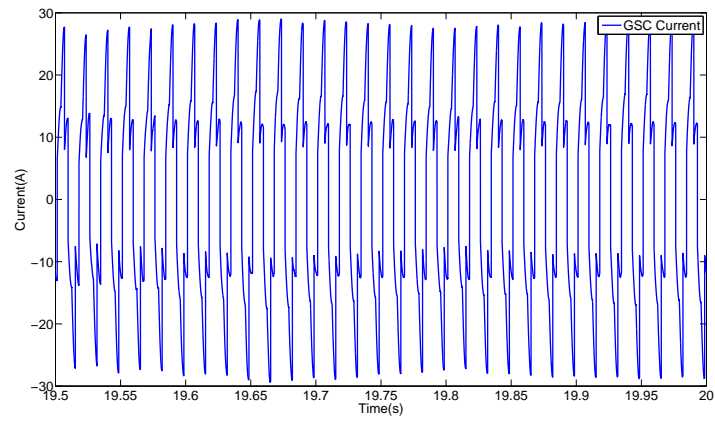


Figure 6.15: GSC Current after Compensation

Table 6.1: HARMONICS VALUES OF DIFFERENT ORDER

Harmonics Order	Before Regulation	After Regulation
5	5.23%	0.18%
7	2.14%	0.39%
11	1.37%	0.01%
13	0.91%	0.03%
17	0.61%	0.02%
19	0.47%	0.08%

As stated in section 3, the uncontrollable diode bridge will introduce harmonics at $n = 6m \pm 1$ $m=1,2,\dots$. The stator current waveform and the FFT results before the compensation is shown as Figure 6.16, 6.17

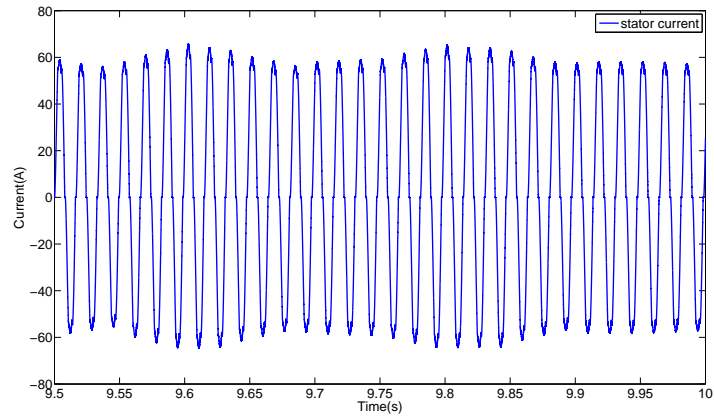


Figure 6.16: DC DFIG Stator a-phase Current Before Harmonics Compensation

The multiple reference frame estimator is used to detect the harmonics in the stator, and the harmonics component then compensated by a multiple reference harmonics regulator. After compensation, the A phase stator current waveform and the FFT analysis results are presented in Figure 6.18 and Figure 6.19

The table 6.2 details the performance of the harmonics compensation of each selected harmonics

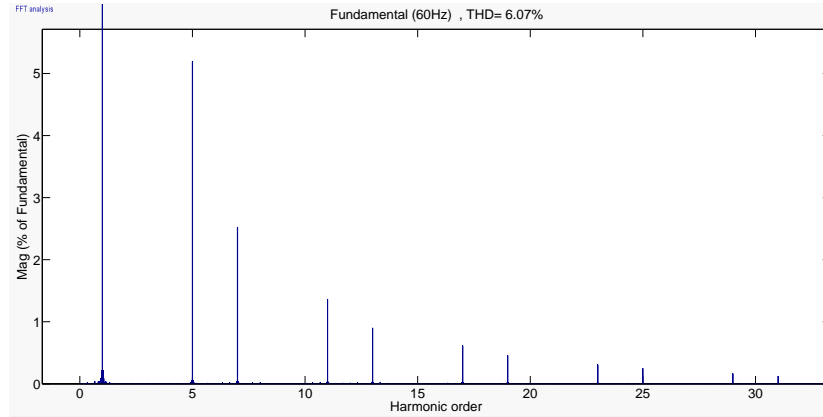


Figure 6.17: FFT Results Before Harmonics Compensation

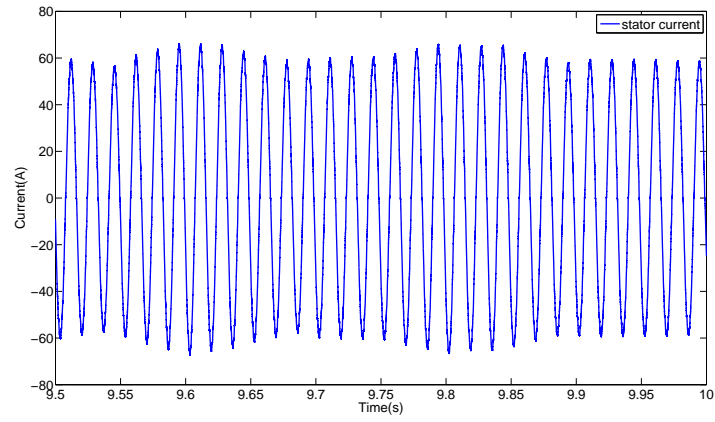


Figure 6.18: DC DFI Stator a-phase Current After Harmonics Compensation

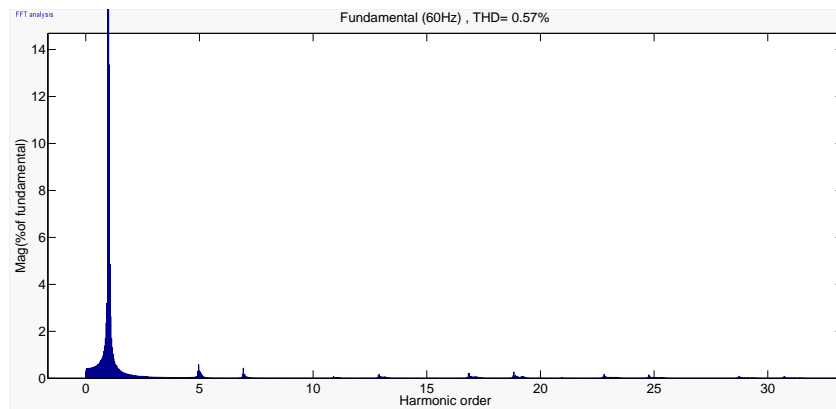


Figure 6.19: FFT Results After Harmonics Compensation

Table 6.2: HARMONICS VALUES OF DIFFERENT ORDER OF THE DC DFIG SYSTEM

Harmonics Order	Before Regulation	After Regulation
5	5.02%	0.34%
7	2.55%	0.12%
11	1.45%	0.03%
13	0.86%	0.03%
17	0.65%	0.07%
19	0.53%	0.02%

6.4 Simulation Results For Hybrid Observer Sensor-less Drive

6.4.1 Sensor-less Drive for squirrel cage machine

The hybrid observer sensor-less control performance is presented for applying to the squirrel cage induction machine in this section. The gain matrix of the Luenberger observer is kept as the 0 matrix to simplify the problem. For SMO, the initial guess of the rotor speed is $\hat{\omega}_{r0} = 0$ RPM and K_1 and K_2 of (12) are chosen as 4×10^5 and 5×10^4 respectively. The boundary layer was chosen as $\delta = 10$.

The induction machine's initial states are all zero. At 0s, the machine is first controlled to run at constant electrical speed of $\omega_r = 600$ RPM. The system is then facing three different command scenarios to test the performance: a positive step, a negative step and hold-to-zero speed. During the whole process there is no load attached to the shaft. In Figure 6.20 and 6.21 show the speed and a-phase current response to a positive step input at 5s; increasing the rotor speed from 600RPM to 900RPM. From Figure 6.20, the system takes around 0.1s to respond to the 300RPM positive step change, with a very small speed overshoot. The estimated speed from the observer is equal to the actual rotor speed. The current has a impulse at 5s to generate the acceleration torque, then comes back to the value that holds the magnetic field of the machine.

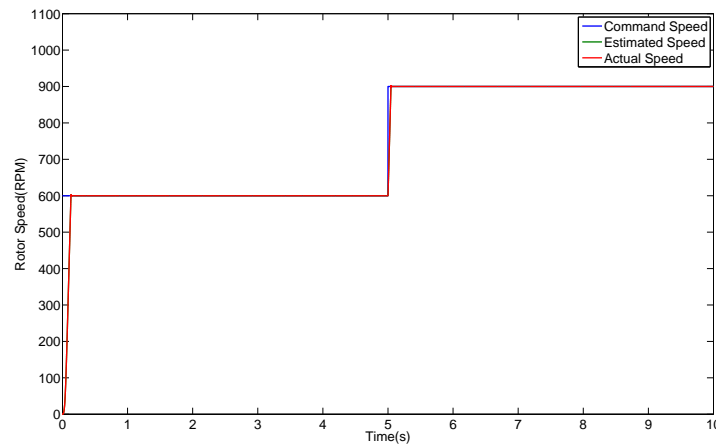


Figure 6.20: Speed response to a positive step

The speed and current response of the negative speed step is demonstrated in Figure 6.22 and 6.23. With a -1500RPM step, the rotor speed jumps from 600RPM to -900RPM in less than 0.2s. A big current jump happens at 5s to deaccelerate the machine speed, then goes back to steady-state values.

The zero speed condition has always been a challenge for speed-sensorless control. Figure 6.24 and

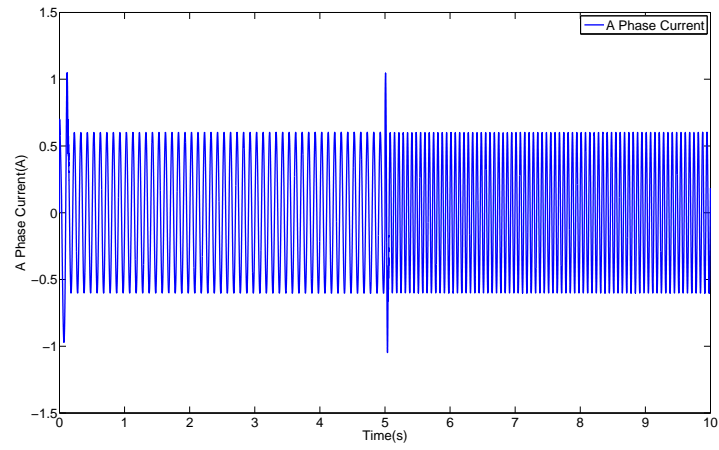


Figure 6.21: Current response to a positive step

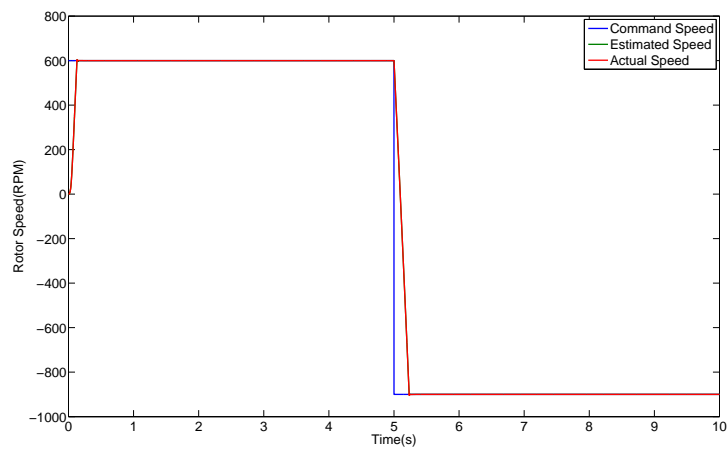


Figure 6.22: Speed response to a negative step

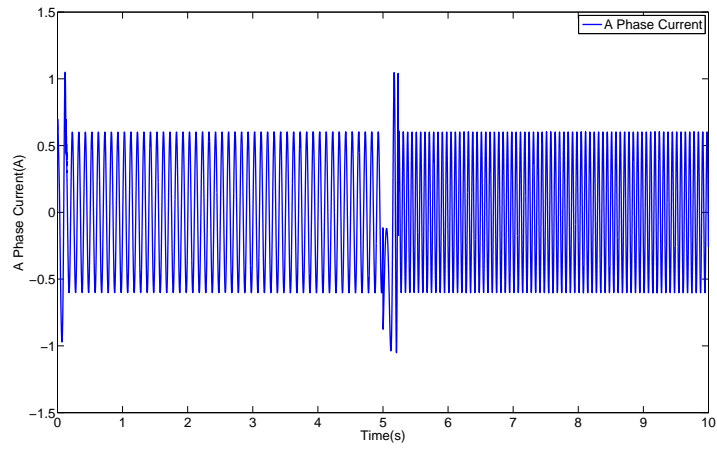


Figure 6.23: Current response to a negative step

6.25 show the behavior of the proposed hybrid observer under zero-speed operation. The rotor speed takes 0.1s from 600RPM to stabilize at zero speed. The current will generate an accordingly deceleration torque to bring the machine speed to zero, then the current will not goes to zero. The current value will keeps the very last value of the decelerate period.

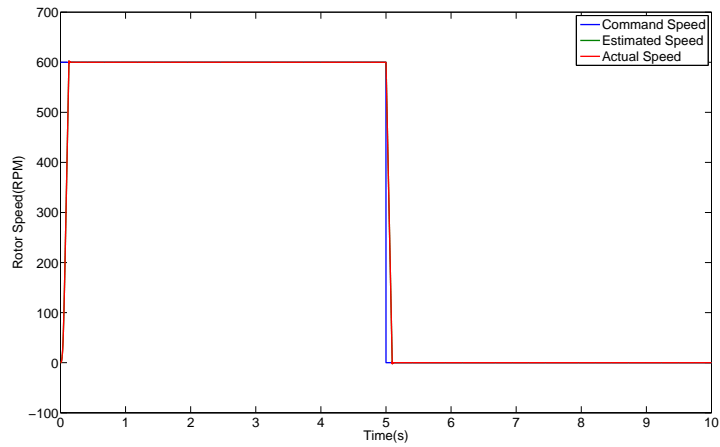


Figure 6.24: Speed response to a zero speed command

6.4.2 Sensor-less Drive for Wound Rotor Machine

To test the speed sensor-less algorithm of the hybrid observer presented in 5.2. The DFIG is facing a step up and step down in the simulation. The gain matrix of the Luenberger observer is picked as equation

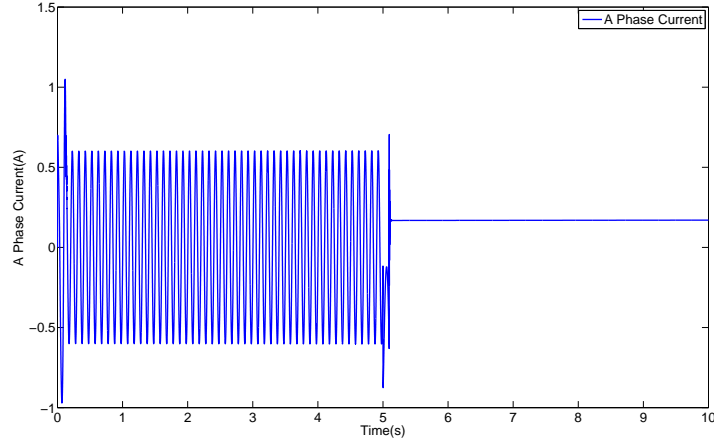


Figure 6.25: Current response to a zero speed command

(5.23), and constant g is picked as 1000.

For SMO, the initial guess of the rotor speed is $\hat{\omega}_{r0} = 0$ RPM and K_1 and K_2 of (12) are chosen as 2×10^5 and 1×10^4 respectively. The boundary layer was chosen as $\delta = 5$. As shown in Fig 6.26, the machine is running at 55Hz at the beginning. At 3.2 second the DFIG rotor electrical speed jumps to 60Hz. The rotor electrical speed steps down to 52Hz at 7.2 second. The green curve is the actual speed and the blue curve is the estimated speed from the hybrid observer. The simulation last 9 second, and the entire simulation period the estimated speed is tracing the actual rotor speed.

The first stage of the simulation, the machine is running from zero speed to 52Hz. From 0 to almost 1 second the estimated speed has a big oscillation. After the transit period, the estimated speed enters the steady state, the chattering is around 1%. When the machine is facing a positive speed step, the estimated speed from the hybrid observer will have a overshoot, the transit period is very short. At 7.2 second, the machine rotor speed is step down from 60Hz to 52Hz. After a big overshoot, the estimated speed has a 0.5s transit period then enters the steady state.

The Figure 6.27, 6.28 elaborates the d-axis stator and rotor current behavior when facing a positive speed step. In Figure 6.28 the current i'_{dr0} is the rotor current referred to the stator value. Both stator and rotor currents will increase the frequency and the amplitude at 3.2second, when the speed step occurs.

The Figure 6.29, 6.30 shows the d-axis stator and rotor current behavior when facing a negative speed step. Both stator and rotor currents will decrease the frequency and the amplitude at 7.2second, when the speed step occurs.

In Figure 6.27, 6.28, 6.29, 6.30 the estimated currents from the hybrid observer are able trace the

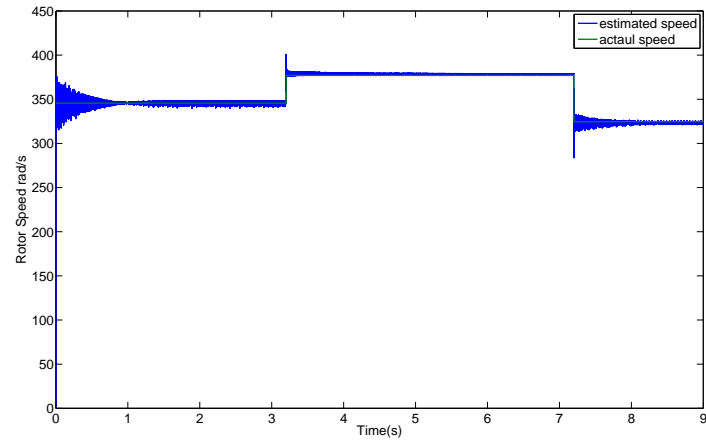


Figure 6.26: Speed response of the hybrid observer for DFIG

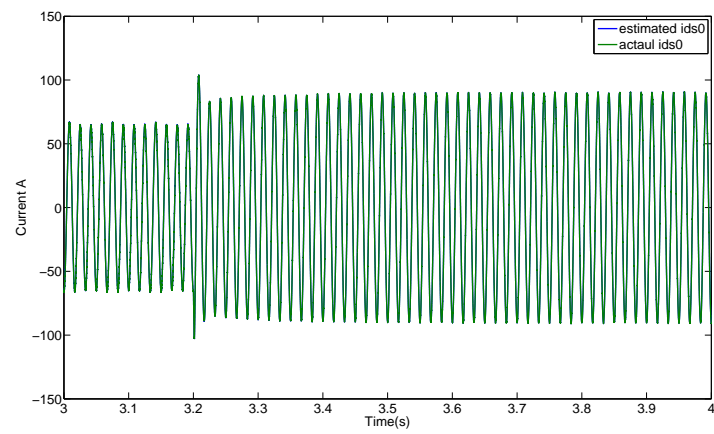


Figure 6.27: Stator current response to a positive speed step

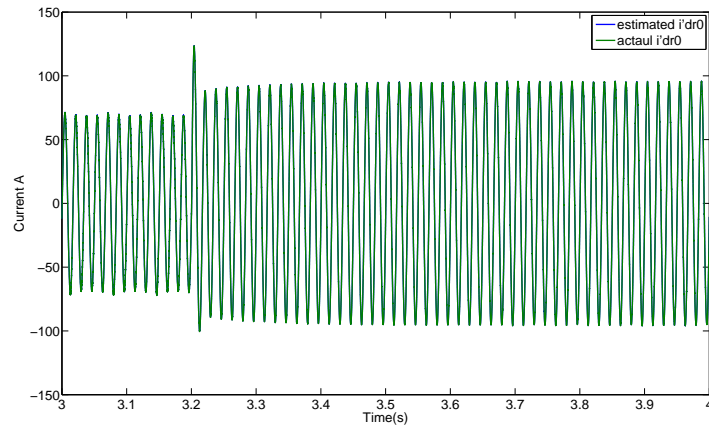


Figure 6.28: Rotor current response to a positive speed step

actual current the entire time, even during the transit period.

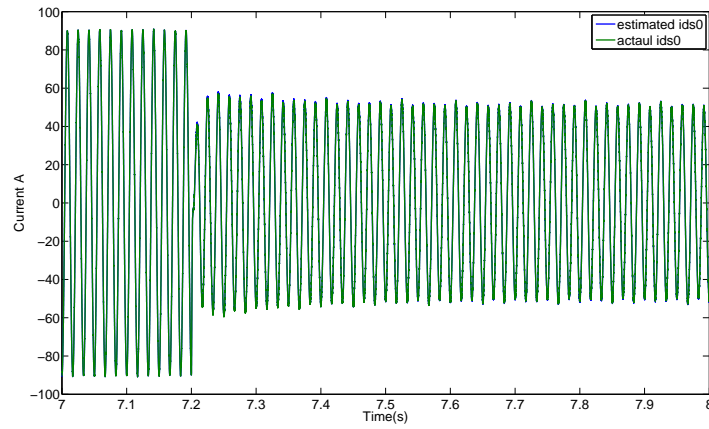


Figure 6.29: Stator current response to a negative speed step

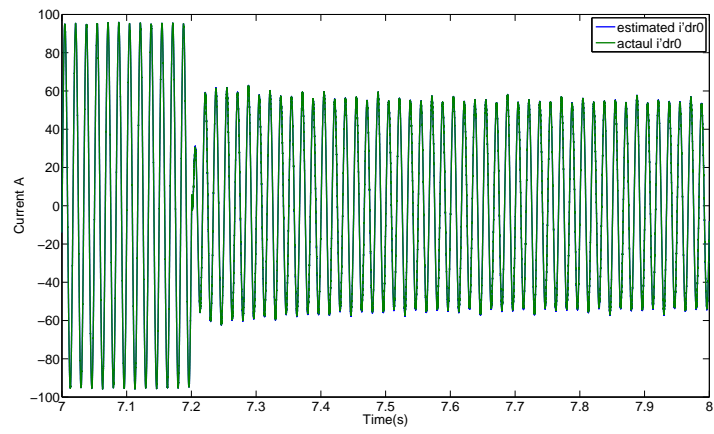


Figure 6.30: Rotor current response to a negative speed step

Chapter 7

Experimental Results

7.1 Experimental Results For AC DFIG System

The hardware setup is shown as in Figure 7.1. The DFIG (on the left) is driven by a dc motor (on the right). The dc motor is controlled using a SCR 4 quadratic algorithm. The control is a speed control, the reference speed will compare with the real speed and the error compare with armature current of the machine to generate the switching signals.



Figure 7.1: Lab Hardware Setup

The power converter and the LCL filter is shown in Figure. 7.2. The IGBT power converter is the Semikron IGD-1-424-P1N4-DL-FA. The LCL filter is chosen as $L_1 = 0.85mH$, $L_2 = 0.3mH$, $C=80\mu f$. The

micro controller to control the converter FPGA based NI single board sbRIO-9607. To have a better interface between sbRIO-9607 to the power converter, a interface PCB board is also designed as presented in Figure 7.3.



Figure 7.2: Converter Cabin

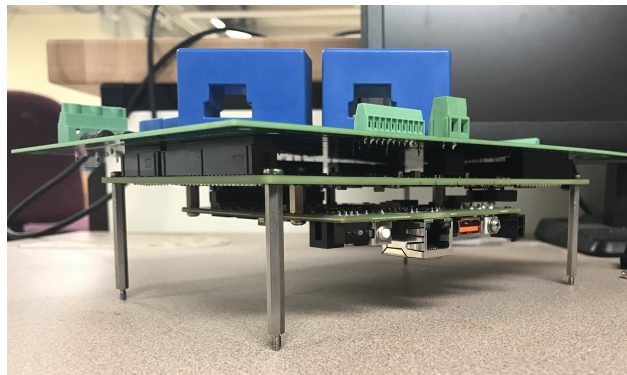


Figure 7.3: sbRIO-9607 Attached with Interface Board

The DFIG is a 40hp machine. The DFIG has been down-grade the machine to 15Kw to meet the safety require of the Clemson University. Because the machine is down-grade so the machine is given a reference power equals to 13Kw with all the wind speed.

When the machine is operates during sub-synchronous mode. With a slip s equals to 10% The stator

current waveform is shown in figure 7.4. With the reference active power of the stator being 13Kw, the stator is suppose to have a current with the amplitude of 50 A.

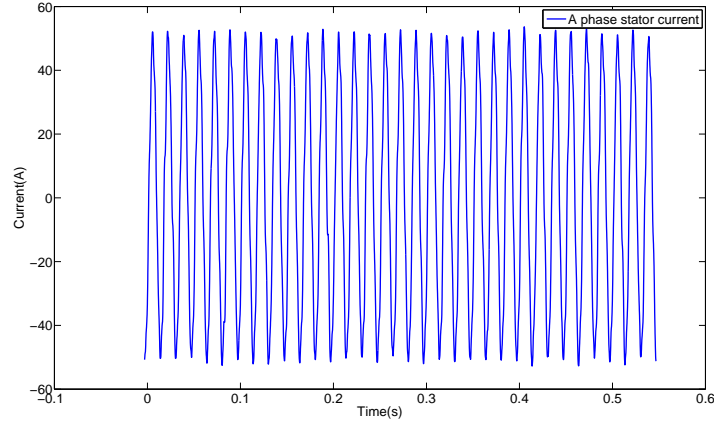


Figure 7.4: Stator A Phase Sub-synchronous Mode

With the synchronous speed 60Hz, the rotor will have a current rotating at slip frequency which is 10% of the synchronous speed 6Hz. The rotor current waveform is shown in figure 7.5.

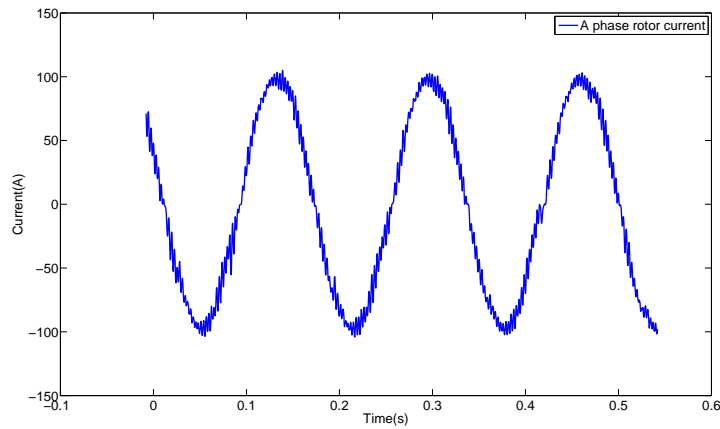


Figure 7.5: Rotor A Phase Sub-synchronous Mode

The GSC is there to hold the dc-link voltage, at the GSC current will also has the same grid frequency equals to 60Hz. The GSC current waveform is shown in figure 7.6.

The Figure 7.7 present the performance of the RSC. With a reference power equals to 13Kw the RSC is able to trace the power.

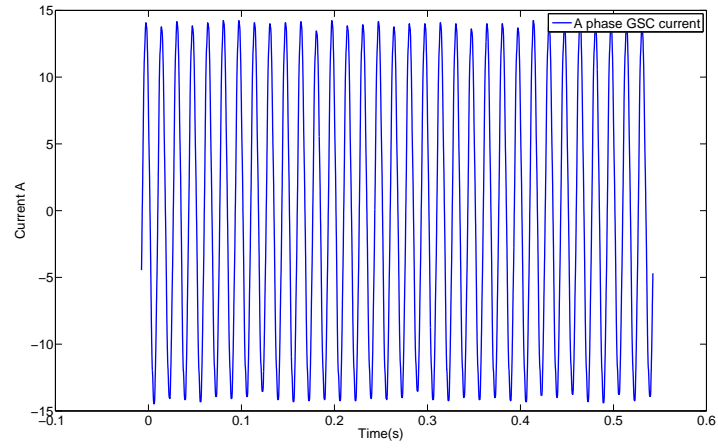


Figure 7.6: GSC A Phase Sub-synchronous Mod

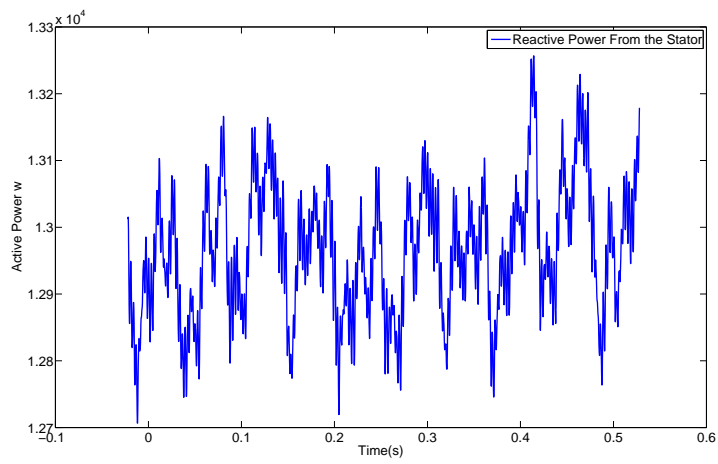


Figure 7.7: Active Power From the Stator Sub-synchronous Mode

Theoretically, the rotor active power should follows the equation:

$$P_r = -SP_s \quad (7.1)$$

In equation (7.1): S is the slip, P_r, P_s is the rotor and stator active power. With a $S = 10\%$ The rotor is supposed to draw around 1.3Kw from the grid. The rotor active power is shown in Figure7.8

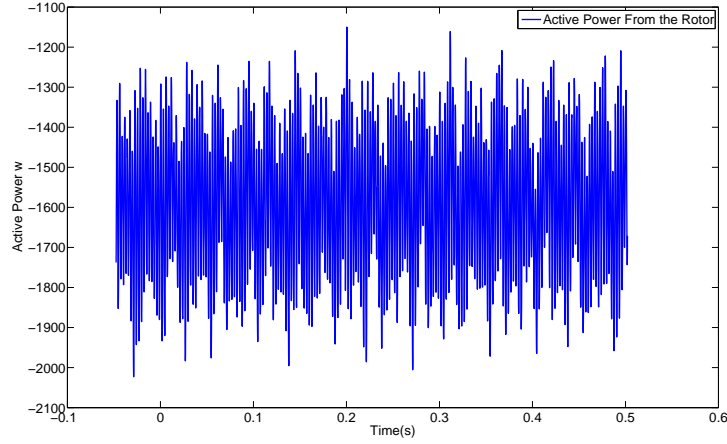


Figure 7.8: Active Power From the Stator Sub-synchronous Mode

The power converter is rating at the apparent power of the DFIG, it is common to command the DFIG to have a unit power factor. The unit power factor will lead to a zero reactive power. The reactive power of the stator and rotor is shown in Figure 7.9 and 7.10

When the machine is operates during synchronous mode. With a slip s equals to 0. The stator will still rotating at 60Hz, while the rotor will have a dc current. The stator and rotor current waveform is show in Figure 7.11 and 7.12 respectively.

The GSC current will still have the frequency equals 60Hz, the current is as shown in Figure 7.13

With a zero slip, the power transfered between the rotor and the grid is expected to be zero. The active power of the stator and rotor is shown in Figure 7.14, 7.15. The reactive power of the stator and rotor is shown in Figure 7.16 and 7.17.

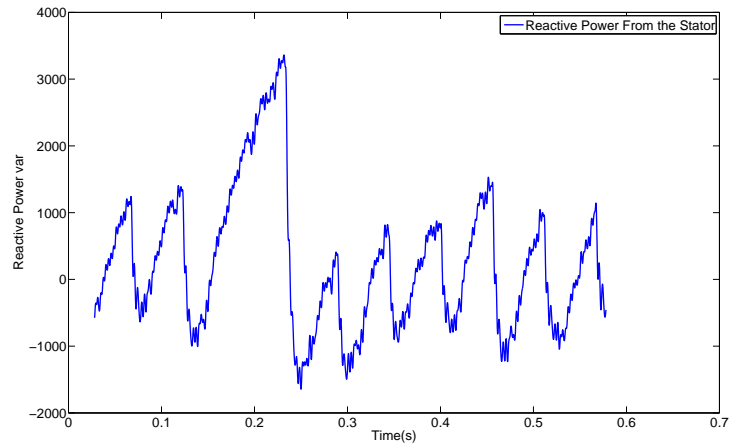


Figure 7.9: Reactive Power From the Stator Sub-synchronous Mode

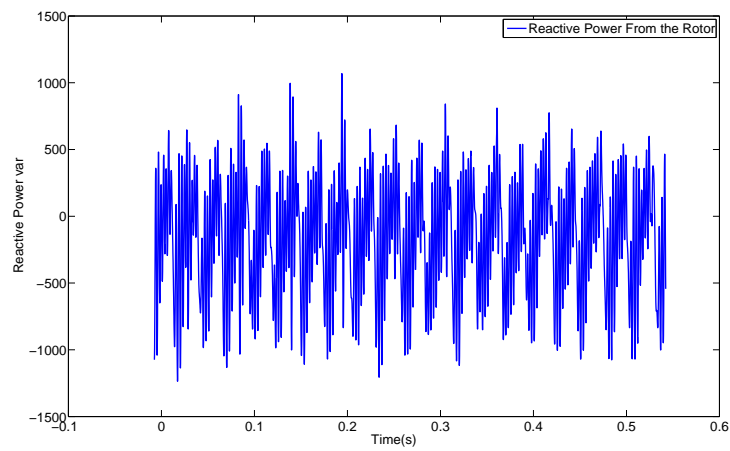


Figure 7.10: Reactive Power From the Rotor Sub-synchronous Mode

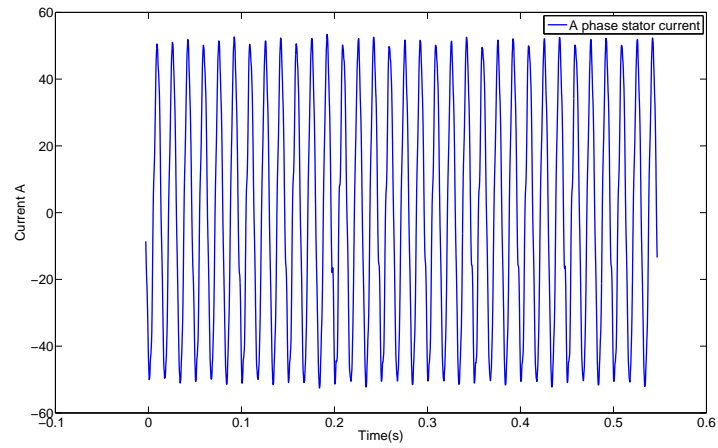


Figure 7.11: Stator A Phase Synchronous Mode

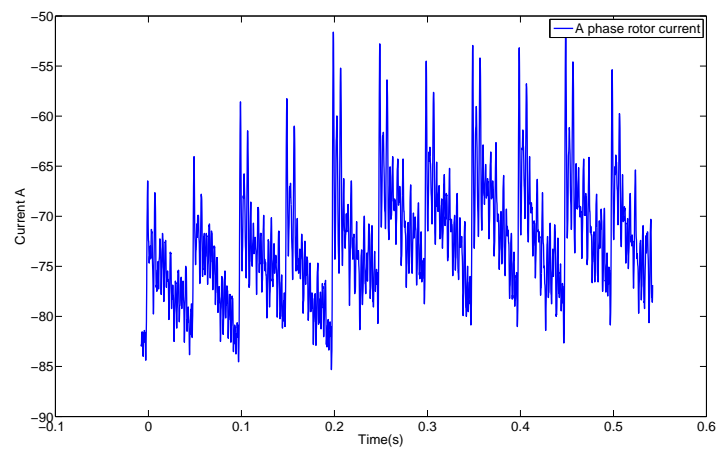


Figure 7.12: Rotor A Phase Synchronous Mode

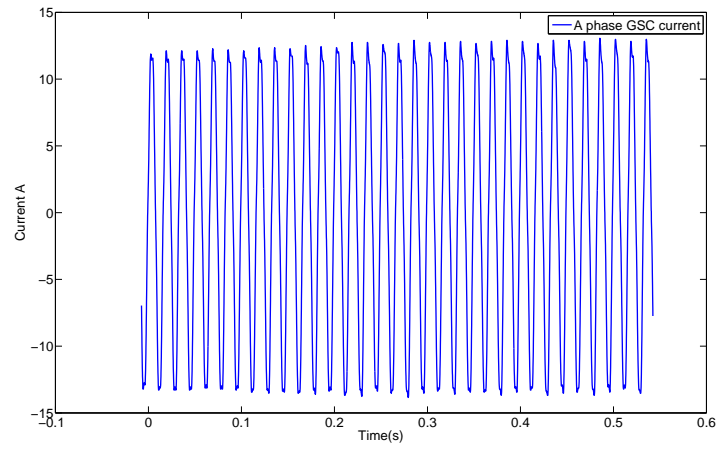


Figure 7.13: GSC A Phase Synchronous Mode

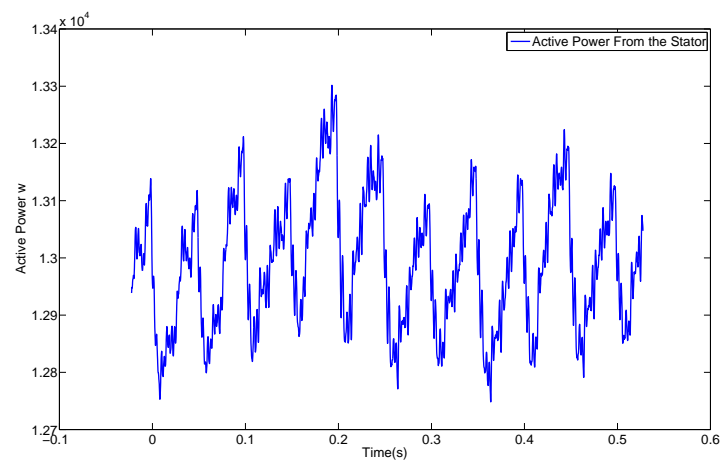


Figure 7.14: Active Power From the Stator Synchronous Mode

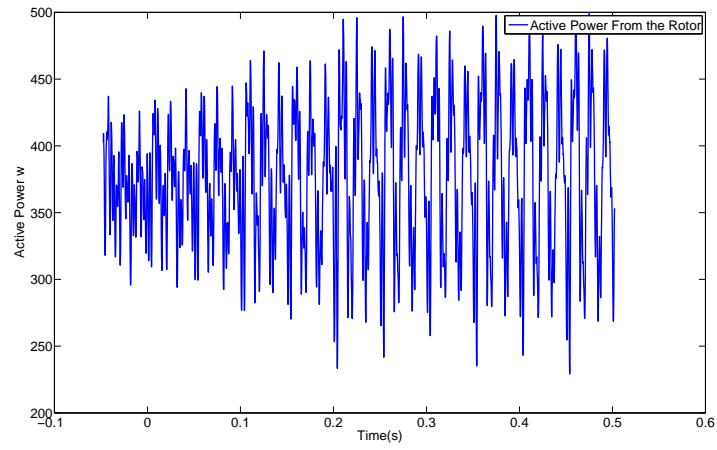


Figure 7.15: Active Power From the Rotor Synchronous Mode

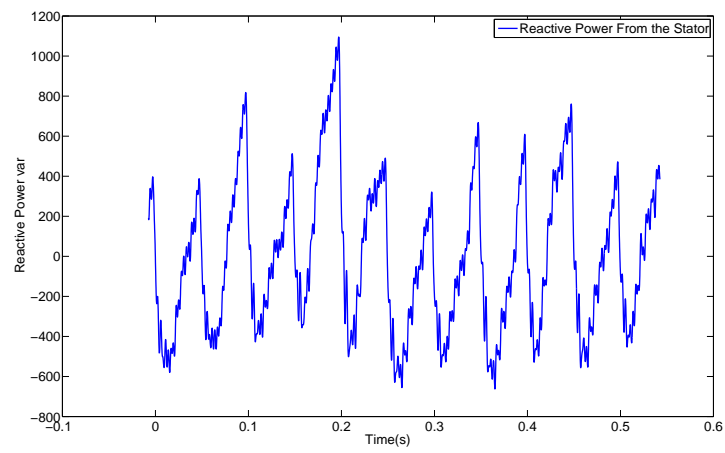


Figure 7.16: Reactive Power From the Stator Synchronous Mode

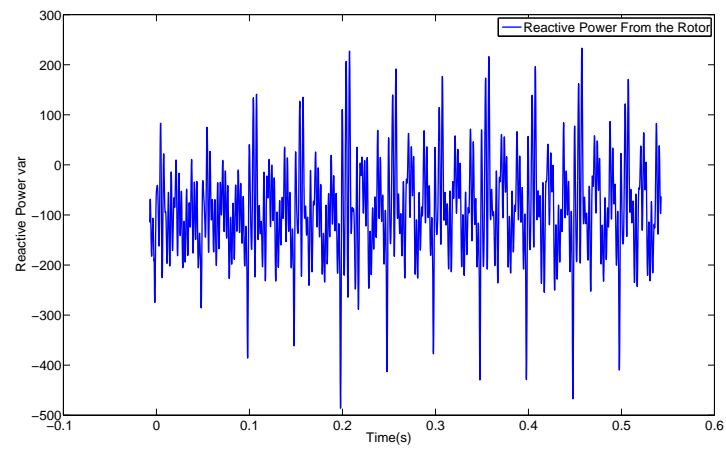


Figure 7.17: Reactive Power From the Rotor Synchronous Mode

When the machine is operates during super-synchronous mode. With a slip s equals to -10%, the rotor is now faster than synchronous speed, the rotor current frequency will be 6Hz. The current of the machine stator, rotor and the GSC are displayed down below in Figure 7.18, 7.19 and 7.20

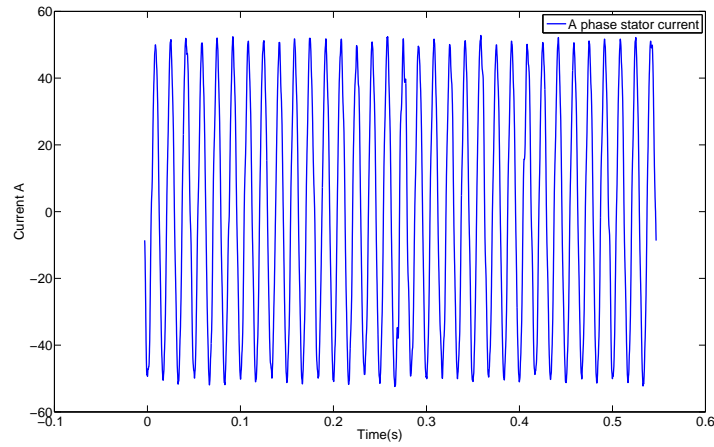


Figure 7.18: Stator A Phase Super-synchronous Mode

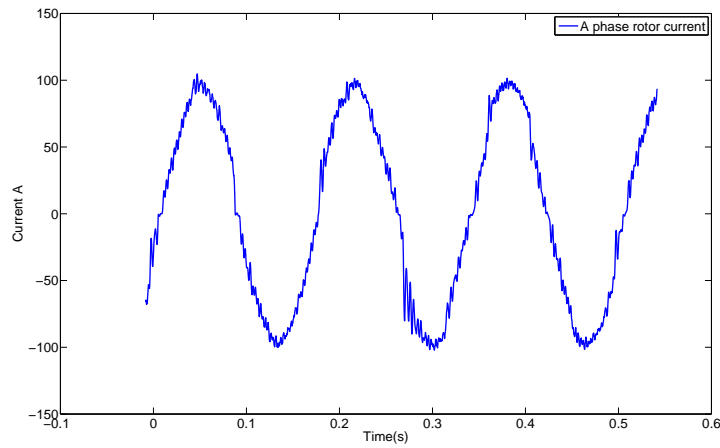


Figure 7.19: Rotor A Phase Super-synchronous Mode

Under the super-synchronous mode, both the stator and the rotor are transfer power to the grid. The active power of the stator and rotor is shown in Figure 7.21, 7.22.

With a unit power factor the reactive power of the stator and rotor is zero under super-synchronous mode.

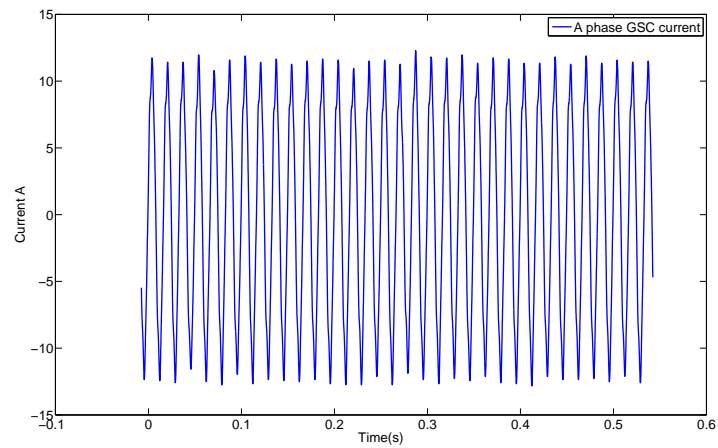


Figure 7.20: GSC A Phase Super-synchronous Mode

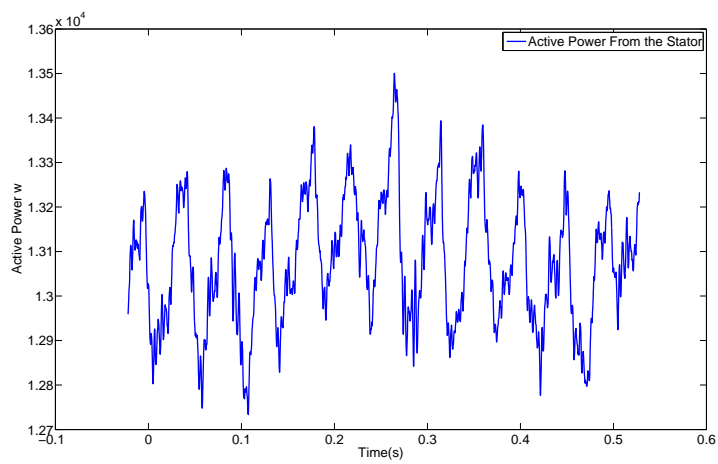


Figure 7.21: Active Power From the Stator Super-synchronous Mode

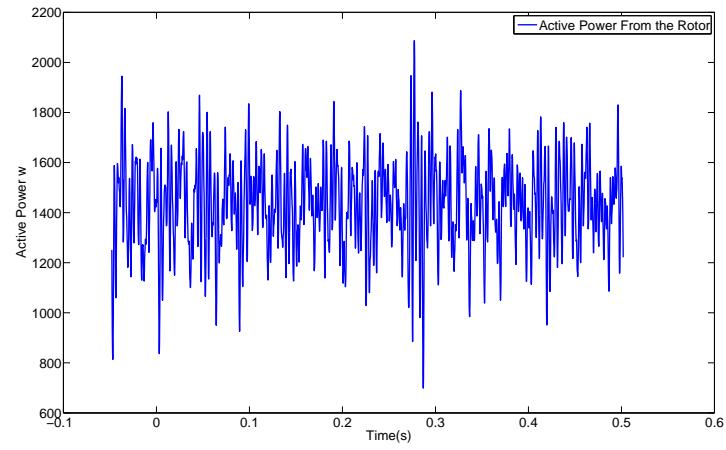


Figure 7.22: Active Power From the Rotor Super-synchronous Mode

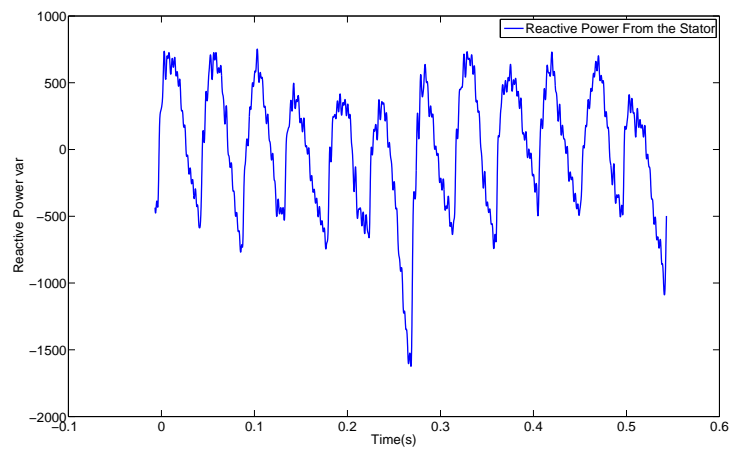


Figure 7.23: Reactive Power From the Stator Super-synchronous Mode

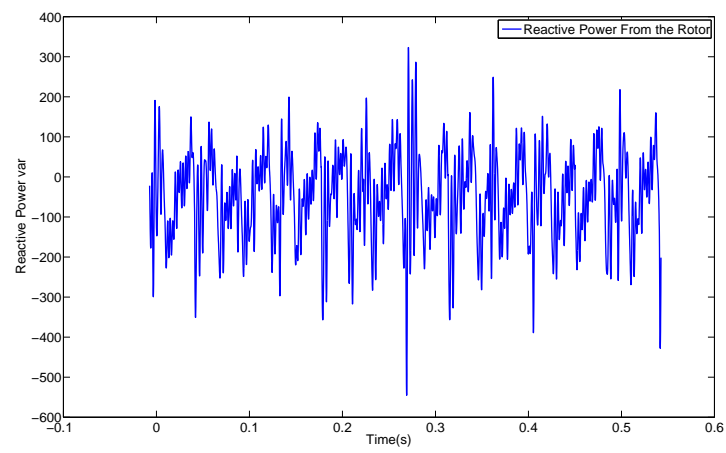


Figure 7.24: Reactive Power From the Rotor Super-synchronous Mode

7.2 Experimental Results Multiple Reference Frame Based Harmonics Regulation For AC DFIG System

With the nonlinear load connected to the PCC of the three phase ac DFIG system. Harmonics will be drawn to the grid. The three phase diode bridge connect a 34 ohms resistor bank is the nonlinear load used in the lab. The current draw from the grid to the load is shown in Figure 7.26 Unlike the running the

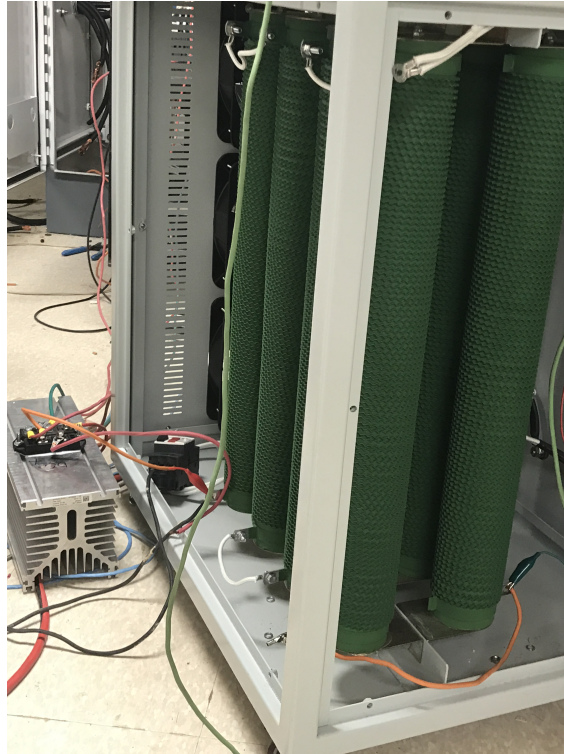


Figure 7.25: Nonlinear Load in Lab

simulation, which is in a ideal environment. Conducting the experimental in the lab, harmonics will also been seen in the stator current. In this section, the RSC is used to compensate the harmonics in the stator and GSC will compensate the harmonics in drawn from the non-linear load. When the nonlinear load connect to the PCC the stator current waveform is as in Figure 7.27 Running the FFT to the stator current. The Figure 7.28 shows the most significant harmonics is at 5th order.

The rotor current is shown in Figure 7.29 The GSC current before the compensation is shown as Figure 7.30

The current flows into the grid follows equation (4.2) is shown as Figure 7.31

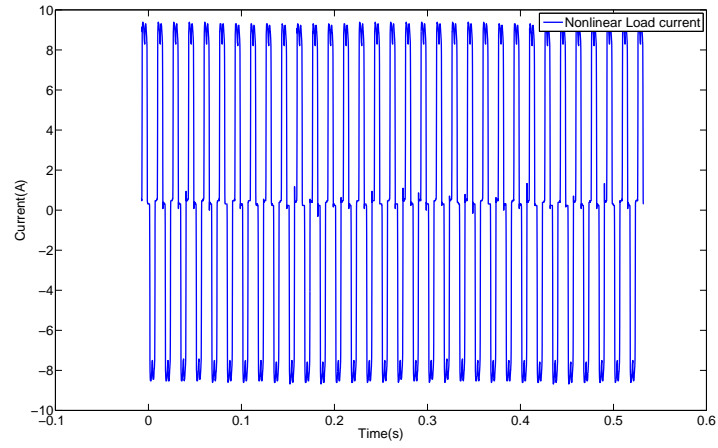


Figure 7.26: Nonlinear Load Current

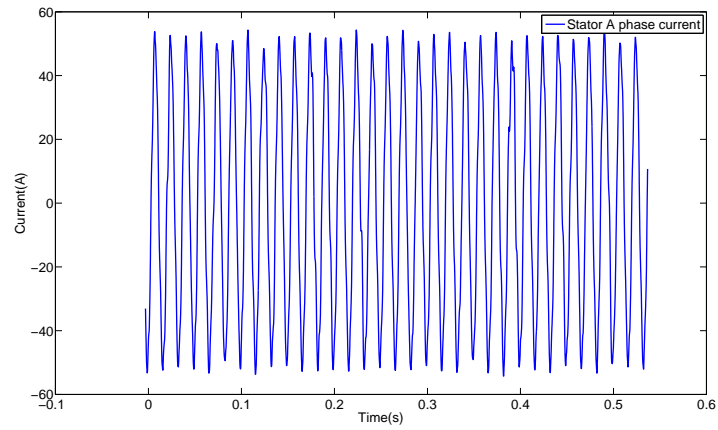


Figure 7.27: Stator Current With Nonlinear Load Connect to PCC Sub-Synchronous Mode

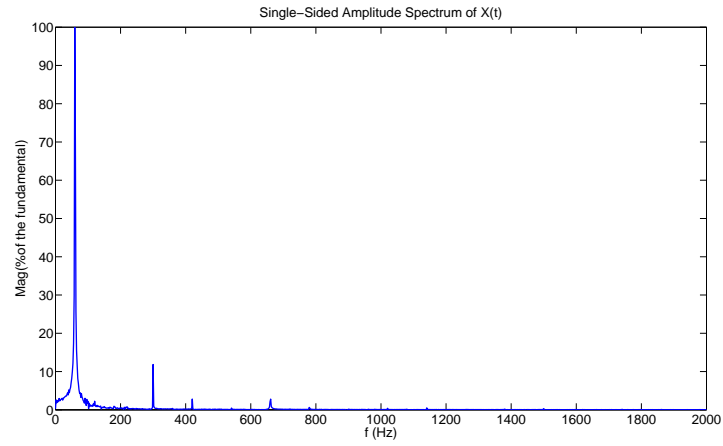


Figure 7.28: FFT of The Stator Current Sub-Synchronous Mode

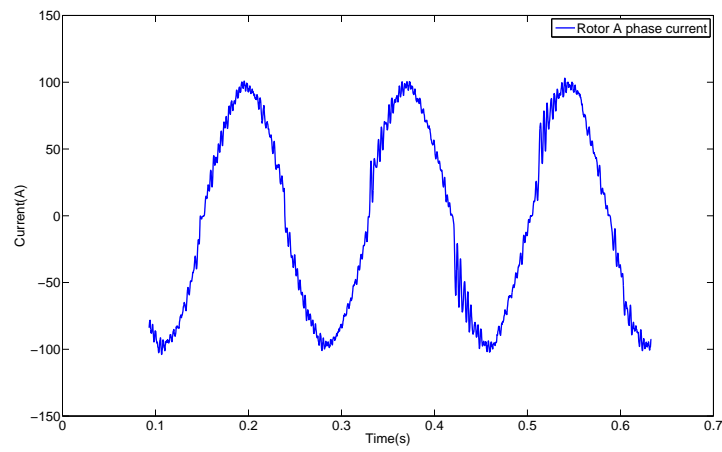


Figure 7.29: Rotor Current With Nonlinear Load Connect to PCC Sub-Synchronous Mode

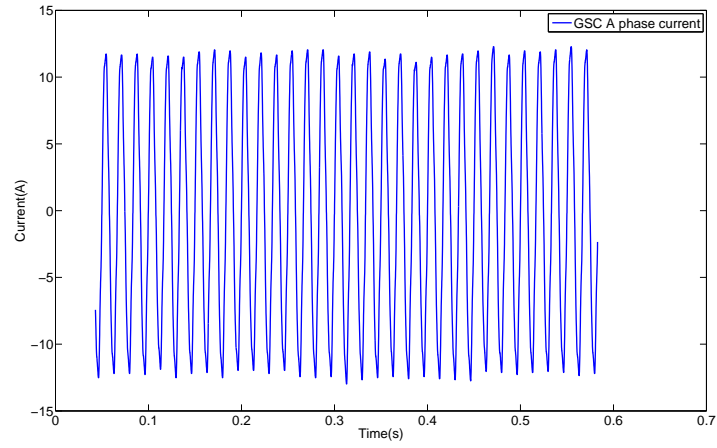


Figure 7.30: GSC Current With Nonlinear Load Connect to PCC Sub-Synchronous Mode

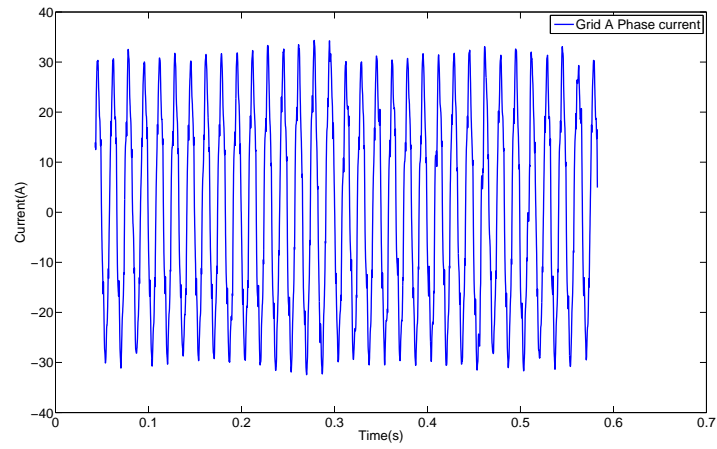


Figure 7.31: Grid Current With Nonlinear Load Connect to PCC Sub-Synchronous Mode

Running FFT for the grid current the results is shown in Figure 7.32

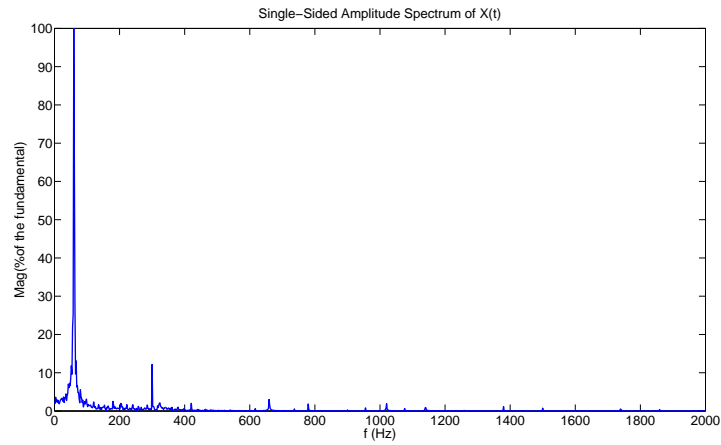


Figure 7.32: FFT of The Grid Current Sub-Synchronous Mode

Using a Multiple Reference Frame harmonics estimator to estimate the harmonics in stator and grid current. Applying the RSC and GSC to compensate the harmonics, the result for the sub-synchronous mode will be presented below.

The stator current is compensated by the rotor current using RSC 7.33.

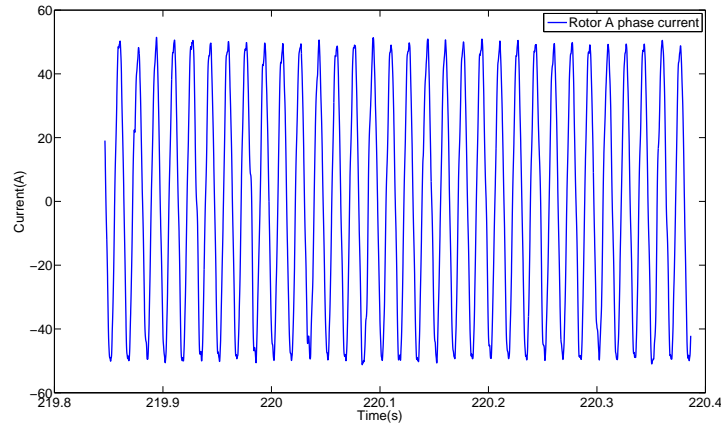


Figure 7.33: Stator Current After the Compensation Sub-Synchronous Mode

Applying FFT algorithm to the stator current after compensation the results shows in Figure 7.34 proves that the 5th order harmonics has been compensated. The rotor current changes to Figure 7.35

The nonlinear load current is compensated by the GSC current. The current waveform after com-

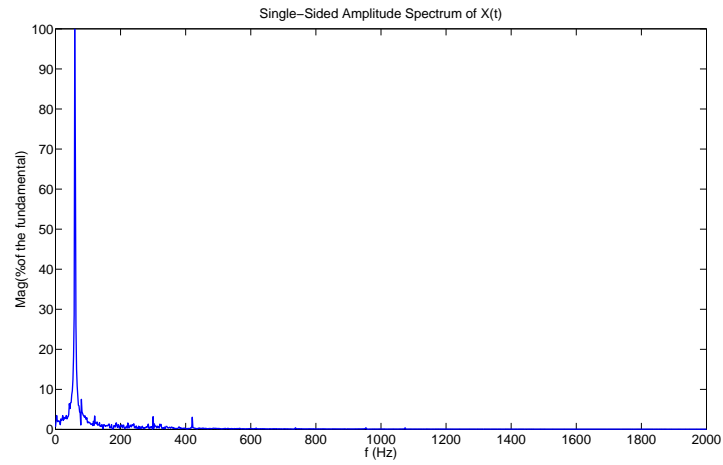


Figure 7.34: Stator Current FFT After the Compensation Sub-Synchronous Mode

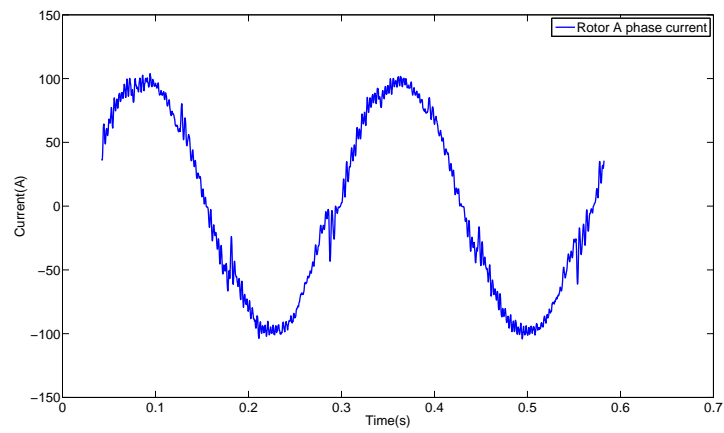


Figure 7.35: Rotor Current After the Compensation Sub-Synchronous Mode

pensation and the FFT results is presented in Figure 7.36 and 7.37.

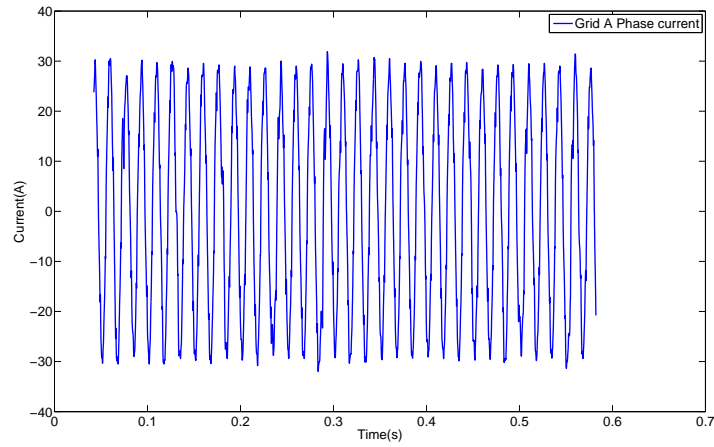


Figure 7.36: Grid Current After the Compensation Sub-Synchronous Mode

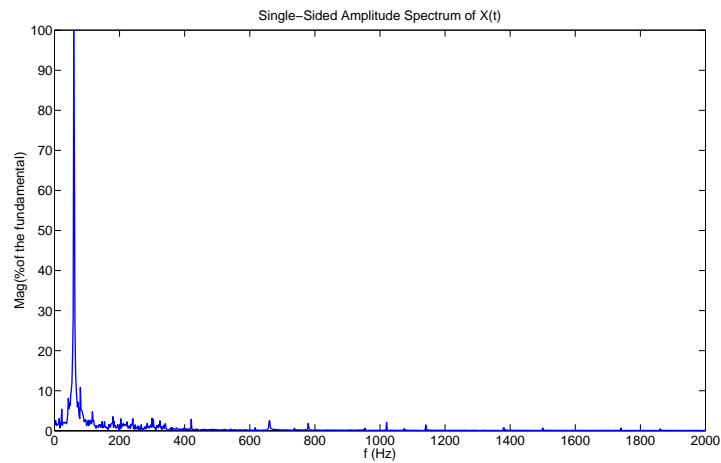


Figure 7.37: Grid Current FFT After the Compensation Sub-Synchronous Mode

The GSC current changes to Figure 7.38

Similar approaches can be applied to the machine running at synchronous speed and super synchronous mode. Under synchronous mode the stator current before the compensation is Figure 7.39 Running the FFT to the stator current. The Figure 7.40 shows the most significant harmonics is at 5th order.

The rotor current is shown in Figure7.41

The GSC current before the compensation is shown as Figure 7.42

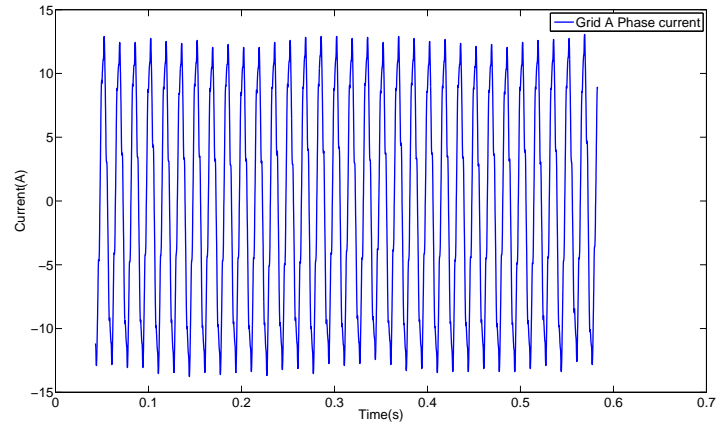


Figure 7.38: GSC Current After the Compensation Sub-Synchronous Mode

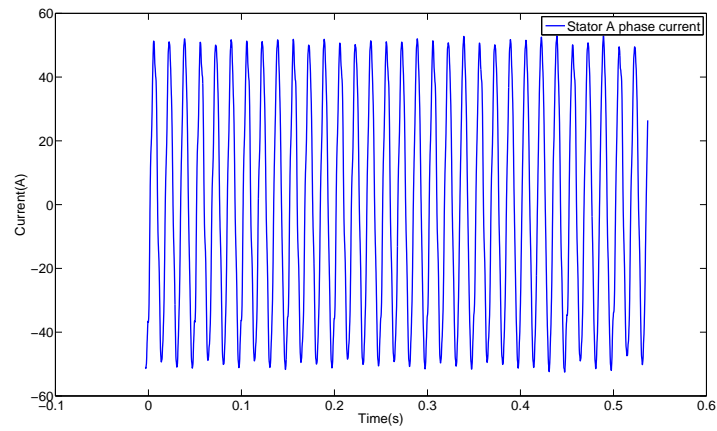


Figure 7.39: Stator Current With Nonlinear Load Connect to PCC Synchronous Mode

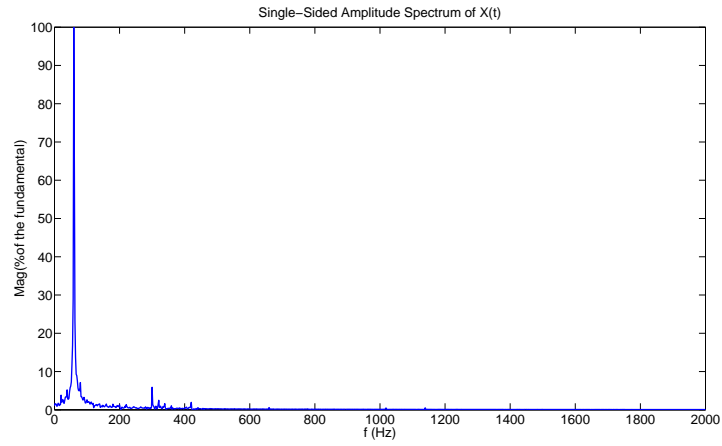


Figure 7.40: FFT of The Stator Current Synchronous Mode

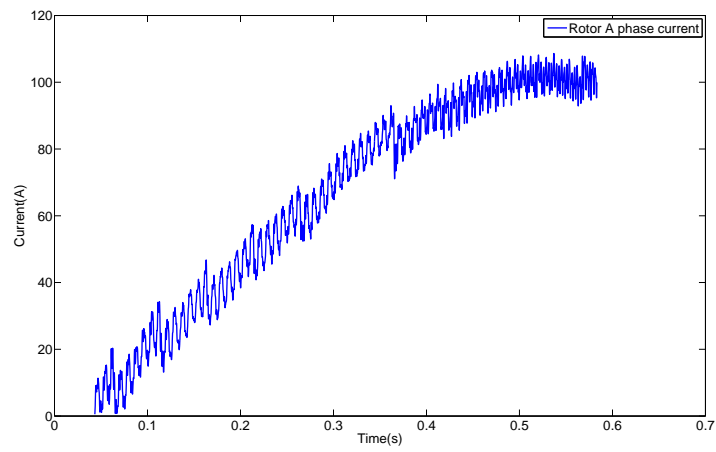


Figure 7.41: Rotor Current With Nonlinear Load Connect to PCC Synchronous Mode

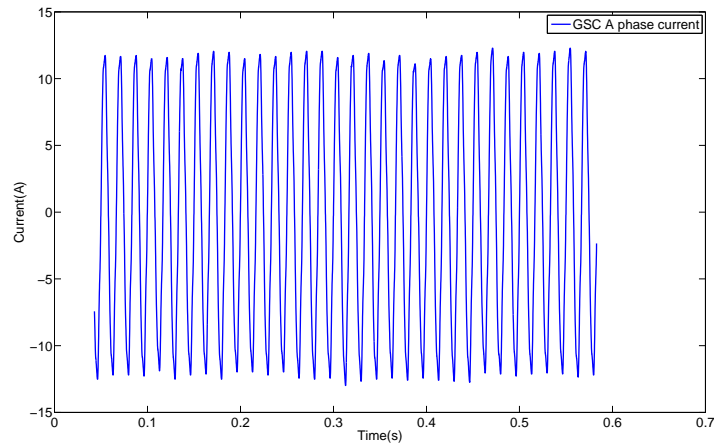


Figure 7.42: GSC Current With Nonlinear Load Connect to PCC Synchronous Mode

The current flows into the grid is shown as Figure 7.43

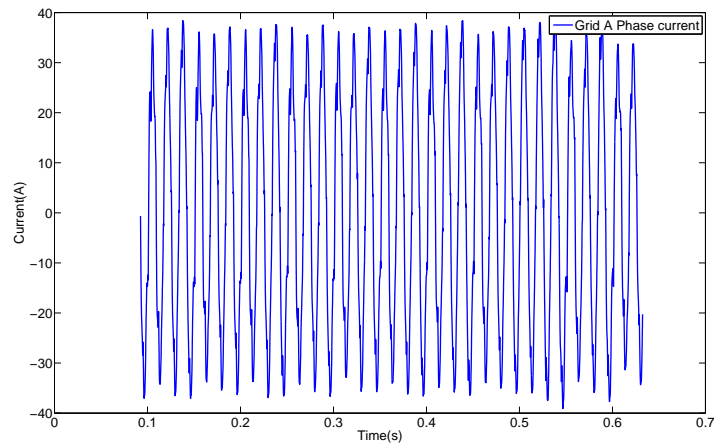


Figure 7.43: Grid Current With Nonlinear Load Connect to PCC Synchronous Mode

Running FFT for the grid current the results is shown in Figure 7.44

The stator current is compensated by the rotor current using RSC, the stator current waveform is Figure 7.45.

Running FFT for the grid current the results is shown in Figure 7.46

The rotor current changes to Figure 7.47

The grid current waveform after compensation and the FFT results is presented in Figure 7.48 and

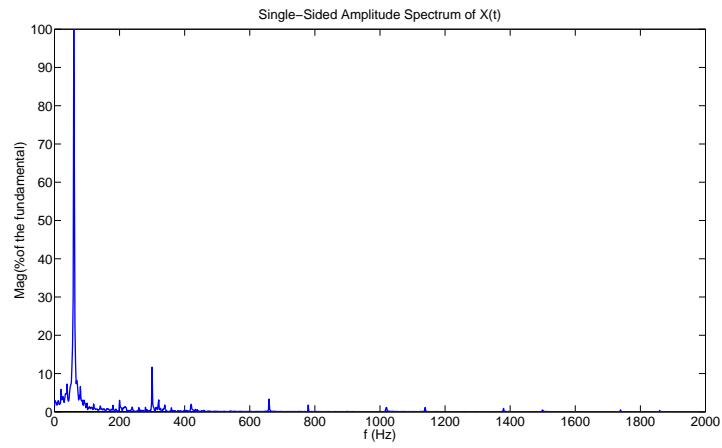


Figure 7.44: FFT of The Grid Current Synchronous Mode

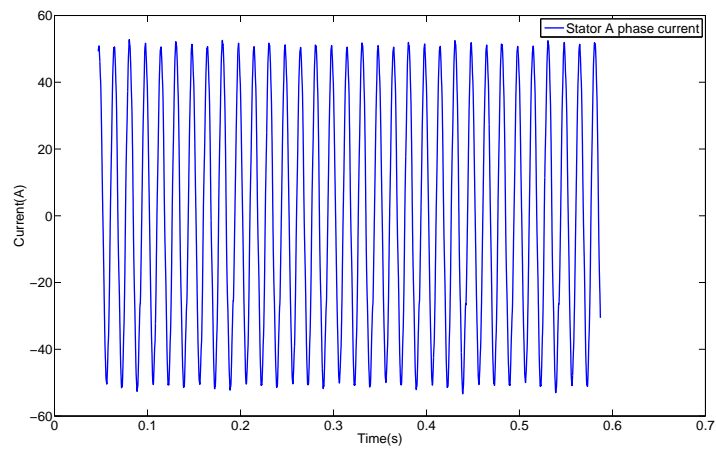


Figure 7.45: Stator Current After the Compensation Synchronous Mode

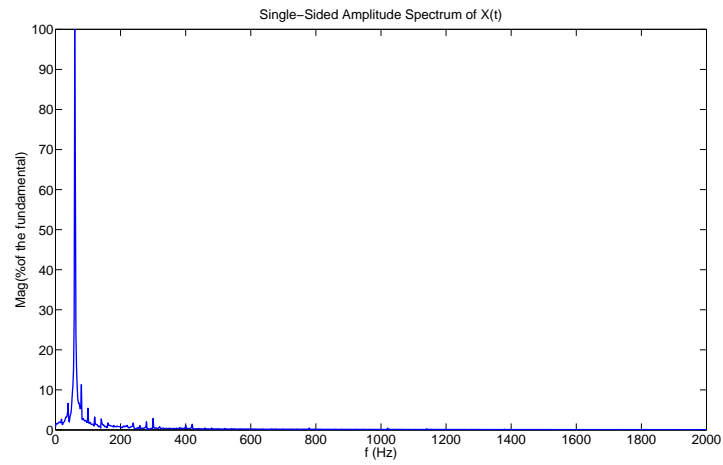


Figure 7.46: Stator Current FFT After the Compensation Synchronous Mode

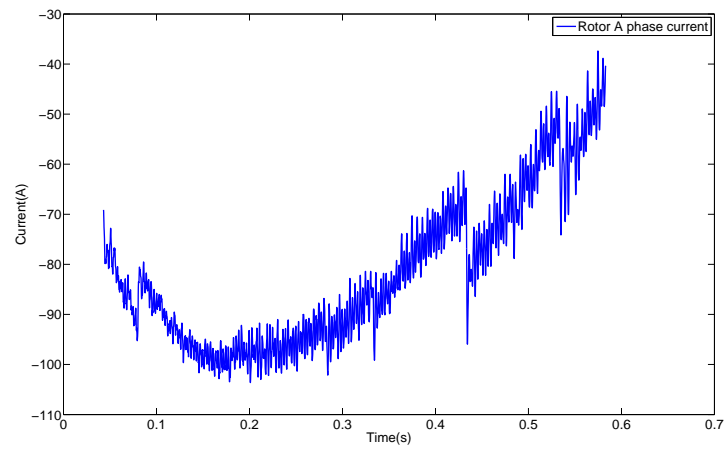


Figure 7.47: Stator Current After the Compensation Synchronous Mode

7.49.

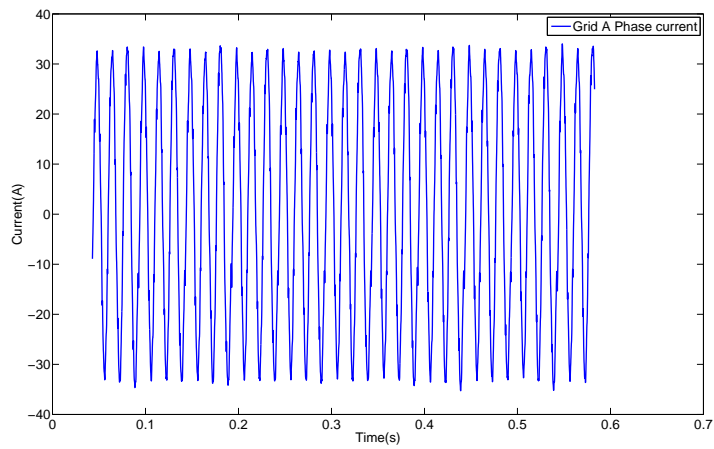


Figure 7.48: Grid Current After the Compensation Synchronous Mode

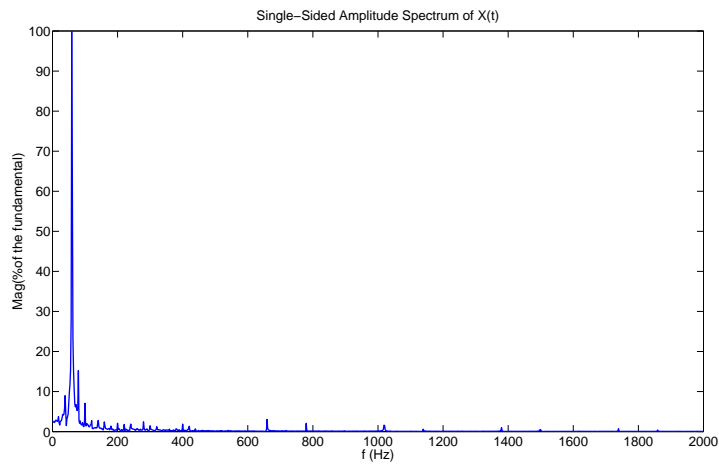


Figure 7.49: Grid Current FFT After the Compensation Synchronous Mode

The GSC current changes to Figure 7.50

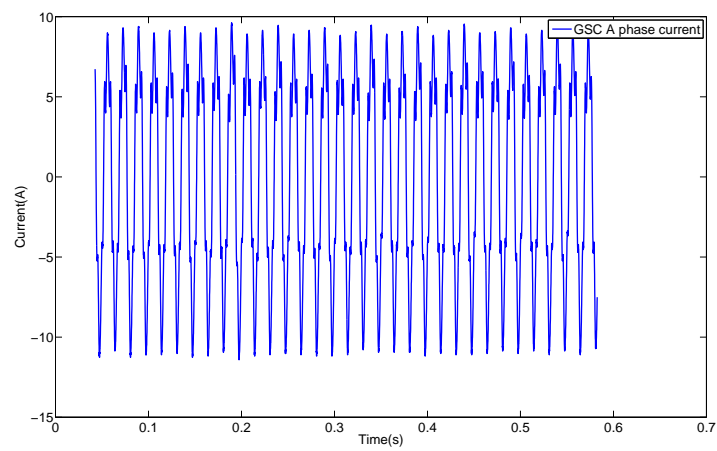


Figure 7.50: GSC Current After the Compensation Synchronous Mode

The stator current before the compensation when driving at super-synchronous mode waveform and FFT results is shown in Figure 7.51, 7.52

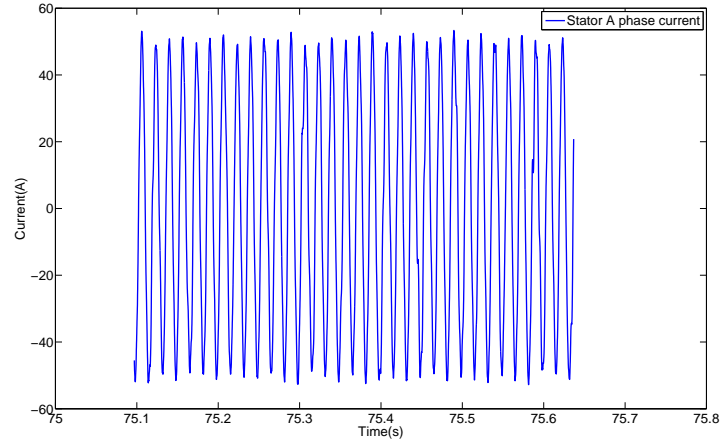


Figure 7.51: Stator Current With Nonlinear Load Connect to PCC Super-Synchronous Mode

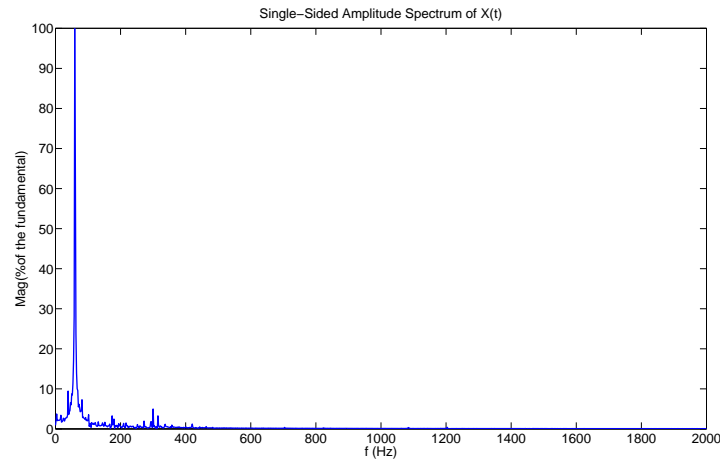


Figure 7.52: FFT of The Stator Current Super-Synchronous Mode

The rotor current is shown in Figure 7.53

The GSC current before the compensation is shown as Figure 7.54

The current flows into the grid is shown as Figure 7.55

Running FFT for the grid current the results is shown in Figure 7.56

The stator current is compensated by the rotor current using RSC, the stator current waveform is

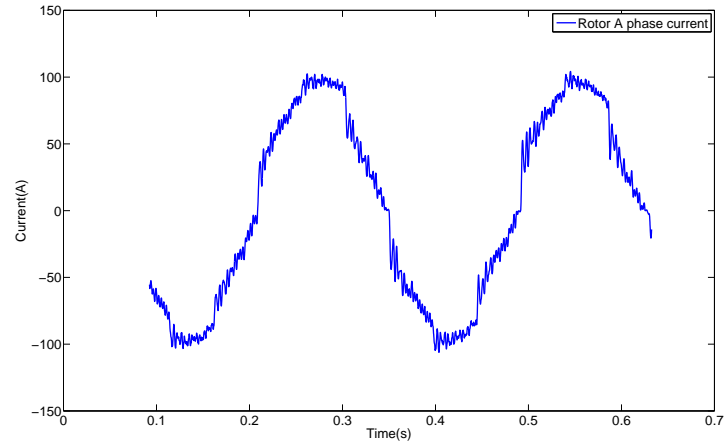


Figure 7.53: Rotor Current With Nonlinear Load Connect to PCC Super-synchronous Mode

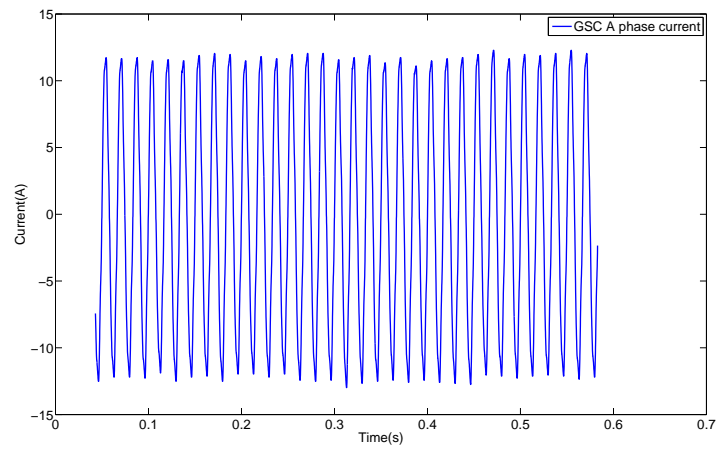


Figure 7.54: GSC Current With Nonlinear Load Connect to PCC Super-synchronous Mode

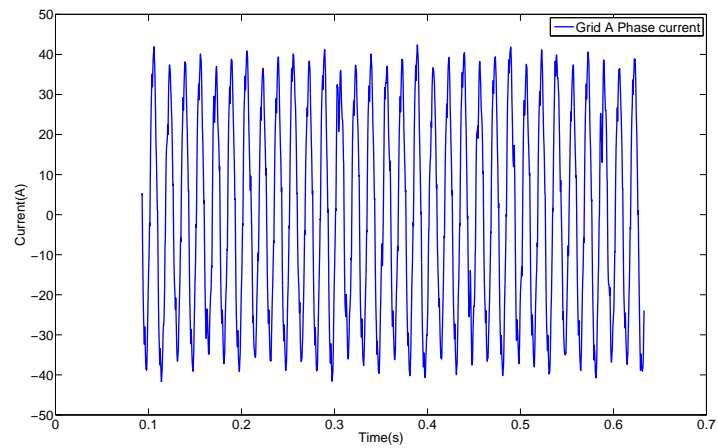


Figure 7.55: Grid Current With Nonlinear Load Connect to PCC Super-synchronous Mode

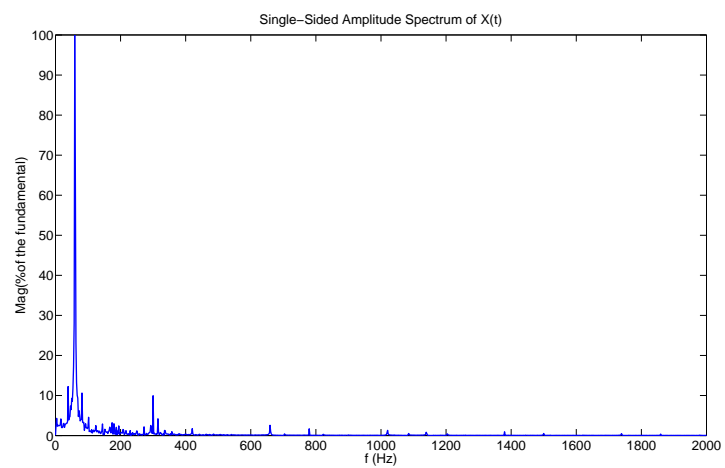


Figure 7.56: FFT of The Grid Current Super-synchronous Mode

Figure 7.57.

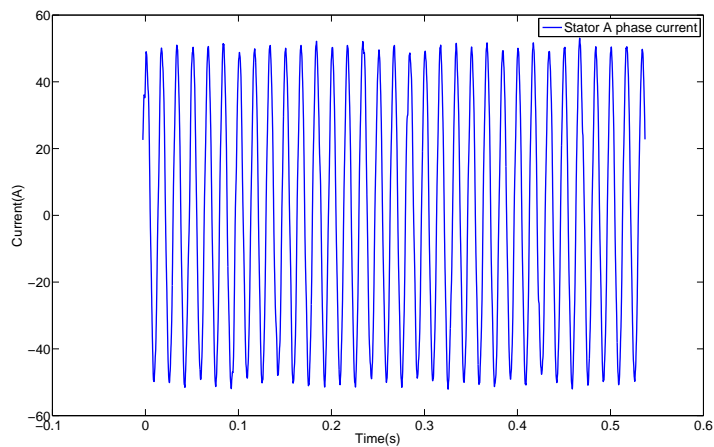


Figure 7.57: Stator Current After the Compensation Super-synchronous Mode

Running FFT for the grid current the results is shown in Figure 7.58

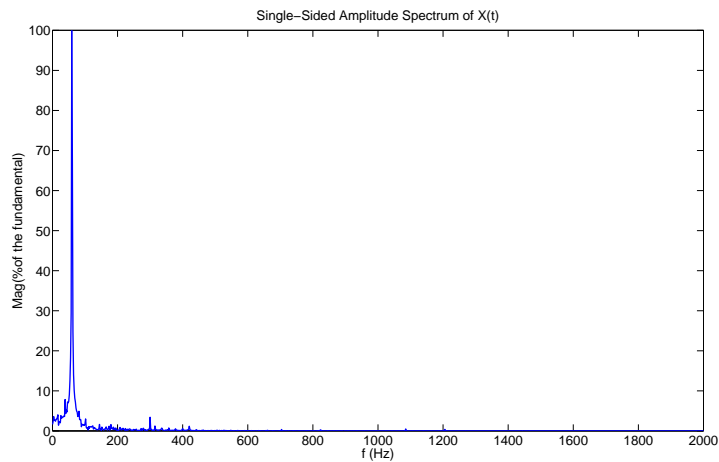


Figure 7.58: Stator Current FFT After the Compensation Super-synchronous Mode

The rotor current changes to Figure 7.59

The grid current waveform after compensation and the FFT results is presented in Figure 7.60 and

7.61.

The GSC current changes to Figure 7.62

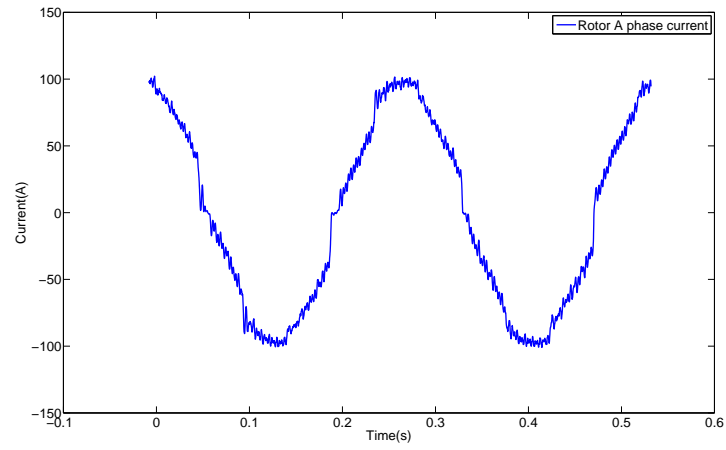


Figure 7.59: Rotor Current After the Compensation Super-synchronous Mode

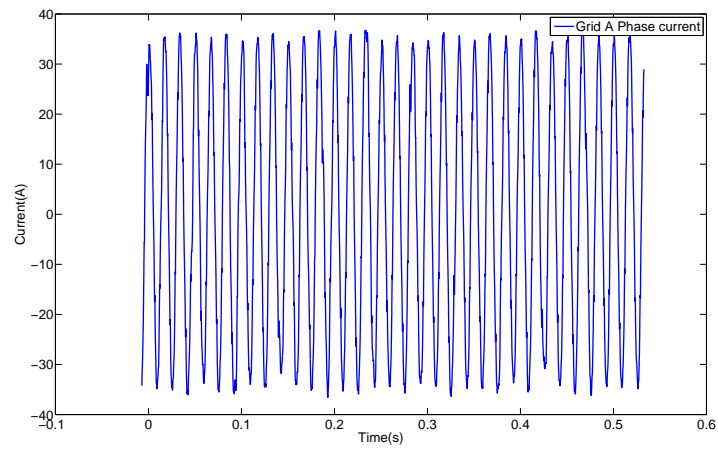


Figure 7.60: Grid Current After the Compensation Super-synchronous Mode

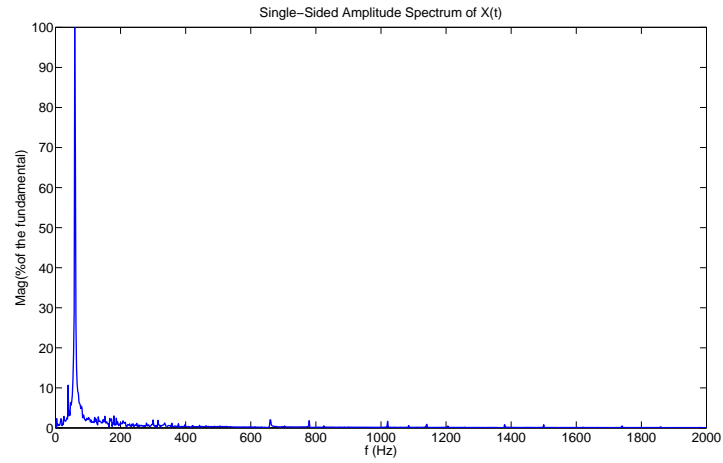


Figure 7.61: Grid Current FFT After the Compensation Super-Synchronous Mode

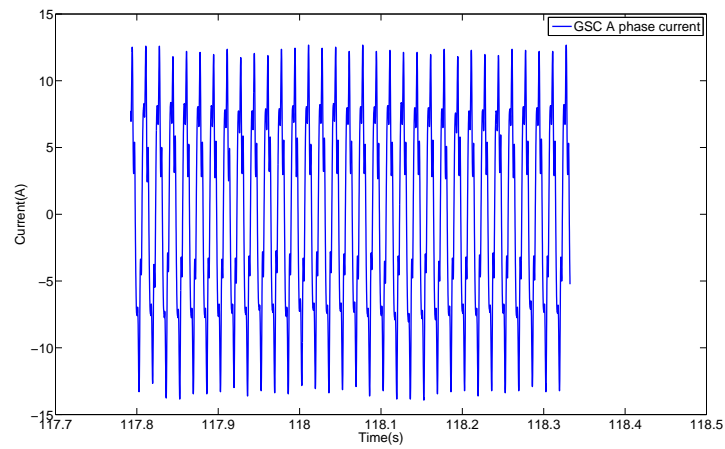


Figure 7.62: GSC Current After the Compensation Sub-Synchronous Mode

The multiple reference frame harmonics regulator takes use of both RSC and GSC to compensate the harmonics in stator and grid current. RSC is used to increase the quality of the stator current and GSC to compensate the current harmonics drawn from the nonlinear load. According to the IEEE harmonics standard [21], under the most crucial situation : $I_{SC}/I_L < 20$, I_{SC} being the maximum short circuit current and I_L referring to the maximum demand load current. The most significant harmonic component should smaller than 4% of the fundamental component. Running the fast Fourier transform (FFT) analyzes to the stator current at different speed mode, the results shows in table 7.1 From the table 7.1, the significant harmonics

Table 7.1: STATOR CURRENT HARMONICS VALUES OF DIFFERENT ORDER

Harmonics Order	Before Regulation sub	After Regulation sub
5	8.7%	3.1%
7	3.1%	3.2%
	Before Regulation syn	After Regulation syn
5	5.9%	2.8%
7	2%	1.4%
	Before Regulation super	After Regulation super
5	5.1%	3.2%
7	1.2%	1.1%

are the 5th and 7th for the stator. Following the IEEE harmonics standard [21], only the one that bigger than 4% is regulated.

The FFT analysis results for the current of the grid is shown in table7.2. The gird current last significant harmonics is the 11th. The harmonic regulation for the GSC still only applies to the harmonic component bigger than 4%.

Table 7.2: HARMONICS VALUES OF DIFFERENT ORDER

Harmonics Order	Before Regulation sub	After Regulation sub
5	12.2%	3.1%
7	2%	2.8%
11	3%	2.5%
	Before Regulation	After Regulation
5	11.6%	1.4%
7	1.9%	1.3%
11	3.3%	3.1%
	Before Regulation	After Regulation
5	10%	1.9%
7	1.7%	0.6%
11	2.6%	2%

7.3 Experimental Results Of Hybrid Observer Sensor-less Drive

7.3.1 Experimental Results Of The Squirrel Cage Machine Hybrid Observer Sensor-less Drive

The squirrel cage machine used to run the hybrid observer sensor-less drive have the machine parameter:

$$r_s = 11.05\Omega$$

$$r'_r = 6.11\Omega$$

$$L_{ss} = 0.3165H$$

$$L'_{rr} = L_s$$

$$L_M = 0.2939H$$

To demonstrate the hardware system response to the positive step, the machine is given a same 300RPM step change. As shown in Figure 7.63,7.64 and 9. The rotor speed will goes to the command 900RPM after 0.2s with a small overshoot. The current waveform indicate that when the step input exert on the system, the current will suddenly increase to accelerate the machine then enters a new steady-state value.

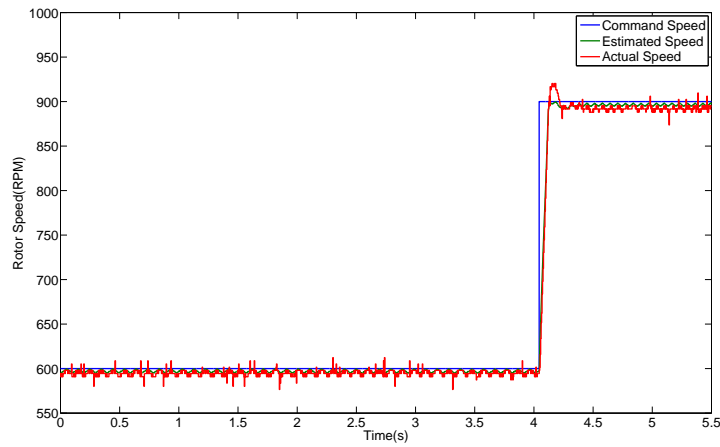


Figure 7.63: Measured speed response with a positive step

A -1500RPM step will the machine speed drop from 600RPM to -900RPM in less than 0.3s. A deceleration torque current will response to the desired speed decrease. The speed and a-phase current waveforms are shown in figure 7.65 7.66

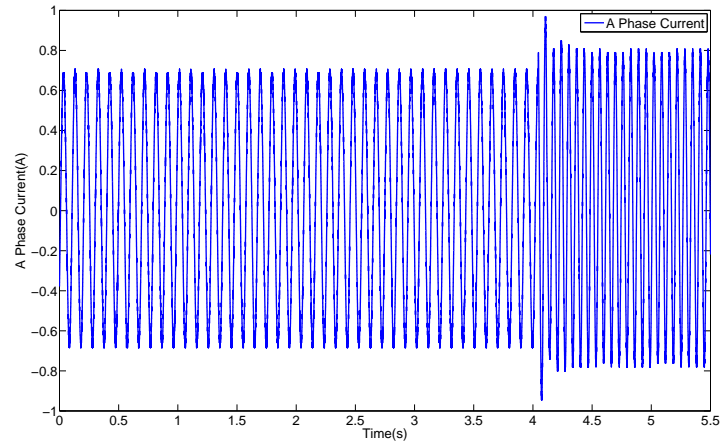


Figure 7.64: Measured current response with a positive step

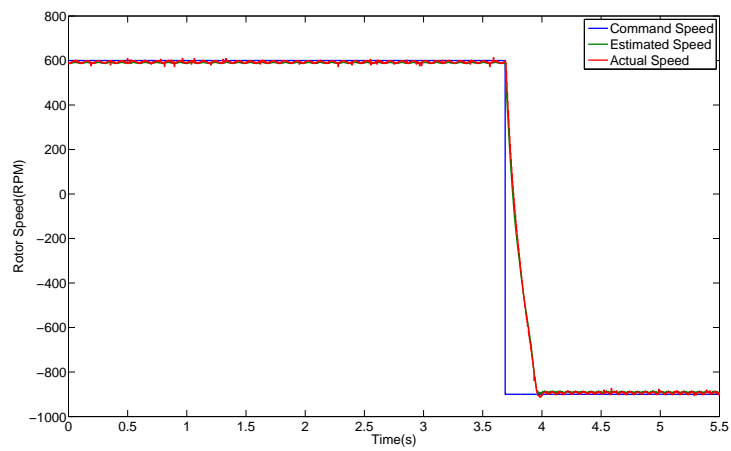


Figure 7.65: Measured speed response with a negative step

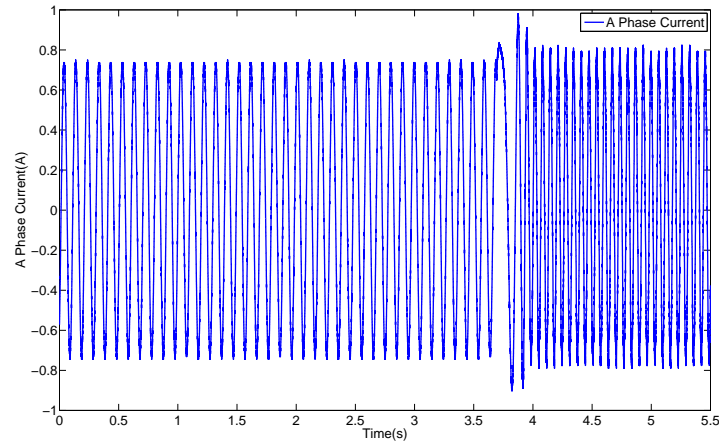


Figure 7.66: Measured current response with a negative step

Figure 7.67, carries out the speed wave when the command machine speed changes from 600RPM to stand still condition. The actual speed about 0.4 second to enter the zero speed, which is longer compares to second step input case. The a-phase current is elaborated in Figure 7.68. After the machine stops, the current will hold to the last step value of the deaccelerate process. In the hardware, the current will vibrate with a amplitude of 0.1A.

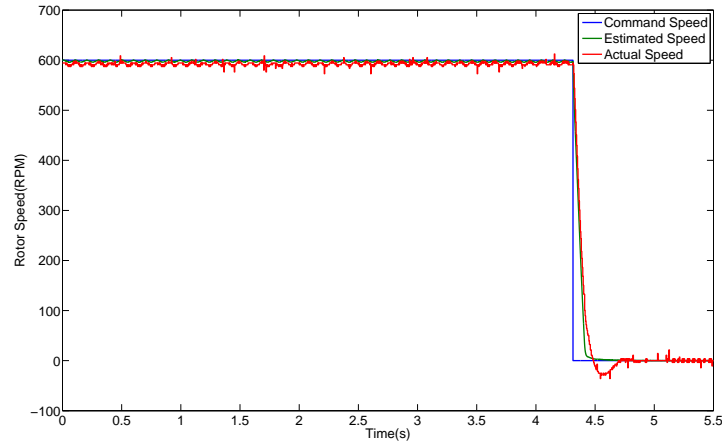


Figure 7.67: Measured speed response with a zero speed command

Compare the current waveform gathered form the simulations results and the hardware results. The current is bigger in the hardware. In simulation the on load condition is ideal, however, in hardware the ideal

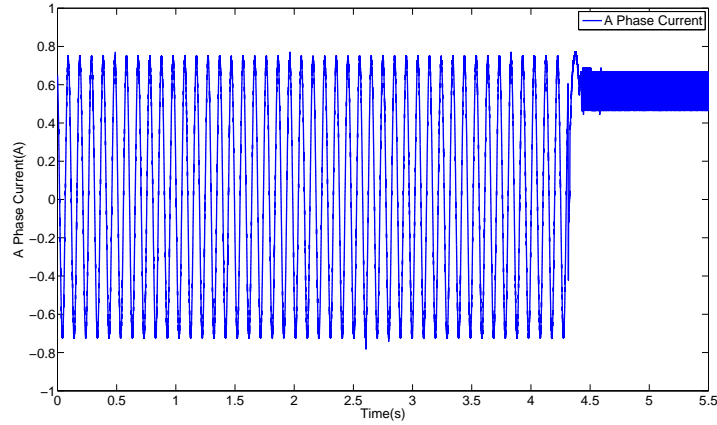


Figure 7.68: Measured current response with a zero speed command

there might be a slight load torque.

7.3.2 Experimental Results Of The Wound Rotor Machine Hybrid Observer Sensor-less Drive

The hybrid observer speed sensor-less drive for the DFIG wind generation system will be operated under sub-synchronous, synchronous and super-synchronous mode. When the machine is running at sub-synchronous mode, the estimated and actual speed of the machine is shown in Figure 7.69. It can be conclude that when the machine enters the steady state of the speed sensor-less drive, the estimated speed can trace the actual speed with a chattering less than $\pm 2\%$.

The hybrid observer for DFIG takes the stator and rotor current as the electrical states for the control. The Figure 7.70, 7.71 shows the estimated and measured stator and rotor current when the machine is running at sub-synchronous mode.

When machine is driven at synchronous speed the estimated and actual speed of the machine is shown in Figure 7.72, the chattering is around $\pm 2\%$. At synchronous mode, the stator measured and estimated current under stationary frame is shown in Figure 7.73. The rotor estimated and measured current referred to the stator the waveform is shown in Figure 7.74.

Running the speed sensor-less drive using the hybrid observer under super-synchronous mode. The estimated and actual speed of the machine is shown in Figure 7.75. The stator and rotor current waveform when the machine is running at super-synchronous mode is shown as in Figure 7.76 7.77.

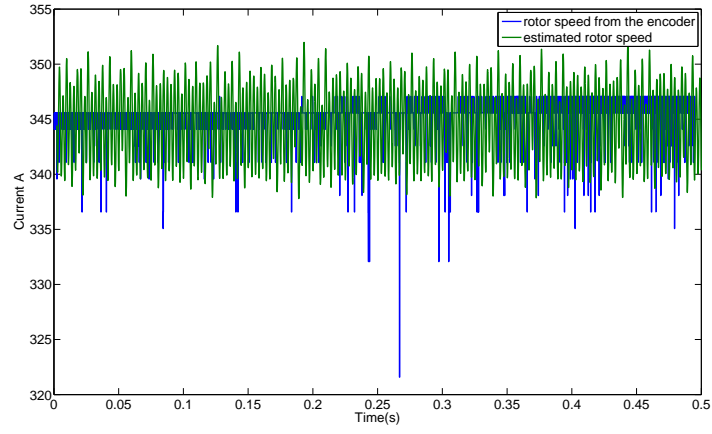


Figure 7.69: Hybrid observer speed performance sub-synchronous mode

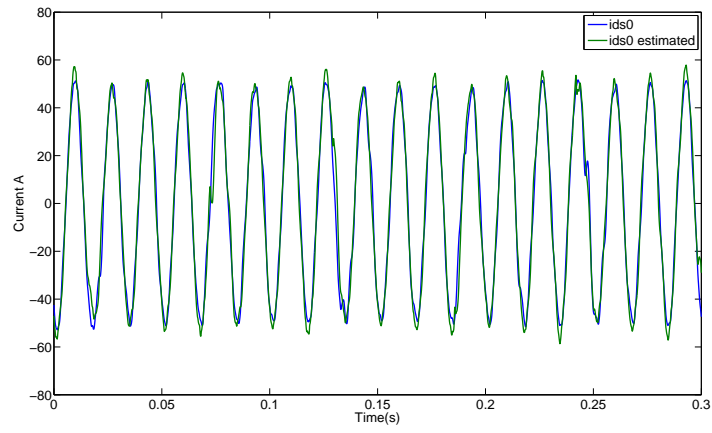


Figure 7.70: Stator current estimated and measured sub-synchronous mode

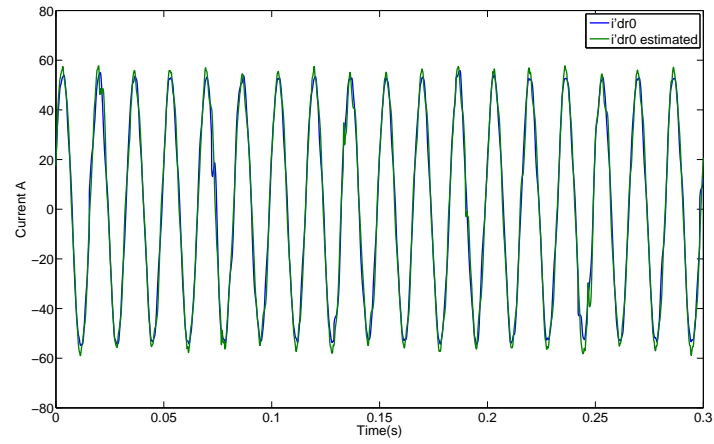


Figure 7.71: Rotor current estimated and measured sub-synchronous mode

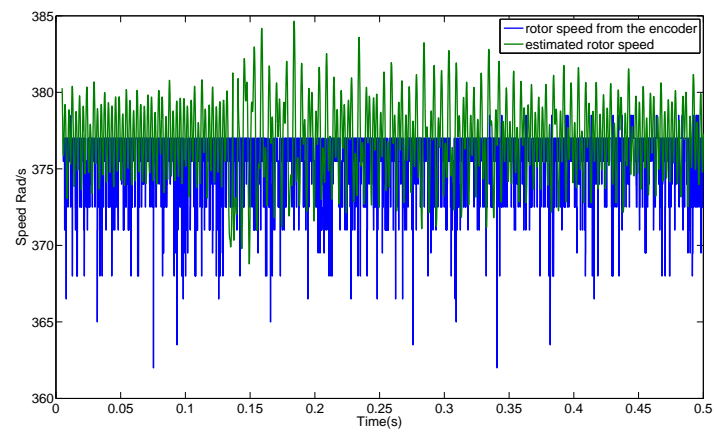


Figure 7.72: Hybrid observer speed performance synchronous mode

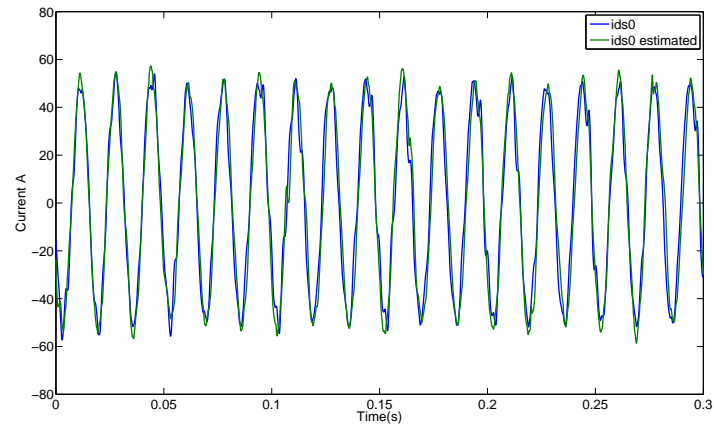


Figure 7.73: Stator current estimated and measured synchronous mode

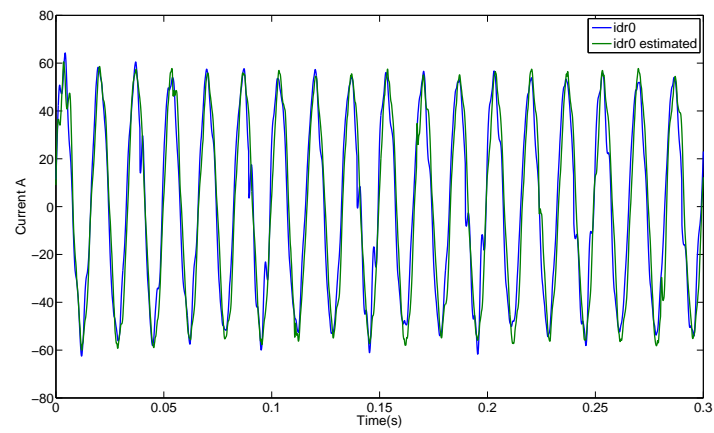


Figure 7.74: Rotor current estimated and measured synchronous mode

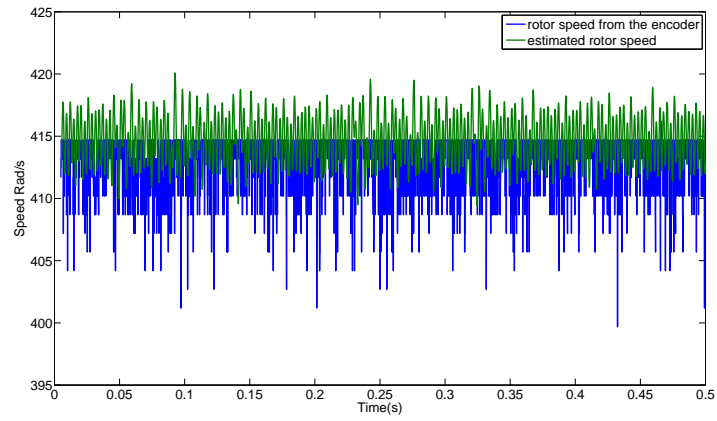


Figure 7.75: Hybrid observer speed performance super-synchronous mode

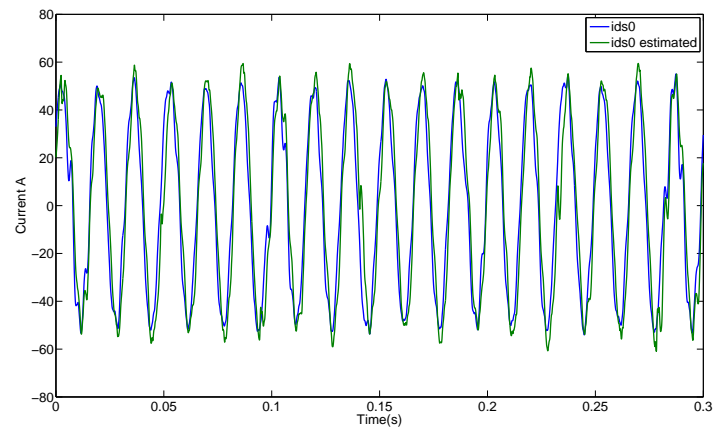


Figure 7.76: Stator current estimated and measured synchronous mode

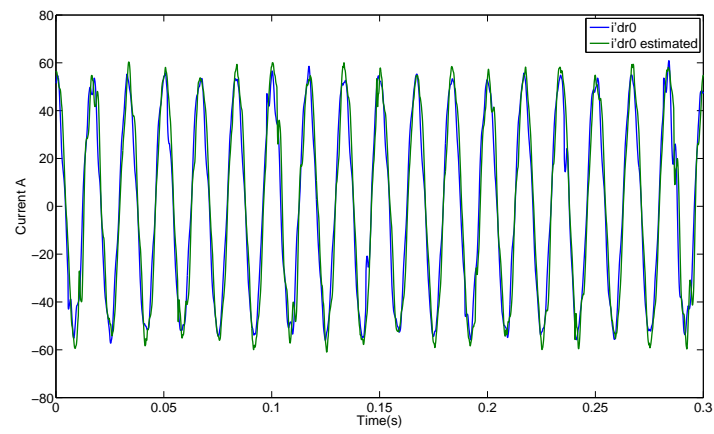


Figure 7.77: Rotor current estimated and measured synchronous mode

Applying the hybrid observer for DFIG to operate the speed sensor-less drive, under sub-synchronous, synchronous and super-synchronous mode, the stator and rotor currents from the observer have error compares to the measured current. From the current waveforms, there are bigger harmonics content in the current compares to the results in section 7.1. Authors believe the reason cause this problems are the machine parameter calibration is not perfect. Unlike the squirrel cage machine in section 7.3.1, which we have the full data from the TI. The DFIG parameters are getting from the machine test conducted in the lab. The hybrid observer designed for DFIG is a parameter depended observer, the error in the parameter will deteriorate the performance.

The speed is calculated by counting the pules number in a certain short period of time. This method depends on the impulses signal quality given by the encoder. The spikes of the actual speed waveforms might caused by some bad quality input. Authors believe this condition difference cause the different in the current waveforms. The actual speed plot is got form a 2500 pulse/rev quadrature speed encoder.

Chapter 8

Conclusion

In this dissertation, a DFIG based wind turbine systems are proposed and researched. The basic AC system with DFIG stator connecting to the grid and rotor connected via a back-to-back converter to the grid. The control algorithm is detailed and simulated using matlab/simulink. The hardware experimental conducted in the Clemson micro-grid and power electronics lab results are also carried out to validate the simulation results under three different operation condition: sub-synchronous mode, synchronous mode, and super-synchronous mode.

With the stator flux oriented control scheme proposed in this dissertation, the DFIG is connecting to a dc link and exchange power through a diode bridge and a rotor-side converter. Compare to a fully controllable power converter, the diode rectifier is much less expensive. The frequency in the stator which is controlled by a closed loop frequency regulator, can trace the reference frequency. A custom designed DFIG with a low rated operating speed could eliminate the gearbox using the proposed topology to connect the DFIG to the dc grid.

The harmonics introduced by the diode bridge will cause distortion in the stator current. However, these harmonics can be detected using a multiple reference frame estimator. The harmonics regulation method proposed in the paper handle each harmonics order at the corresponding frequency. Harmonics will be transferred to DC component, then compensated using the RSC. Multiple reference frame harmonic regulator in the paper wont require extra device to cancel the harmonics in stator current, and the PI control is stable and easy to achieve. The harmonics regulation control in the paper is parallel with the main DFIG decouple control, the harmonics regulation will not affect the FOC for the DFIG.

In the three phase AC DFIG system, connecting the non-linear load to the PCC, the harmonics

draw from the nonlinear load current will decrease the system power quality. In the simulation section, the harmonics regulation method is applied to the harmonics components up to 19th order for the sake of verifying the proposed method. In the hardware experimental section. Following the IEEE stander, the harmonics regulation only applied to the ones has amplitude bigger 4% of the fundamental component.

The last part of this dissertation investigated speed-sensorless state estimation for induction machines. The proposed observer exploits the bilinear structure of the induction machine dynamics, and includes a Luenberger observer for stator current and rotor flux estimation, and a sliding mode observer for speed estimation. The hybrid nature of the proposed observer allows us to exploit the simplicity of the Luenberger observer and robustness of the sliding mode observer. The proposed observer does not require information of the machine inertia. Lots of scenario the inertia of the machine changes during the drive process. The changing of the inertia might due to the changing of the working condition, some load inertia might change with the speed. For the squirrel cage machine, the simulation and the experimental results are presented when feeding a positive step input, negative step input and enters the zero speed condition. For the DFIG the simulation and the experimental results are elaborated for three different operation condition: sub-synchronous mode, synchronous mode, and super-synchronous mode.

The future work will be three folds. First, due to the hardware limits in the lab, there is no DC sink which we can put around 50kw back in to it. All the topologies and control algorithms presented in this dissertation regarding to the DC DFIG topology are not validated with experimental results. Second, the multiple reference frame harmonics estimator and regulator works well with certain harmonics orders. With sub-harmonics and some higher order harmonics other than $m=6n \pm 1$, the harmonics compensation will be fully achieved combining the the multiple reference frame harmonics estimator and regulator with active filter. Third, for the hybrid observer for the induction machine, the observer is parameter depended for the Luenberger observer part. With poor parameter information or some parameter variation during operating period, the results will be deteriorated. This problem can be solved adding a on-line parameter identification algorithm to the observer.

Bibliography

- [1] O. A. Ahmed and J. Bleijs. Power flow control methods for an ultracapacitor bidirectional converter in dc microgrids: a comparative study. *Renewable and Sustainable Energy Reviews*, 26:727–738, 2013.
- [2] C. Lee, N. R. Chaudhuri, B. Chaudhuri, and S. R. Hui. Droop control of distributed electric springs for stabilizing future power grid. *IEEE Transactions on Smart Grid*, 4(3):1558–1566, 2013.
- [3] H. Farhangi. The path of the smart grid. *IEEE power and energy magazine*, 8(1), 2010.
- [4] S. Chowdhury, S. P. Chowdhury, and P. Crossley. *Microgrids and active distribution networks*. Institution of Engineering and Technology, 2009.
- [5] P. P. Varaiya, F. F. Wu, and J. W. Bialek. Smart operation of smart grid: Risk-limiting dispatch. *Proceedings of the IEEE*, 99(1):40–57, 2011.
- [6] R. H. Lasseter and P. Paigi. Microgrid: A conceptual solution. In *Power Electronics Specialists Conference, 2004. PESC 04. 2004 IEEE 35th Annual*, volume 6, pages 4285–4290. IEEE, 2004.
- [7] N. Pogaku, M. Prodanovic, and T. C. Green. Modeling, analysis and testing of autonomous operation of an inverter-based microgrid. *IEEE Transactions on power electronics*, 22(2):613–625, 2007.
- [8] F. Katiraei, M. R. Iravani, and P. W. Lehn. Micro-grid autonomous operation during and subsequent to islanding process. *IEEE Transactions on power delivery*, 20(1):248–257, 2005.
- [9] Y. Li, D. M. Vilathgamuwa, and P. C. Loh. Design, analysis, and real-time testing of a controller for multibus microgrid system. *IEEE Transactions on power electronics*, 19(5):1195–1204, 2004.
- [10] I. Boldea. *Variable speed generators*. CRC press, 2005.

- [11] J. M. Carrasco, L. G. Franquelo, J. T Bialasiewicz, E. Galván, R. C. PortilloGuisado, M. A. M Prats, J. I. León, and N. Moreno-Alfonso. Power-electronic systems for the grid integration of renewable energy sources: A survey. *IEEE Transactions on industrial electronics*, 53(4):1002–1016, 2006.
- [12] S. Muller, M. Deicke, and R. W De Doncker. Doubly fed induction generator systems for wind turbines. *IEEE Industry applications magazine*, 8(3):26–33, 2002.
- [13] F. M. Hughes, O. Anaya-Lara, N. Jenkins, and G. Strbac. Control of dfig-based wind generation for power network support. *IEEE Transactions on Power Systems*, 20(4):1958–1966, 2005.
- [14] J. R. Rodríguez, J. W. Dixon, J. R. Espinoza, J. Pontt, and P. Lezana. Pwm regenerative rectifiers: state of the art. *Industrial Electronics, IEEE Transactions on*, 52(1):5–22, 2005.
- [15] Z. Wang, C. Xie, C. He, and G. Chen. A waveform control technique for high power shunt active power filter based on repetitive control algorithm. In *Applied Power Electronics Conference and Exposition (APEC), 2010 Twenty-Fifth Annual IEEE*, pages 361–366. IEEE, 2010.
- [16] H. Kakigano, Y. Miura, T. Ise, and R. Uchida. Dc micro-grid for super high quality distributionsystem configuration and control of distributed generations and energy storage devices. In *Power Electronics Specialists Conference, 2006. PESC'06. 37th IEEE*, pages 1–7. IEEE, 2006.
- [17] B. Liu, F. Zhuo, Y. Zhu, and H. Yi. System operation and energy management of a renewable energy-based dc micro-grid for high penetration depth application. *IEEE Transactions on Smart Grid*, 6(3):1147–1155, 2015.
- [18] Y. Ito, Z. Yang, and H. Akagi. Dc microgrid based distribution power generation system. In *Power Electronics and Motion Control Conference, 2004. IPEMC 2004. The 4th International*, volume 3, pages 1740–1745. IEEE, 2004.
- [19] L. Xu and D. Chen. Control and operation of a dc microgrid with variable generation and energy storage. *IEEE Transactions on Power Delivery*, 26(4):2513–2522, 2011.
- [20] M. T. Abolhassani, P. Niazi, H. A. Toliyat, and P. Enjeti. A sensorless integrated doubly-fed electric alternator/active filter (idea) for variable speed wind energy system. In *Industry Applications Conference, 2003. 38th IAS Annual Meeting. Conference Record of the*, volume 1, pages 507–514. IEEE, 2003.
- [21] I. F II. Ieee recommended practices and requirements for harmonic control in electrical power systems. 1993.

- [22] Electromagnetic Compatibility. Part 3: Limits-section 2: Limits for harmonic current emissions (equipment input current ≤ 16 a per phase). *IEC Standard*, pages 61000–3, 1995.
- [23] E. Tremblay, A. Chandra, and P. J. Lagace. Grid-side converter control of dfig wind turbines to enhance power quality of distribution network. In *Power Engineering Society General Meeting, 2006. IEEE*, pages 6–pp. IEEE, 2006.
- [24] F. Blaschke. A new method for the structural decoupling of ac induction machines. In *Conf. Rec. IFAC*, volume 1, 1971.
- [25] D. Casadei, F. Profumo, G. Serra, and A. Tani. Foc and dtc: Two viable schemes for induction motors torque control. *IEEE transactions on Power Electronics*, 17(5):779–787, 2002.
- [26] M. Talib, Z. Ibrahim, N. A. Rahim, and N. M. Yaakop. Development of combined vector and direct torque control methods for independent two induction motor drives. In *Power Engineering and Optimization Conference (PEDCO) Melaka, Malaysia, 2012 Ieee International*, pages 78–83. IEEE, 2012.
- [27] S. Ogasawara, H. Akagi, and A. Nabae. A novel pwm scheme of voltage source inverters based on space vector theory. *Archiv für Elektrotechnik*, 74(1):33–41, 1990.
- [28] L. Zhang, C. Wathanasarn, and F. Hardan. An efficient microprocessor-based pulse-width modulator using space vector modulation strategy. In *Industrial Electronics, Control and Instrumentation, 1994. IECON'94., 20th International Conference on*, volume 1, pages 91–96. IEEE, 1994.
- [29] H. Kubota and K. Matsuse. Speed sensorless field-oriented control of induction motor with rotor resistance adaptation. *Industry Applications, IEEE Transactions on*, 30(5):1219–1224, 1994.
- [30] H. Kubota, K. Matsuse, and T. Nakano. Dsp-based speed adaptive flux observer of induction motor. *IEEE Transactions on Industry Applications*, 29(2):344–348, 1993.
- [31] J. Maes and J. Melkebeek. Speed-sensorless direct torque control of induction motors using an adaptive flux observer. *Industry Applications, IEEE Transactions on*, 36(3):778–785, 2000.
- [32] J. Soltani, G. R. A. Markadeh, N. R. Abjadi, and H. W. Ping. A new adaptive direct torque control (dte) scheme based-on svm for adjustable speed sensorless induction motor drive. In *Electrical Machines and Systems, 2007. ICEMS. International Conference on*, pages 497–502. IEEE, 2007.

- [33] B. Shen, B. Mwinyiwiwa, Y. Zhang, and B. Ooi. Sensorless maximum power point tracking of wind by dfig using rotor position phase lock loop (pll). *IEEE Transactions on Power Electronics*, 24(4):942–951, 2009.
- [34] B. Shen and B. T. Ooi. Novel sensorless decoupled pq control of doubly-fed induction generator (dfig) based on phase locking to gamma-delta frame. In *Power Electronics Specialists Conference, 2005. PESC'05. IEEE 36th*, pages 2670–2675. IEEE, 2005.
- [35] B. Shen, V. Low, and B. T. Ooi. Slip frequency phase lock loop (pll) for decoupled pq control of doubly-fed induction generator (dfig). In *Industrial Electronics Society, 2004. IECON 2004. 30th Annual Conference of IEEE*, volume 1, pages 80–85. IEEE, 2004.
- [36] Y. Kim, S. Sul, and M. Park. Speed sensorless vector control of induction motor using extended kalman filter. *IEEE Transactions on Industry Applications*, 30(5):1225–1233, 1994.
- [37] K. L. Shi, T. F. Chan, Y. K. Wong, and S. L. Ho. Speed estimation of an induction motor drive using an optimized extended kalman filter. *Industrial Electronics, IEEE Transactions on*, 49(1):124–133, 2002.
- [38] F. J. Lin. Robust speed-controlled induction-motor drive using ekf and rls estimators. *IEEE Proceedings-Electric Power Applications*, 143(3):186–192, 1996.
- [39] G. Welch and G. Bishop. An introduction to the kalman filter. 2006. *University of North Carolina: Chapel Hill, North Carolina, US*, 2006.
- [40] F. Gustafsson and G. Hendeby. Some relations between extended and unscented kalman filters. *IEEE Transactions on Signal Processing*, 60(2):545–555, 2012.
- [41] G. A. Einicke and L. B. White. Robust extended kalman filtering. *IEEE Transactions on Signal Processing*, 47(9):2596–2599, 1999.
- [42] R. W. Bass, V. D. Norum, and L. Schwartz. Optimal multichannel nonlinear filtering. *Journal of Mathematical Analysis and Applications*, 16(1):152–164, 1966.
- [43] C. Lascu, I. Boldea, and F. Blaabjerg. A class of speed-sensorless sliding-mode observers for high-performance induction motor drives. *Industrial Electronics, IEEE Transactions on*, 56(9):3394–3403, 2009.

- [44] F. Chen and M. W. Dunnigan. Comparative study of a sliding-mode observer and kalman filters for full state estimation in an induction machine. *IEE Proceedings-Electric Power Applications*, 149(1):53–64, 2002.
- [45] M. Tursini, R. Petrella, and F. Parasiliti. Adaptive sliding-mode observer for speed-sensorless control of induction motors. *Industry Applications, IEEE Transactions on*, 36(5):1380–1387, 2000.
- [46] G. Cimini, M. L. Corradini, G. Ippoliti, N. Malerba, and G. Orlando. Control of variable speed wind energy conversion systems by a discrete-time sliding mode approach. In *Mechatronics (ICM), 2013 IEEE International Conference on*, pages 736–741. IEEE, 2013.
- [47] Y. Shtessel, C. Edwards, L. Fridman, and A. Levant. *Sliding mode control and observation*. Springer, 2014.
- [48] A. Levant. Sliding order and sliding accuracy in sliding mode control. *International journal of control*, 58(6):1247–1263, 1993.
- [49] V. Utkin and J. Guldner, J. and Shi. *Sliding mode control in electro-mechanical systems*, volume 34. CRC press, 2009.
- [50] C. Edwards and S. Spurgeon. *Sliding mode control: theory and applications*. Crc Press, 1998.
- [51] P. C. Krause, O. Wasynczuk, S. D. Sudhoff, and S. Pekarek. *Analysis of electric machinery and drive systems*, volume 75. Wiley. com, 2013.
- [52] S. Chattopadhyay, M. Mitra, and S. Sengupta. Electric power quality. In *Electric Power Quality*, pages 5–12. Springer, 2011.
- [53] A. P. Ferrero, A. .and Morando, R. Ottoboni, and G. Superti-Furga. On the meaning of the park power components in three-phase systems under non-sinusoidal conditions. *European Transactions on Electrical Power*, 3(1):33–43, 1993.
- [54] H. Akagi and A. Nabae. The p-q theory in three-phase systems under non-sinusoidal conditions. *International Transactions on Electrical Energy Systems*, 3(1):27–31, 1993.
- [55] S. J. Chapman. *Electric machinery fundamentals*. Tata McGraw-Hill Education, 2005.

- [56] W. Qiao, G. K. Venayagamoorthy, and R. G. Harley. Real-time implementation of a statcom on a wind farm equipped with doubly fed induction generators. *Industry Applications, IEEE Transactions on*, 45(1):98–107, 2009.
- [57] R. Pena, J. C. Clare, and G. M. Asher. Doubly fed induction generator using back-to-back pwm converters and its application to variable-speed wind-energy generation. *IEEE Proceedings-Electric Power Applications*, 143(3):231–241, 1996.
- [58] J. Li and K. A. Corzine. Harmonic compensation for variable speed dfig wind turbines using multiple reference frame theory. In *2015 IEEE Applied Power Electronics Conference and Exposition (APEC)*, pages 2974–2979. IEEE, 2015.
- [59] J. Liang, D. F. Howard, J. A. Restrepo, and R. G. Harley. Feedforward transient compensation control for dfig wind turbines during both balanced and unbalanced grid disturbances. *IEEE Transactions on Industry Applications*, 49(3):1452–1463, 2013.
- [60] F. Liu, Y. Zhou, S. Duan, J. Yin, B. Liu, and F. Liu. Parameter design of a two-current-loop controller used in a grid-connected inverter system with lcl filter. *Industrial Electronics, IEEE Transactions on*, 56(11):4483–4491, 2009.
- [61] M. Liserre, F. Blaabjerg, and S. Hansen. Design and control of an lcl-filter-based three-phase active rectifier. *IEEE Transactions on industry applications*, 41(5):1281–1291, 2005.
- [62] G. Shen, D. Xu, L. Cao, and X. Zhu. An improved control strategy for grid-connected voltage source inverters with an lcl filter. *IEEE Transactions on Power Electronics*, 23(4):1899–1906, 2008.
- [63] J. Li and K. A. Corzine. Development of grid-connected inverters for micro-grid. In *Power Systems Conference (PSC), 2014 Clemson University*, pages 1–6. IEEE, 2014.
- [64] W. Wu, Y. He, T. Tang, and F. Blaabjerg. A new design method for the passive damped lcl and llcl filter-based single-phase grid-tied inverter. *IEEE Transactions on Industrial Electronics*, 60(10):4339–4350, 2013.
- [65] W. Wu, Y. He, and F. Blaabjerg. An llcl power filter for single-phase grid-tied inverter. *IEEE Transactions on Power Electronics*, 27(2):782–789, 2012.

- [66] J. Ekanayake and N. Jenkins. Comparison of the response of doubly fed and fixed-speed induction generator wind turbines to changes in network frequency. *IEEE Transactions on Energy conversion*, 19(4):800–802, 2004.
- [67] J. B. Ekanayake, L. Holdsworth, X. Wu, and N. Jenkins. Dynamic modeling of doubly fed induction generator wind turbines. *IEEE transactions on power systems*, 18(2):803–809, 2003.
- [68] G. D. Marques and M. F. Iacchetti. Inner control method and frequency regulation of a dfig connected to a dc link. *Energy Conversion, IEEE Transactions on*, 29(2):435–444, 2014.
- [69] G. D. Marques and M. F. Iacchetti. Control method of the dfig connected to a dc link through a diode bridge. *Energy and Power Engineering*, 5(04):102, 2013.
- [70] G. D. Marques and M. F. Iacchetti. Stator frequency regulation in a field-oriented controlled dfig connected to a dc link. *Industrial Electronics, IEEE Transactions on*, 61(11):5930–5939, 2014.
- [71] R. Krishnan. *Electric motor drives: modeling, analysis, and control*. Prentice Hall, 2001.
- [72] H. Sasaki and T. Machida. A new method to eliminate ac harmonic currents by magnetic flux compensation-considerations on basic design. *IEEE Transactions on Power Apparatus and Systems*, 5(PAS-90):2009–2019, 1971.
- [73] F. Peng. Application issues of active power filters. *IEEE Industry Applications Magazine*, 4(5):21–30, 1998.
- [74] S. Bhattacharya, D. M. Frank, T. M. and Divan, and B. Banerjee. Parallel active filter system implementation and design issues for utility interface of adjustable speed drive systems. 2:1032–1039, 1996.
- [75] A. M. Al-Zamil and D. A. Torrey. A passive series, active shunt filter for high power applications. *IEEE Transactions on Power Electronics*, 16(1):101–109, 2001.
- [76] H. Fujita and H. Akagi. The unified power quality conditioner: the integration of series-and shunt-active filters. *IEEE transactions on power electronics*, 13(2):315–322, 1998.
- [77] P. L. Chapman and S. D. Sudhoff. A multiple reference frame synchronous estimator/regulator. *Energy Conversion, IEEE Transactions on*, 15(2):197–202, 2000.
- [78] P. L. Chapman, S. D. Sudhoff, and C. A. Whitcomb. Multiple reference frame analysis of non-sinusoidal brushless dc drives. *Energy Conversion, IEEE Transactions on*, 14(3):440–446, 1999.

- [79] S. D. Sudhoff. Multiple reference frame analysis of an unsymmetrical induction machine. *IEEE transactions on energy conversion*, 8(3):425–432, 1993.
- [80] P. C. Krause and J. R. Hake. Method of multiple reference frames applied to the analysis of a rectifier-inverter induction motor drive. *IEEE Transactions on Power Apparatus and Systems*, (11):1635–1641, 1969.
- [81] P. C. Krause. Method of multiple reference frames applied to the analysis of symmetrical induction machinery. *Power Apparatus and Systems, IEEE Transactions on*, (1):218–227, 1968.
- [82] M. T. Abolhassani, P. Enjeti, and H. A. Toliyat. Integrated doubly-fed electric alternator/active filter (idea), a viable power quality solution, for wind energy conversion systems. In *Industry Applications Conference, 2004. 39th IAS Annual Meeting. Conference Record of the 2004 IEEE*, volume 3, pages 2036–2043. IEEE, 2004.
- [83] P. Xiao, K. A. Corzine, and G. K. Venayagamoorthy. Multiple reference frame-based control of three-phase pwm boost rectifiers under unbalanced and distorted input conditions. *Power Electronics, IEEE Transactions on*, 23(4):2006–2017, 2008.
- [84] A. El Assoudi, E. H. El Yaagoubi, and H. Hammouri. Non-linear observer based on the euler discretization. *International Journal of Control*, 75(11):784–791, 2002.
- [85] D. Luenberger. An introduction to observers. *IEEE Transactions on automatic control*, 16(6):596–602, 1971.
- [86] A. Alessandri and P. Coletta. Design of luenberger observers for a class of hybrid linear systems. In *International Workshop on Hybrid Systems: Computation and Control*, pages 7–18. Springer, 2001.
- [87] P. K. Nandam and P. C. Sen. A comparative study of a luenberger observer and adaptive observer-based variable structure speed control system using a self-controlled synchronous motor. *IEEE transactions on industrial electronics*, 37(2):127–132, 1990.
- [88] T. Kwon, M. Shin, and D. Hyun. Speed sensorless stator flux-oriented control of induction motor in the field weakening region using luenberger observer. *IEEE Transactions on Power Electronics*, 20(4):864–869, 2005.
- [89] K. Ogata and Y. Yang. *Modern control engineering*. Prentice-Hall Englewood Cliffs, 1970.

- [90] E. D. Sontag. *Mathematical control theory: deterministic finite dimensional systems*, volume 6. Springer Science & Business Media, 2013.
- [91] J. S. Thongam and M. Ouhrouche. *MPPT control methods in wind energy conversion systems*. INTECH Open Access Publisher, 2011.
- [92] E. Koutroulis and K. Kalaitzakis. Design of a maximum power tracking system for wind-energy-conversion applications. *IEEE transactions on industrial electronics*, 53(2):486–494, 2006.
- [93] G. Walker. Evaluating mppt converter topologies using a matlab pv model. *Journal of Electrical & Electronics Engineering, Australia*, 21(1):49, 2001.
- [94] B. W. McCormick. *Aerodynamics, aeronautics, and flight mechanics*, volume 2. Wiley New York, 1995.
- [95] J. J. Bertin and M. L. Smith. *Aerodynamics for engineers*. Prentice-Hall, 1998.
- [96] S. H. Jangamshetti and V. G. Rau. Normalized power curves as a tool for identification of optimum wind turbine generator parameters. *IEEE Transactions on Energy Conversion*, 16(3):283–288, 2001.
- [97] R. E. Wilson and P. Lissaman. *Applied aerodynamics of wind power machines*. [Corvallis, Or., Oregon State University], 1974.
- [98] R. W. Erickson and D. Maksimovic. *Fundamentals of power electronics*. Springer Science & Business Media, 2007.